

VIBRONIC COHERENCE IN KETOCAROTENOIDS AND SEMICONDUCTOR QUANTUM DOTS

By

Nila Mohan Thazhe Mecheri

A DISSERTATION

Submitted to
Michigan State University
in partial fulfillment of the requirements
for the degree of

Chemistry – Doctor of Philosophy

2023

ABSTRACT

Electronic-vibrational coupling drives the relaxation of optically prepared excitations in both carotenoids and semiconductor quantum dots (QDs). As a result of this electronic-vibrational (vibronic) coupling, coherent wavepacket motions are observed during the excitation relaxation processes. The first part of the dissertation describes the relaxation of the optically prepared bright S_2 state to dark S_1 state via bridging intermediate, S_x . The spectroscopic signature and the vibrational coherences of the intermediate state S_x involved in the nonradiative decay were characterized using broadband multidimensional spectroscopic techniques. Analysis of vibrational coherences shows that S_x undergoes displacements along out-of-plane coordinates as it passes to the S_1 state. The second part of the dissertation discusses the nonradiative relaxation in oleate-capped QDs. This process involves excited-state coherent wavepacket motions through a cascade of conical intersections between exciton potential-energy surfaces. Excited state wavepacket motions are observed at frequencies matching the vibrational modes of the organic ligands. These observations indicate that the ligand vibrations are quantum coherently mixed with the core electronic states of the QDs. The third part of the dissertation presents the role vibronic coupling in photoinduced charge transfer from the QD core to a surface ligand electron acceptor molecule, methyl viologen dication (MV^{2+}). The observation of coherent wavepacket motions is consistent with presence of a charge transfer intermediate with a mixed QD-MV character, and this intermediate initiate photoinduced charge transfer from the core of the QD to the surface acceptor molecule. These results raise new opportunities for the engineering light-harvesting properties of materials through the control of electronic-vibrational coupling and quantum coherences.

Copyright by
NILA MOHAN THAZHE MECHERI
2023

To my parents and Louis

ACKNOWLEDGEMENTS

I would like to thank my advisor, Professor Warren F. Beck, for the opportunity to learn and grow under his guidance. You guided and supported my journey, ensuring my success as a researcher. I have enjoyed every opportunity to discuss new possibilities and new science with you. Our engaging conversations have been a source of motivation, consistently igniting my enthusiasm to experiment with novel ideas after each meeting. You have also granted me intellectual freedom to pursue new and innovative ideas, allowing me to follow my interests and passion for research. Thank you. I would like to thank our collaborators, Professor P. Gregory Van Patten at Middle Tennessee State University for providing us the quantum dot samples and Professor Benjamin Levine at Stony Brook University for the contributions on the theory calculations.

I would like to thank Ryan Tilluck for training, mentoring, and helping me solve problems in the laser lab as well as guiding me in getting started with the quantum dot project. I thank Jessica Gurchiek for mentoring me during the initial days of my PhD. I would like to thank my cohorts, Sourav, and Justin for helping me with the experiments, for their friendship and support throughout my time in the Beck lab. Chase, thank you for helping me with the data analysis and all the best for your future endeavors. Thank you Kunwei for being a very supportive friend and all the best for your future. Despite our limited time together in the lab, Shanu, thank you for being understanding and supporting friend. I am excited to see the progress and success of your research projects in the future. I am thankful to my committee members, Professors Benjamin Levine, Marcos Dantus, and Thomas Hamann for asking insightful questions and providing me support during my PhD.

I also thank Kevin Cavey at MTSU for accommodating our requests and sending us quantum dot samples to carry out the femtosecond experiments.

I have made some great friends at my time at the MSU. We've cherished many fun moments, camping adventures, and good food with each other that reminded me of home. Thank you, Arnab, Atanu, Saro, Manoj, Akhil, Anand and Amal. I received a great deal of support from my IISER friends throughout this journey. I thank Vinaya, Elizabeth, Aparna, Neha, Abhin, Ajmal, Sreya and Mirsana for their friendship. Thank you, Manasa, for all love, care, and support over the past several years.

I am incredibly grateful to for my loving and supportive family. Thank you, Amma and Pappa, for everything you have provided me till today. Without your love and support, I would never be able to achieve my goals. Thank you for always believing in me. I am thankful to my brother for his care and support throughout my life. Most importantly, I thank my partner, Louis for his tremendous patience, support, love, and care during the ups and downs of this journey.

The work featured in this dissertation was supported by the U.S. Department of Energy, Office of Basic Energy Sciences, Solar Photochemistry Program under Award Number DE-SC0021197, Photosynthetic Systems Program under Award Number DE- SC0010847 and National Science Foundation, Chemistry of Life Processes under Award number 1904655. I'd like to thank the financial support through Alfred J. and Ruth Zeits Endowed Fellowship from the College of Natural Science and the Rogowski Chemistry Graduate Fellowship from the Department of Chemistry at Michigan State University.

TABLE OF CONTENTS

LIST OF TABLES	ix
LIST OF FIGURES	x
LIST OF ABBREVIATIONS.....	xix
Overview of the Dissertation.....	1
Chapter 1: Introduction to Carotenoids and Semiconductor Quantum Dots.....	4
1.1 Nonradiative Relaxation Mechanisms	4
1.2 Orange Carotenoid Protein: An Overview.....	5
1.3 Photophysics of Carotenoids.....	6
1.3.1 Nonradiative Decay in Carotenoids.....	8
1.4 Semiconductor Quantum Dots	11
1.4.1 Electronic Structure and Surface of Colloidal CdSe QDs	13
1.4.2 Hot Carrier Cooling in QDs	15
1.5 Multidimensional Electronic Spectroscopy	18
1.5.1 Excitation Pulse Sequence in 2DES	19
1.5.2 Third-Order Nonlinear Optical Responses.....	20
1.5.3 Quantum Coherences in 2DES	25
1.6 Instrumentation.....	30
1.7 Data Processing and Analysis	35
REFERENCES	37
Chapter 2: Broadband 2DES Detection of Vibrational Coherence in the S _x State of Ketocarotenoid Canthaxanthin.....	51
2.1 Introduction	52
2.2 Experimental Methods.....	54
2.2.1 Samples.....	54
2.2.2 Linear Spectroscopy.....	55
2.2.3 Two-Dimensional Electronic Spectroscopy.....	55
2.3 Results.....	57
2.3.1 Linear Spectroscopy.....	57
2.3.2 2DES Spectra	59
2.3.3 Global and Target Modeling of the 2DES spectra.....	61
2.3.4 Vibrational Coherence.....	66
2.3.5 Anisotropy.....	73
2.4 Discussion.....	77
REFERENCES	83
APPENDIX	88
Chapter 3: Electronic-Vibrational Coherences in Oleate-capped CdSe Quantum Dots.....	96
3.1 Introduction	97

3.2 Experimental Methods.....	99
3.2.1 CdSe Quantum Dot Synthesis and Characterization	99
3.2.2 Linear Spectroscopy and Photoluminescence	102
3.2.3 Two-Dimensional Electronic Spectroscopy	102
3.3 Results.....	104
3.3.1 Particle Size and Surface Characterization	104
3.3.2 Linear Spectroscopy.....	105
3.3.3 2DES Spectra	107
3.3.4 Global Modeling and Coherence Analysis.....	109
3.4 Discussion.....	120
REFERENCES	124
APPENDIX	128
Chapter 4: Vibronic Coherences Initiate Photoinduced Charge Transfer from CdSe Quantum Dots to Methyl Viologen	130
4.1 Introduction	131
4.2 Experimental Methods.....	135
4.2.1 CdSe Quantum Dot Synthesis and Characterization	135
4.2.2 Linear Spectroscopy and Photoluminescence	136
4.2.3 Two-Dimensional Electronic Spectroscopy	137
4.3 Results.....	138
4.3.1 Linear Absorption and Photoluminescence	138
4.3.2 Two-Dimensional Electronic Spectroscopy.....	140
4.3.3 Global Analysis and Coherence Analysis.....	142
4.4 Discussion.....	151
REFERENCES	155
APPENDIX	159

LIST OF TABLES

Table 3.1. Parameters (frequency, amplitude, phase, and damping time) for LPSVD analysis of X3 excitation at the indicated coordinates in 2D spectra. These coordinates are indicated in the 2D spectra (Figure 3.6).....	115
Table 3.2. Parameters for LPSVD analysis for X2 excitation at the indicated coordinates in 2D spectra. These coordinates are indicated in the excitation specific coherence map (Figure 3.11).....	119
Table 4.1. Parameters (frequency, amplitude, phase, and damping time) for LPSVD analysis of X3 excitation for QDs at the indicated coordinates in 2D spectra.....	148
Table 4.2. Parameters (frequency, amplitude, phase, and damping time) for LPSVD analysis of X3 excitation for QD-MV ²⁺ at the indicated coordinates in 2D spectra.....	148

LIST OF FIGURES

- Figure 1.1.** Structure of different carotenoids..... 7
- Figure 1.2.** Schematic representations for the potential energy surfaces for the singlet states of a carotenoid, plotted here as a function of a reaction coordinate composed of sequential displacements from the Franck–Condon geometry of the optically prepared S_2 state with respect to the C–C and C=C stretching and out-of-plane (φ) coordinates of the isoprenoid backbone. Planar and distorted conformations are divided by a low barrier at the structure marked ‡ on the reaction coordinate axis. The mixed S_2 , S_1 , and S_0 surfaces are proposed to converge near the geometry of the S_2 minimum owing to a conical intersection (CI) of the diabatic surfaces. Arrows indicate vertical optical transitions from planar and distorted conformations to the S_2 state. Adapted from Gurchiek et al.²⁹ 10
- Figure 1.3.** Illustration of the quantum confinement compared to the bulk semiconductor. When the spatial extent of wavefunction is smaller than the Bohr exciton radius (a_b), size-dependent optical properties are observed. Adapted from ref 47.⁴⁷ 12
- Figure 1.4.** Illustration of different surface capping ligands and their possible coupling of vibrational modes with QD core electronic states.⁸² (a) Ligands, alkylamine (I), trioctylphosphineoxide (TOPO)(II), and alkylcarboxyl group (III), where R represents the alkyl chain, interacting with the surface of CdSe QDs. (b) Possible coupling of energy levels of ligand (solid line and dashed line representing bonding orbital and antibonding orbital, respectively) to core electronic states and (c) exciton manifold for excitons (electron hole pair) X1 to X4, as labelled. (Reproduced from Ryan Tilluck’s dissertation.⁸³) 14
- Figure 1.5.** Broadband pulse sequences in the 2DES experiment. The red Gaussian pulse envelopes depict the excitation pulses in the pulse sequence. The blue signals represent the coherences emitted from the sample after the interaction of the pulses. The first pulse creates coherence that evolves over time, followed by the interaction of the second pulse to create a population. The third pulse interacts with the system to create another coherence and an evolving electric field (blue) is emitted from the sample. (Reproduced from Ryan Tilluck’s dissertation,⁸³ adapted from work by the Jonas group.^{121,133}) 20
- Figure 1.6.** WMEL diagram (top) and Feynman diagram (bottom) of ground-state bleaching signal. The figures on the right correspond to the non-rephasing pathway, whereas those on the left correspond to the rephasing pathway. In the WMEL diagram, time evolves towards the right, and the field matter interactions are numbered as 1, 2, and 3 with marked time delays. The solid arrows represent the field-matter interaction on the *ket* side of the Feynman diagram, whereas the dashed arrows represent the interaction on the *bra* side. The dotted line in the WMEL and dashed arrow in the Feynman diagram represent the emitted signal after a series of field-matter interactions. The vertical line in the Feynman diagram represents the evolution of the time. 22

Figure 1.7. WMEL diagram (top) and Feynman diagram (bottom) of stimulated emission signals. The figures on the right correspond to the non-rephasing pathway, whereas those on the left correspond to the rephasing pathway.....	24
Figure 1.8. WMEL diagram (top) and Feynman diagram (bottom) of the excited-state absorption signal. The figures on the right correspond to the non-rephasing pathway, whereas those on the left correspond to the rephasing pathway.....	25
Figure 1.9. Example WMEL diagram for electronic coherences between excited electronic states, 1 and 2. The figures on the right correspond to the non-rephasing pathway, whereas those on the left correspond to the rephasing pathway.....	27
Figure 1.10. Example of WMEL diagram for vibrational coherences between ground and excited electronic state, 1. Vibrational states are indicated by v_0 and v_1 . The figures on the right correspond to the non-rephasing pathway, whereas those on the left correspond to the rephasing pathway.....	28
Figure 1.11. Example WMEL diagram for ground-state vibrational coherences (stimulated Raman) between ground and excited electronic state. Vibrational states are indicated by v_0 and v_1 . The figures on the right correspond to the non-rephasing pathway, whereas those on the left correspond to the rephasing pathway.....	29
Figure 1.12. An example broadband laser spectrum in the range of 510-710 nm used in 2DES experiments. The full width at half maximum (FWHM) is 120 nm and the transform limited pulse duration was 6.8 fs.....	31
Figure 1.13. Interferometric autocorrelation of the pump pulses, determined as the integral of the SHG-FROG spectrogram ¹⁵⁶ (left panel). SHG-FROG ¹⁵⁸ spectrogram for the pump pulses, as measured with scanned pulse pairs prepared by the pump beam's pulse shaper in the 2DES spectrometer.....	33
Figure 1.14. Instrumentation set up used in the 2DES experiment. The Yb laser (4W, 100 kHz, 1040 nm) is pumped to a NOPA to generate broadband visible pulses ranging from 500-700 nm. The adaptive pulse shapers and the pairs of chirp mirrors compress the pulse to the transform limit. The pulse shaper on the pump beam is manipulated to create a pulse pair and vary the time between the pump pulses. A time-of-flight delay stage is used to vary the time delay between the pump and the probe beams. The emitted signals are collected using a home-built spectrograph and a fast CCD.....	34
Figure 1.15. Evolution of the amplitude obtained after FFT of the pump-induced change in probe-transmission with respect to the time, integrated along the detection axis for CdSe QDs with 7 fs pulses. The coherent oscillations are isolated, mirrored and zero-padded prior to the FFT process.....	36
Figure 2.1. Structure of canthaxanthin.....	53

Figure 2.2. Linear absorption spectrum of CAN in toluene solvent (blue dotted curve), plotted with respect to the wavenumber ν as the relative oscillator strength, $\epsilon(\nu)/\nu$. The 14000–17000- cm^{-1} range of the spectrum is also plotted with a $\times 25$ scaling of the ordinate. The laser intensity spectrum from the broadband excitation pulses used in the 2DES experiments (red solid curve) is superimposed. 58

Figure 2.3. Evolution of total amplitude (K) 2DES spectra from CAN in toluene at six waiting times T 60

Figure 2.4. 2D global and target model for the main band excitation region of the 2DES K spectra from CAN in toluene. (a) Kinetic scheme and time constants for nonradiative decay of the S_2 state via an intermediate, S_x , to the S_1 state. (b) Time dependence of the populations for the S_2 (blue), S_x (green dotted), and S_1 (red dashed) spectrokinetic species. (c) 2D evolution-associated difference spectra (EADS) for the three spectrokinetic species. The EADS are scaled relative to the maximum of the ESA signal in the S_1 compartment. 63

Figure 2.5. 2D global and target model for the red tail excitation region of the 2DES K spectra from CAN in toluene. (a) Kinetic scheme and time constants for nonradiative decay of the S_2 state via an intermediate, S_x , to the S_1 state. (b) Time dependence of the populations for the S_2 (blue), S_x (green dotted), and S_1 (red dashed) spectrokinetic species. (c) 2D evolution-associated difference spectra (EADS) for the three spectrokinetic species. The EADS are scaled relative to the maximum of the ESA signal in the S_1 compartment in the main band region (Figure 2.4). 65

Figure 2.6. Oscillation maps for the principal vibrational coherences detected in the 2DES K spectra from CAN in toluene. 69

Figure 2.7. Total amplitude K and anisotropy r transients with excitation at 18200 cm^{-1} and detection at 16750 cm^{-1} in the S_x cross peak in the main band excitation region. (a) K transient, with the fit from the global model (from Figure 2.4) superimposed. (b) Residual (K -global model) transient. (c) Fourier transform amplitude spectrum of the K residual over the $T = 70$ - 500 fs range. (d) Anisotropy r transient, with a fitted exponential (40 fs time constant). (e) Residual (r -exponential fit) transient. (f) Fourier transform amplitude spectrum of the r residual over the $T = 100$ -500 fs range. Error bars show the 95% confidence intervals for the K and r amplitudes. 71

Figure 2.8. Total amplitude K and anisotropy r transients with excitation at 17200 cm^{-1} and detection at 16750 cm^{-1} in the S_x cross peak in the red tail excitation region. (a) K transient, with the fit from the global model (Figure 2.5) superimposed. (b) Residual (K -global model) transient. (c) Fourier transform amplitude spectrum of the K residual over the $T = 70$ -500 fs range. (d) Anisotropy r transient, with a fitted exponential (92 fs time constant). (e) Residual (r -exponential fit) transient. (f) Fourier transform amplitude spectrum of the r residual over the $T = 100$ -500 fs range. Error bars show the 95% confidence intervals for the K and r amplitudes. 72

Figure 2.9. Schematic representations for the potential energy surfaces for the singlet states of a carotenoid, plotted here as a function of a reaction coordinate composed of sequential displacements from the Franck–Condon geometry of the optically prepared S_2 state with respect to the C–C and C=C stretching and out-of-plane (ϕ) coordinates of the isoprenoid backbone. Planar and distorted conformations are divided by a low barrier at the structure marked ‡ on the reaction coordinate axis. The dashed curve indicates that the S_2 surface will be stabilized by displacements with respect to the out-of-plane coordinates when the isoprenoid backbone is carbonyl substituted, as in CAN. The mixed S_2 , S_1 , and S_0 surfaces are proposed to converge near the geometry of the S_2 minimum owing to a conical intersection (CI) of the diabatic surfaces. Arrows indicate vertical optical transitions from planar and distorted conformations to the S_2 state. Adapted from Ref. 6..... 80

Figure A2.1. Laser intensity and residual phase spectrum for the laser pulses in the pump beam of the 2DES spectrometer, with the latter determined at the sample’s position by MIIPS scans²³ after compression..... 88

Figure A2.2. Laser intensity and residual phase spectrum for the laser pulses in the probe beam of the 2DES spectrometer, with the latter determined at the sample’s position by MIIPS scans after compression..... 89

Figure A2.3. Interferometric autocorrelation and SHG-FROG²⁴ spectrograms for the pump pulses, as measured with scanned pulse pairs prepared by the pump beam’s pulse shaper..... 89

Figure A2.4. 1D global and target model for the 2DES spectra from CAN in toluene, with excitation at 18500 cm^{-1} (540 nm). (a) Kinetic scheme for nonradiative decay of the resonant S_2 state via the intermediate S_x to the S_1 state. (b) Time dependence of the populations for the S_2 , S_x , and S_1 spectrokinetic species. (c) Evolution-associated difference spectra (EADS) for the three spectrokinetic species. 90

Figure A2.5. Oscillation map for vibrational coherence at 100 cm^{-1} detected in the 2DES K spectra from CAN in toluene..... 91

Figure A2.6. Oscillation map for vibrational coherence at 1800 cm^{-1} detected in the 2DES K spectra from CAN in toluene..... 91

Figure A2.7. Total amplitude K transient and modulation spectrum on the diagonal in the main band excitation region. (a) K transient with excitation at 18200 cm^{-1} and detection at 18200 cm^{-1} , with the fit from the global model (red curve) superimposed. (b) Residual (K –global model) transient. (c) Fourier transform amplitude spectrum of the residual over the $T = 75\text{--}500\text{ fs}$ range. In (b,c) the bars show the 95% confidence intervals for the K amplitudes..... 92

Figure A2.8. Total amplitude K transient and modulation spectrum in the S_1 cross peak in the main band excitation region. (a) K transient with excitation at 18200 cm^{-1} and detection at 15500 cm^{-1} , with the fit from the global model (red curve) superimposed. (b)

Residual (K - global model) transient. (c) Fourier transform amplitude spectrum of the residual over the $T = 75$ -500 fs range. In (b,c) the bars show the 95% confidence intervals for the K amplitudes. 93

Figure A2.9. Total amplitude K transient and modulation spectrum on the diagonal in the red tail excitation region. (a) K transient with excitation at 17200 cm^{-1} and detection at 17200 cm^{-1} , with the fit from the global model (red curve) superimposed. (b) Residual (K - global model) transient. (c) Fourier transform amplitude spectrum of the residual over the $T = 75$ -500 fs range. In (b,c) the bars show the 95% confidence intervals for the K amplitudes. 94

Figure A2.10. Total amplitude K transient and modulation spectrum in the S_1 cross peak in the red tail excitation region. (a) K transient with excitation at 17200 cm^{-1} and detection at 15500 cm^{-1} , with the fit from the global model (red curve) superimposed. (b) Residual (K - global model) transient. (c) Fourier transform amplitude spectrum of the residual over the $T = 75$ -500 fs range. In (b,c) the bars show the 95% confidence intervals for the K amplitudes. 95

Figure 3.1. Schematic representation of the potential energy surface representing the relaxation of optical excitation via a cascade of conical intersections via coherent wavepacket motions. Adapted from Tilluck et al.¹⁴..... 99

Figure 3.2. Schematics of DART-MS analysis. The sample was heated using a thermal desorption module where the ion source ionized the desorbed molecules. The mass spectrometer detects ionized ligand molecules and shows the signatures of the released species in the mass spectrum. Inset plot shows the linear temperature ramp applied over certain time. 101

Figure 3.3. Characterization of oleate CdSe (a) Transmission electron microscopy images of oleate-capped CdSe quantum dots with 500,000x magnification and 5x zoom. (b) Size distribution of CdSe QDs, 245 total particles counted, 62 particles 6.98 nm. The mean of the size distribution is 6.97 nm with a standard deviation of 0.50 nm. Mass spectra collected from TD-DART-MS of oleate-capped CdSe QDs. The ligands are desorbed from the inorganic core at $430\text{ }^\circ\text{C}$. In addition to the major peak at $m/z = 281.4$ corresponding to the oleate anion, two peaks associated with subsequent additions of oxygen are observed at $m/z = 297.4$ and $m/z = 313.3$. Desorption plot obtained from DART-MS for $m/z = 281.4$ 105

Figure 3.4. Energy level diagram of CdSe QDs. On the left, the electron-hole energy levels are marked with hole levels in the valence band ($1S_{3/2}$, $1P_{3/2}$, $2S_{3/2}$, $3S_{1/2}$) and electron levels ($1S_e$ and $1P_e$) in the conduction band. The band edge exciton ($1S_{3/2} 1S_e$) is denoted as X1, the second exciton ($2S_{3/2} 1S_e$) is denoted as X2, the third exciton ($1P_{3/2} 1P_e$) as X3, and the fourth exciton ($3S_{1/2} 1S_e$) as X4. The figure on the right shows the exciton energy levels of the first four excitons with energy in eV on the left and wavelength on the right. 106

Figure 3.5. Steady-state spectroscopic characterization of oleate-capped QDs. Linear absorption spectrum (blue trace) marked with various exciton energy levels, and

photoluminescence spectrum (orange trace) with overlapping laser spectrum (gray filled).....107

Figure 3.6. Time evolution of 2DES spectra of oleate capped CdSe quantum dots with respect to the population time, T . The spectra are presented with evenly spaced contours and are tinted with colors indicating positive (red, GSB/SE) and negative (blue, ESA/PA) signals. The side panels plot the 2DES signal amplitude sliced along the diagonal at $T = 0$ fs (blue) superimposed on the linear absorption oscillator strength (black dotted) and photoluminescence (PL) spectra (orange). Amplitude transients sampled at the marked coordinates (excitation at X3 and detection at X3, X1, and PL) are shown in Figure 3.7.....109

Figure 3.7. Global analysis of the population response of the X3 (2.066-2.194 eV) excitation region of 2DES spectrum of oleate capped CdSe quantum dots. (a) Kinetic scheme for the global model with time constants, 12 + 1 fs, 40 + 1 fs, 212 + 3 fs, 1.41 + 0.47 ps, and 186 + 40 ps for each relaxation pathway. (b) Evolution of population with respect to time for each compartment. (c) Evolution associated difference spectra (EADS) for each compartment in the kinetic scheme. (d) Transients at various coordinates, (X3, X3) (blue trace), (X3, X1) (green trace) and (X3, PL) (maroon trace). The lower panels show the residual for each coordinate overlapped with the fit obtained from the LPSVD analysis...112

Figure 3.8. Coherence analysis accompanying the relaxation of X3. (a) Excitation-specific coherence map at X3 excitation (from 10-200 fs). The side panel includes the steady state absorption spectrum (b) LPSVD spectra for coordinates (X3, X3), (X3, X1) and (X3, PL) for time range 10- 500 fs.....114

Figure 3.9. 3DES spectra/mode specific oscillation of modulations for rapidly damped modulations of frequencies, (a) 280 cm^{-1} , (b) 380 cm^{-1} , (c) 640 cm^{-1} , and (d) 720 cm^{-1}116

Figure 3.10. Global analysis of the population response of the X2 (1.952-2.016 eV) excitation region of 2DES spectrum of oleate capped CdSe quantum dots. (a) Kinetic scheme for the global model with time constants, 17 + 1 fs, 165 + 3 fs, 2.10 + 0.4 ps, and 164 + 40 ps for each relaxation pathway. (b) Evolution of population with respect to time for each compartment. (c) Evolution associated difference spectra (EADS) for each compartment in the kinetic scheme. (d) Transients at various coordinates, (X3, X3) (blue trace), (X3, X1) (green trace) and (X3, PL) (maroon trace). Lower panels show the residual for each coordinate overlapped with the fit obtained from the LPSVD analysis.....117

Figure 3.11. Coherence analysis accompanying the relaxation of X2. (a) Excitation specific coherence map at X3 excitation (from 10-200 fs). Side panel includes the steady state absorption spectrum (b) LPSVD spectra for coordinates (X2, X2), (X2, X1) and (X2, PL) for time range 10- 500 fs.....118

Figure 3.12. Vector representation of the 420 cm^{-1} , 650 cm^{-1} and 950 cm^{-1} obtained from the Raman spectra calculation of Cd oleate complex. Purple arrows indicate the direction of displacement of each atom from its equilibrium position.....121

Figure A3.1. Residual phase and intensity spectra of the femtosecond laser pulses used in the broadband multidimensional electronic spectroscopy experiments. Top panel shows residual phase spectra after compression of the laser pulses used in the 2DES experiment for the pump beam (solid), and for the probe beam (dashed), as determined by MIIPS scans.²⁰ Bottom panel is the intensity spectrum of the laser pulses.....128

Figure A3.2. SHG-FROG²¹ spectrogram for the pump pulses, as measured with scanned pulse pairs prepared by the pump beam's pulse shaper in the 2DES spectrometer.....129

Figure A3.3. Interferometric autocorrelation of the pump pulses, determined as the integral of the SHG-FROG spectrogram (Figure A3.2).....129

Figure 4.1. Energy level diagram for the photoinduced electron transfer from CdSe QD core to methyl viologen dication (MV^{2+}) inspired by Morris-Cohen et al.¹⁵ On the left, the electron ($1S_e$ and $1P_e$) and hole energy levels of the QDs are marked with solid lines. The conduction band (CB) and valence band (VB) of the QDs are marked with shaded regions. Exciton formation upon optical pulse interaction is indicated by the red arrow. On the right side, the lowest unoccupied molecular orbital (LUMO) and highest occupied molecular orbital (HOMO) levels of MV^{2+} are shown. Upon photoexcitation, an electron-hole pair is formed in the QDs. This electron is transferred from the $1S_e$ state of the QD to the LUMO of the MV^{2+} . The dotted arrow represents the electron recombination from the $MV^{••}$ to the hole in the VB.134

Figure 4.2. Spectroscopic characterization of methyl viologen. (a) Structure of 1,1'-dimethyl-4,4'-bipyridinium dication. (b) Absorption spectra at 298 K and of methyl viologen dication (blue trace) and radical cation in ethanol (red trace, redrawn from Watanabe et al.²³).....135

Figure 4.3. Energy level diagram of CdSe QDs and steady-state spectroscopic characterization of QD- MV^{2+} . (a) On the top left, the electron-hole energy levels are marked with hole levels in the valence band and electron levels in the conduction band. The vertical lines depict different excitons: X1 (red), X2 (green), and X3 (blue). The figure on the right shows the exciton energy levels with energy in eV on the left and wavelength on the right. (b) Linear absorption spectrum (blue trace) marked exciton energy levels, and photoluminescence (PL) spectrum (orange trace) with overlapping laser spectrum (gray filled). The brown trace is the photoinduced absorption spectrum of $MV^{••}$ radical cation adapted from Zhao et al.¹⁹ The purple trace is the PL of the QD- MV^{2+} complex.....139

Figure 4.4. Time evolution of 2D spectra of oleate-capped QD and QD- MV^{2+} with respect to the population time, T . The 2D spectra on the left are those of the oleate-capped QDs used in the control experiment. The 2D spectra of the QD- MV^{2+} complex are shown on the right side. The intensities of the 2D spectra are auto scaled with respect to the maxima of the signal at a given time, T . The side panels plot the linear absorption oscillator strength (blue), photoinduced absorption spectrum of $MV^{••}$ (brown), and photoluminescence (PL) spectra (orange). The amplitude transients sampled at the marked coordinates (excitation at X3 and detection at X3, X1, and PL) are shown in Figure 4.5.....141

Figure 4.5. Global analysis of the population response of the X3 (2.102-2.214 eV) excitation region of 2DES spectrum of QD-MV²⁺ complex. On the left is the kinetic scheme for the global model with time constants for each relaxation pathway. Evolution associated difference spectra (EADS) for each compartment in the kinetic scheme are present on the right. The final component of the model is enhanced 15 times to project out the amplitudes.....143

Figure 4.6. Amplitude transient comparison of QDs and QD-MV²⁺ at various coordinates. (a) 2D spectra of the QD-MV²⁺ complex with marked coordinates (X3, X3) (blue), (X3, X1) (green) and (X3, PL) (maroon). The side panels plot the linear absorption oscillator strength (blue), photoinduced absorption spectrum of MV^{•+} (brown), and photoluminescence (PL) spectra (orange). (b) Amplitude transients at for the QDs (top panel) and QD-MV²⁺ (bottom panel) for the marked coordinates in the 2D spectra.....146

Figure 4.7. Frequency analysis of the residuals of the transients shown in Figure 4.6. (a) Residuals of the transients presented in the Figure 4.6. The green traces correspond to the coordinate (X3, X1) and the maroon trace correspond to the coordinate (X3, PL). The LPSVD fit function is plotted as the black trace overlapping on the residuals of the transients. (b) LPSVD models for the oscillations observed in the residuals. The dotted lines represent the amplitude spectra of the QDs, and the solid lines represent the amplitude spectra of the QD-MV²⁺ of the complex. The model parameters are provided in Tables 4.1 and 4.2.....147

Figure 4.8. Comparison of excitation-specific coherence map at X3 excitation (from 10-200 fs) for QD and QD-MV²⁺ complex. The side panels plot the linear absorption oscillator strength (blue), photoinduced absorption spectrum of MV^{•+} (brown), and PL spectra (orange). The blue box illustrates the portion of the excitation-specific coherence map where significant amplitude differences between QD and QD-MV²⁺ are evident.....150

Figure 4.9. Vector representation of the vibrational modes obtained from the Raman spectra calculation of MV²⁺ for 340-450 cm⁻¹ region. Purple arrows indicate the direction of displacement of each atom from its equilibrium position during the vibrations.151

Figure 4.10. Schematic representation of the potential energy surface representing the relaxation of X3 optical excitation via a cascade of conical intersections via coherent wavepacket motions. The red potential energy curve depicts the bridging coherent charge transfer intermediate in the QD-MV²⁺ complex.153

Figure A4.1. Residual phase and intensity spectra of the femtosecond laser pulses used in the broadband multidimensional electronic spectroscopy experiments. Top panel shows residual phase spectra after compression of the laser pulses used in the 2DES experiment for the pump beam (solid), and for the probe beam (dashed), as determined by MIIPS scans.²⁷ Bottom panel is the intensity spectrum of the laser pulses.....159

Figure A4.2. SHG-FROG²⁸ spectrogram for the pump pulses, as measured with scanned pulse pairs prepared by the pump beam's pulse shaper in the 2DES spectrometer.....160

Figure A4.3. Interferometric autocorrelation of the pump pulses, determined as the integral of the SHG-FROG spectrogram (Figure A4.2).....160

LIST OF ABBREVIATIONS

2DES	Two-Dimensional Electronic Spectroscopy
CAN	Canthaxanthin
CB	Conduction Band
CCD	Charge-Coupled Device
CI	Conical Intersection
CT	Charge Transfer
CTD	C-Terminal Domain
DART	Direct Analysis in Real Time
EADS	Evolution Associated Difference Spectra
ESA	Excited State Absorption
FFT	Fast Fourier Transform
FROG	Frequency Resolved Optical Gating
FT	Fourier Transform
FWHM	Full Width at Half Maximum
GSB	Ground State Bleaching
HOMO	Highest Occupied Molecular Orbital
HOOP	Hydrogen-Out-of-Plane
HPLC	High Performance Liquid Chromatography
ICT	Intramolecular Charge Transfer
IR	Infrared
LED	Light Emitting Diode

LH	Light Harvesting
LO	Longitudinal Optical
LPSVD	Linear Prediction Singular Value Decomposition
LUMO	Lowest Unoccupied Molecular Orbital
MBE	Molecular Beam Epitaxy
MG	Milligram
MIIPS	Multiphoton Intrapulse Interference Scan
MOCVD	Metalorganic Chemical Vapor Deposition
MS	Mass Spectrometry
MTSU	Middle Tennessee State University
NIR	Near Infrared
NOPA	Noncollinear Optical Parametric Amplifier
NTD	N-Terminal Domain
OCP	Orange Carotenoid Protein
OCP ^O	Orange Carotenoid Protein-Orange state
OCP ^R	Orange Carotenoid Protein-Red state
ODE	Octadecene
PL	Photoluminescence
PTC	Phenyldithiocarbamate
QD	Quantum Dots
SE	Stimulated Emission
SHG	Second Harmonic Generation

SLM	Spatial Light Modulator
TA	Transient Absorption
TD	Thermal Desorption
TDM	Transition Dipole Moment
TEM	Transmission Electron Microscopy
THG	Third Harmonic Generation
TOPO	Trioctylphosphineoxide
UV	Ultraviolet
VB	Valence Band
WMEL	Wave-Mixing Energy Level Diagram

Overview of the Dissertation

The purpose of the work presented in this dissertation is to address the role of electronic-vibrational (vibronic) quantum coherences in nonradiative relaxation mechanism of carotenoids and semiconductor quantum dots (QDs) as well as the photoinduced charge transfer from QD core to an acceptor molecule. We employed multidimensional spectroscopic techniques on samples of ketocarotenoid molecule, canthaxanthin and CdSe QDs to understand the dynamics of nonradiative relaxation and photoinduced electron transfer. The correlation nature of multidimensional spectroscopic techniques enables us to determine the relaxation of excitation energy via a series of excited energy levels. The vibronic coherences manifest as amplitude modulations in the 2D spectra, and their frequencies provide the structural information on the vibrational motions involved in these processes. Using the time-evolution of the 2D spectra along with the vibronic coherence characterization, we address the following questions:

1. What are the electronic and vibrational dynamics accompanying the formation of intermediate, S_x in the nonradiative decay of S_2 in the ketocarotenoid canthaxanthin?
2. How do the vibrations of surface ligands and the QD core facilitate hot-carrier cooling of electrons and holes in oleate-capped QDs?
3. Do vibronic excitons involving the core and ligand vibrational modes initiate photoinduced charge transfer from the QD core to the acceptor molecule?

The dissertation is organized as follows:

Chapter 1 provides a brief introduction to carotenoids and semiconductor quantum dots. This chapter discusses nonradiative relaxation in carotenoids and reviews relevant

literature. The second section provides an introduction to semiconductor quantum dots and their previously suggested nonradiative relaxation mechanisms. In the final section of this chapter, a brief introduction to third-order nonlinear signals is provided along with experimental implementation of two-dimensional electronic spectroscopy (2DES).

Chapter 2 reports the results from the study of the nonradiative relaxation mechanism in ketocarotenoid canthaxanthin using multidimensional spectroscopy. We report the spectroscopic signature and vibrational coherence of the intermediate, S_x , that is involved in the nonradiative decay of bright S_2 state to the dark S_1 state. The results indicate that the S_x evolves along out-of-plane coordinates of the isoprenoid backbone as it relaxes to S_1 state.

Chapter 3 presents the results from the multidimensional spectroscopy that determine the coherent vibronic exciton mechanism of hot carrier cooling in oleate-capped CdSe QDs. This process involves excited-state coherent wavepacket motions through a cascade of conical intersections between exciton potential-energy surfaces. The results indicate that the ligand vibrations are quantum coherently mixed with the core electronic states of the QDs. Using coherence analyses we isolate the vibrational motions that aid the electron and hole relaxation in these QDs.

In the Chapter 4, we present the results from the multidimensional spectroscopy that determines the role of vibronic excitons on the photoinduced charge transfer from CdSe QD core to a surface electron acceptor methyl viologen (MV). We observe coherent wavepacket motions with frequencies of lattice-vibrations and the out-of-plane deformations of MV^{2+} . These observations are consistent with a charge transfer intermediate with a mixed QD-MV

character, and this intermediate initiates the photoinduced charge transfer from the core of the QD to the surface acceptor molecule.

Chapter 1: Introduction to Carotenoids and Semiconductor Quantum Dots

Nonradiative relaxation of excited states has been observed in both naturally existing photosynthetic light-harvesting structures and energy materials such as semiconductor quantum dots. The mechanism of nonradiative relaxation observed in these systems involves relaxation of the optically prepared excited states via the coupling of electronic and nuclear motions.¹⁻³ This chapter covers the background of the nonradiative relaxation observed in carotenoids, along with a review of the literature to date. The second part of the chapter provides a background on semiconductor quantum dots and the previously proposed mechanisms of nonradiative relaxation (hot-carrier cooling). We employed multidimensional electronic spectroscopic techniques to address the nonradiative relaxation mechanisms of these systems. The experimental implementation of this spectroscopic technique is discussed in the final section of this chapter.

1.1 Nonradiative Relaxation Mechanisms

Photosynthetic light harvesting systems and solar energy materials consist of a manifold of excited states including several vibrational energy levels. Upon an electric field interaction from an optical pulse, a wavepacket is created in the excited state which consists of both electronic and vibrational energy levels. This electronic-vibrational (vibronic) wavepacket evolves through the excited state potential energy surfaces and lose its excitation energy into vibrations in the form of nonradiative relaxation. The nonradiative relaxation is considered as a nonadiabatic mechanism which occurs beyond the Born-Oppenheimer regime.⁴⁻⁶ In the Born-Oppenheimer regime, the motions of electrons and nuclei evolve independently of each other owing to their large differences in

mass. However, in nonadiabatic mechanisms, the electrons couple to the nuclear motions of the molecules that allow for energy relaxation. Nonadiabatic processes occurs in the regions where the optically prepared wavepacket crosses the potential energy surfaces at the intersections called conical intersections (CI).^{4,7}

Several powerful experimental techniques employing ultrafast lasers have been applied to create and investigate excited states, enabling experimental investigations of the relaxation of excited states through these nonadiabatic processes. Some of the experimental techniques include transient absorption spectroscopy, multidimensional spectroscopy, and single molecule spectroscopy. These mechanisms have been used to explain several photophysical processes including coherent vibronic dynamics in energy transfer mechanisms⁸⁻¹¹ and photochemical reactions.¹²⁻¹⁴

1.2 Orange Carotenoid Protein: An Overview

Carotenoid molecules are an integral component of light-harvesting systems in plants and photosynthetic organisms.^{15,16} In cyanobacteria, ketocarotenoids serve as chromophores for ambient light sensing in the orange carotenoid protein (OCP).^{15,17-23} The OCP facilitates the nonphotochemical quenching of bilin chromophores in the core of light-harvesting protein complexes, phycobilisomes.²³ The OCP consists of two protein domains, C-terminal domain (CTD) and N-terminal domain (NTD). The ketocarotenoid is located at the interface between the NTD and CTD. Upon excitation of the ketocarotenoid in the OCP using mid-visible photons, it gets photoactivated from the resting orange state (OCP⁰) to the active red state (OCP^R). The absorption spectra of the OCP^R exhibits a redshift of 50 nm compared to that of the OCP⁰.^{23,24} In terms of protein structure, the process of photoactivation involves translocation of the carotenoid molecule into the NTD and

displacement of the CTD.^{23,25} The NTD of OCP^R then binds to the core of the phycobilisome to facilitate nonphotochemical quenching. The photoactivation process of OCP from OCP⁰ to OCP^R involves significant changes in the conformation and position of the carotenoid molecule.^{23,26} However, the impact of photoactivation on the electronic structure of the ketocarotenoid is still under investigation. As an initial stage, it's crucial to understand the impact of photoexcitation on carotenoid molecules before delving into their response to photoactivation in OCP. The next section gives an overview of the structure and photophysical processes in carotenoids.

1.3 Photophysics of Carotenoids

Carotenoid molecules consist of a long-conjugated isoprenoid backbone with various functional groups at their ends. Examples include canthaxanthin, β -carotene, peridinin, and zeaxanthin (Figure 1.1). Owing to the planar structure of these molecules, they fall under the C_{2h} symmetry group. Therefore, the ground state S_0 has $1A_g^-$ symmetry, while the first excited state, S_1 , and second excited state, S_2 , have symmetries $2A_g^-$ and $1B_u^+$, respectively.²⁷ The absorption spectrum of a typical carotenoid consists of a strong band in the mid-visible region. The first excited state, S_1 , is considered a dark state owing to the lack of dipole-allowed transitions from the ground state, S_0 . Consequently, the strong absorption band in the mid-visible region of the absorption spectrum is attributed to the transition from the S_0 to the second excited state, S_2 .^{28,29} These transitions are $\pi \rightarrow \pi^*$ excitations of the long-conjugated isoprenoid backbone.^{27,30,31} The energies of these transitions are similar to the particle-in-a box problem, where an increase in the conjugation length results in a decrease in the energy gap.³² Additionally, most carotenoid molecules also exhibit vibronic

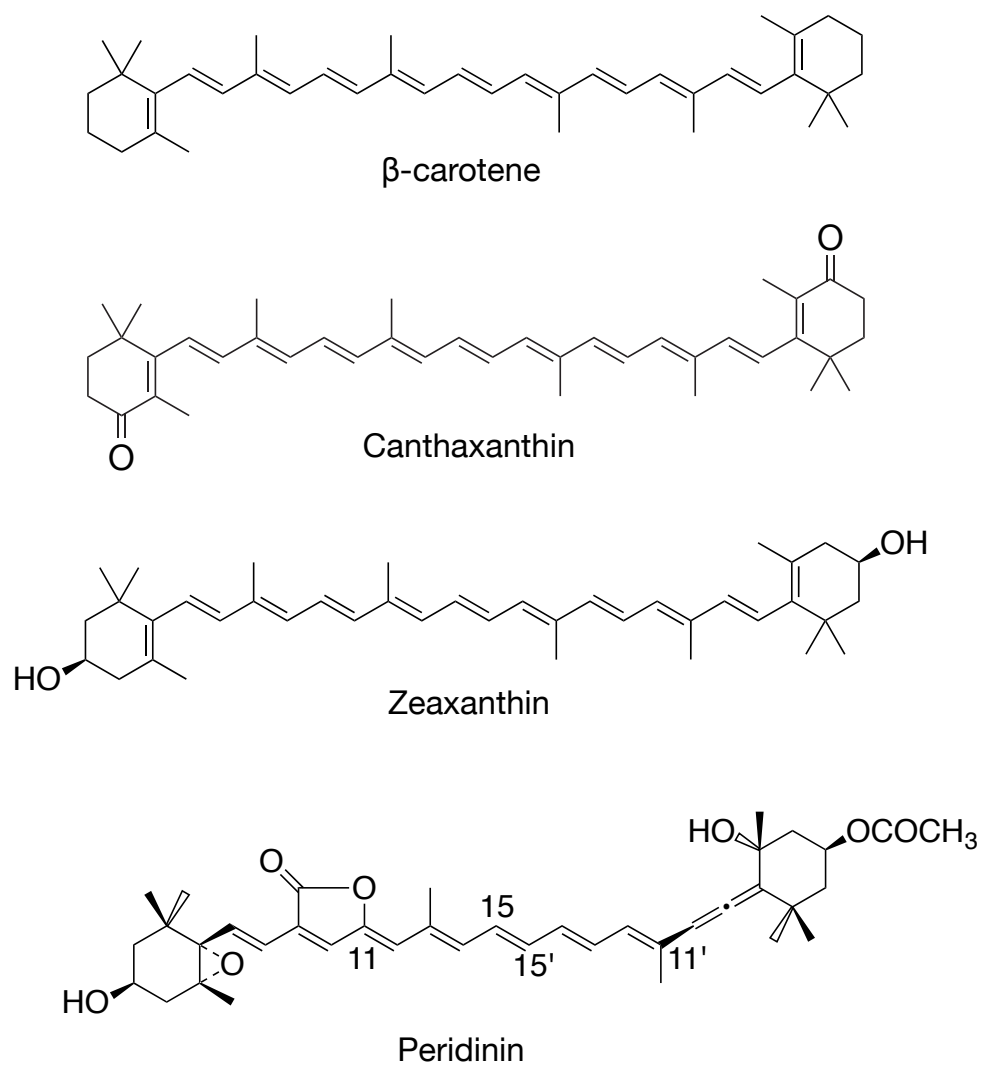


Figure 1.1. Structure of different carotenoids.

structures in the absorption spectrum, which are attributed to the combination of stretching motions of the C-C (1150 cm^{-1}) and C=C (1530 cm^{-1}) bonds of the polyene backbone.

1.3.1 Nonradiative Decay in Carotenoids

In carotenoids, the optically prepared S_2 state exhibits a very short lifetime ($<100\text{ fs}$) and relaxes to the S_1 state via ultrafast nonradiative processes.³³⁻³⁵ Several studies have shown that the decay of S_2 to S_1 involves an intermediate state that is detected in $< 20\text{ fs}$ after the optical preparation of S_2 .^{30,36,37} The structural and spectroscopic nature of this intermediate remains uncertain. One of the first experimental detection of the intermediate state was with resonance Raman excitation studies of all-trans-spheroidene by Koyama et al.³⁸ Further studies using sub-picosecond time-resolved experiments on all-trans-neurosporene, the group assigned the intermediate to a discrete $1B_u^-$ state^{39,40} as predicted by Tavan and Schulten.⁴¹ Subsequent transient absorption (TA) experiments conducted by Cerullo group using 15 fs pulses on β -carotene and lutein revealed that the S_2 state decays in 12 fs , giving rise to a distinctive electronic state called S_x , characterized by an excited state absorption in the $800\text{--}900\text{ nm}$ range.³⁶ Like earlier studies, this intermediate was also attributed to the $1B_u^-$ state. Two-dimensional electronic spectroscopy studies from Scholes group on LH2 light-harvesting protein have detected the X state in the carotenoid. The X state is attributed to the direct excitation of the $1B_u^-$ state and is considered to borrow oscillator strength from the nearby S_2 state via the Herzberg-Teller coupling.^{42,43} The assignment of the intermediate state to $1B_u^-$ applies only to planar carotenoid molecules with a C_{2h} geometry. However, studies on the ground-state structures in vacuum, solution

and proteins show that these carotenoids have asymmetric conformations with distortion along out-of-plane coordinates.^{31,44}

Earlier studies from our group raised the possibility that S_x should be assigned to a conformationally distorted S_2 structure moving along the out-of-plane coordinates of the isoprenoid backbone towards a conical intersection (CI) seam⁴ with the S_1 state.^{31,34,35} Upon photoexcitation, carotenoid molecules undergo displacements along the bond-alternation coordinates from the Franck-Condon geometry. These molecules then undergo vibrational motions along out-of-plane coordinates, leading to a twisted conformation (Figure 1.2). Fluorescence anisotropy measurements on β -carotene in aprotic solutions at room temperature show a 50° rotation of the emission transition dipole moment (TDM) relative to the Franck-Condon S_2 state, implying that the torsional and pyramidal distortions are initiated in the S_x state near the center of the isoprenoid backbone.²⁹ The first part of this dissertation addresses the nonradiative decay mechanisms of the ketocarotenoid, canthaxanthin involving an intermediate state, S_x , using multidimensional spectroscopic techniques. The nature of the bridging intermediate state, S_x , involved in the nonadiabatic mechanism of decay of optically prepared S_2 state to dark S_1 state in the ketocarotenoid is to be established. We address our proposal that S_x corresponds to conformationally distorted molecules evolving along the out-of-plane coordinates of the isoprenoid backbone near a low barrier between the planar and distorted conformations on the S_2 potential surface. The spectroscopic signature, electronic and vibrational dynamics of S_x formation will be addressed in the Chapter 2.

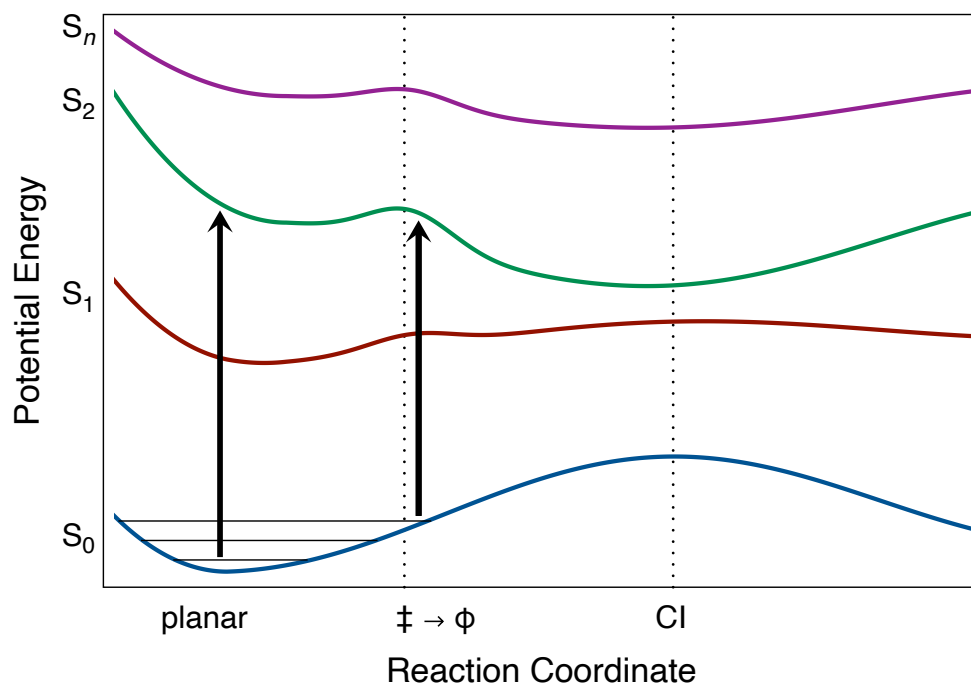


Figure 1.2. Schematic representations for the potential energy surfaces for the singlet states of a carotenoid, plotted here as a function of a reaction coordinate composed of sequential displacements from the Franck–Condon geometry of the optically prepared S_2 state with respect to the C–C and C=C stretching and out-of-plane (ϕ) coordinates of the isoprenoid backbone. Planar and distorted conformations are divided by a low barrier at the structure marked \ddagger on the reaction coordinate axis. The mixed S_2 , S_1 , and S_0 surfaces are proposed to converge near the geometry of the S_2 minimum owing to a conical intersection (CI) of the diabatic surfaces. Arrows indicate vertical optical transitions from planar and distorted conformations to the S_2 state. Adapted from Gurchiek et al.²⁹

1.4 Semiconductor Quantum Dots

Semiconductor materials have a fixed energy gap (or band gap) between the conduction band (CB) and valence band (VB), depending on the composition of the materials. However, when these semiconductor crystals are < 10 nm in size, their bandgaps are no longer fixed. In this size regime, semiconductor crystals exhibit *quantum size effects* and are therefore called quantum dots (QDs). QDs contain anywhere from 100 to 10000 atoms per nanocrystals. They can be viewed as materials between the molecules and bulk materials. Quantum effects are observed when the size of the nanocrystals is comparable to or smaller than the spatial separation between the electron and hole or the Bohr exciton radius (Figure 1.3). Their size-dependent electronic energy gaps have been modeled using the particle-in-a-sphere approximation.^{45,46} The energy of a particle in a sphere of radius R is strongly dependent on size and is proportional to $1/R^2$. The wavefunctions of the particle in a sphere are similar to the atomic orbitals of H-atom. Thus, they are labeled by quantum numbers n (1, 2,...), l (S, P, D, ...), and m . According to the derived selection rules, optical transitions occur only at energy levels with the same l quantum numbers. Owing to the quantum confinement in these particles, smaller QDs exhibit optical properties in the blue region of the spectra compared to larger ones.

QDs can be composed of single elements like Si or C, binary compounds of II-IV (e.g. CdSe, CdTe, ZnS, etc.), III-V elements (InP, GaN, GaP, etc.), and IV-VI elements (PbSe, PbTe, GeTe, etc.). Several synthetic approaches have been devised to prepare QDs with identical shapes, sizes, and properties. These approaches include physical processes such as molecular-beam-epitaxy (MBE)⁴⁸⁻⁵⁰ and metalorganic-chemical-vapor-deposition

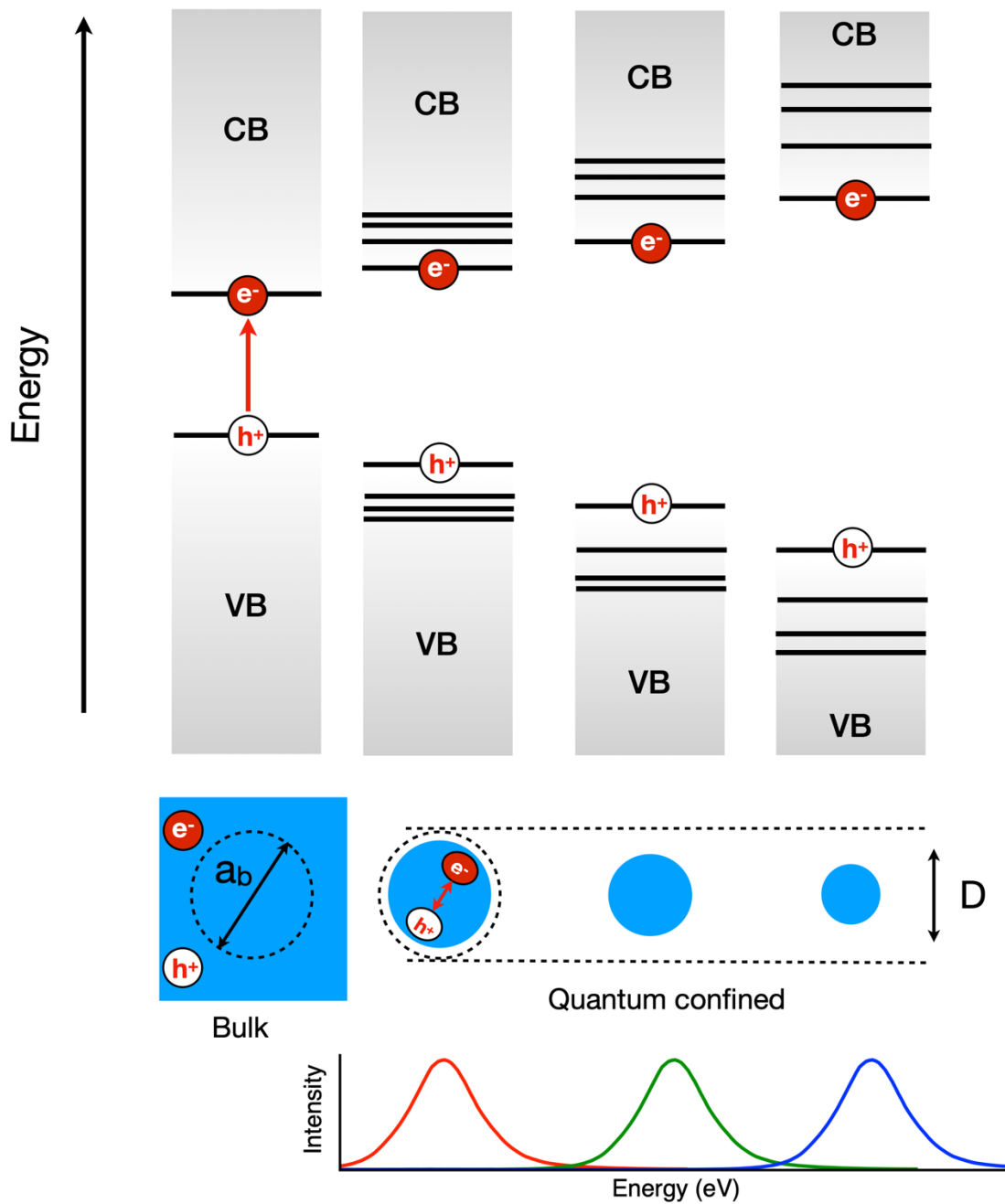


Figure 1.3. Illustration of the quantum confinement compared to the bulk semiconductor. When the spatial extent of wavefunction is smaller than the Bohr exciton radius (a_b), size-dependent optical properties are observed. Adapted from ref 47.⁴⁷

(MOCVD)^{50,51} and chemical methods such as colloidal nanocrystalline synthesis.⁵²⁻⁵⁴

This dissertation focusses on colloidal CdSe quantum dots. Colloidal CdSe quantum dots (QDs) have been widely recognized as a model system for the fundamental research of electronic and optical properties of QDs.⁵⁵ This is primarily because they can be synthesized with ease, resulting in high-quality, monodisperse QDs.

1.4.1 Electronic Structure and Surface of Colloidal CdSe QDs

To obtain a complete picture of the electronic structure and size-dependent optical properties, several optical spectroscopic techniques have been employed, including transient differential absorption,⁵⁶⁻⁶⁰ photoluminescence excitation^{56,61-63} and fluorescence line narrowing.^{64,65} In QDs, the VB contains a high density of states and the CB has a lower density of states. This means that the hole energy levels in the VB are closer to each other than the electronic energy levels in the CB. The electronic energy levels in the CB and the hole energy levels in the VB are shown in Figure 1.3. Electronic transitions following selection rules occur from the S and P states in the VB to the corresponding S and P states in the CB. The lower-energy exciton ($1S_{3/2} 1S_e$) is often termed as the band-edge exciton. Due to their tunable size-dependent energy gap, narrow-linewidth emission, surface chemistry, and charge transport properties, they have wide range of applications.⁴⁷ Some of the QD applications include their use in displays,⁶⁶⁻⁶⁹ lasers,⁷⁰⁻⁷² optical sensing and imaging,⁷³⁻⁷⁵ solar cells,⁷⁶⁻⁷⁸ and photo and electrocatalysis.⁷⁹⁻⁸¹

In colloidal solution, the surface of the quantum dots is passivated with organic molecules called surface capping ligands (Figure 1.4). These ligand molecules satisfy valencies of the surface atoms of the nanocrystal, protect the surface from the

surroundings, and control nucleation and kinetics during the colloidal synthesis.^{84–86} QDs have large surface-to-volume ratio and spatially confined excitonic wavefunctions.

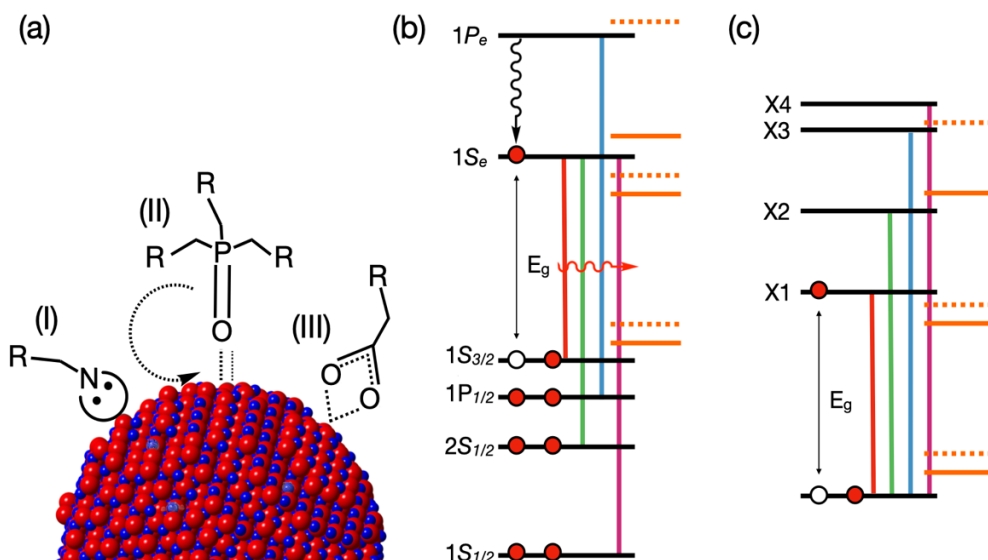


Figure 1.4. Illustration of different surface capping ligands and their possible coupling of vibrational modes with QD core electronic states.⁸² (a) Ligands, alkylamine (I), trioctylphosphineoxide (TOPO)(II), and alkylcarboxyl group (III), where R represents the alkyl chain, interacting with the surface of CdSe QDs. (b) Possible coupling of energy levels of ligand (solid line and dashed line representing bonding orbital and antibonding orbital, respectively) to core electronic states and (c) exciton manifold for excitons (electron hole pair) X1 to X4, as labelled. (Reproduced from Ryan Tilluck’s dissertation.⁸³)

Therefore, the properties of QDs can be significantly altered largely by modifying their surface using capping ligands. Surface-to-ligand bonding characteristics are classified into three categories by exploring the photoluminescence quantum yield dependence on ligands.^{82,86–88} They are L-type, X-type and Z-type based on Green’s Covalent Bond Classification.⁸⁹ The L-type ligands are neutral two-electron donors with lone pairs such as amines and phosphines. These ligands donate two electrons to the vacant orbitals of the metal ions. X-type ligands are one-electron Lewis bases, such as carboxylates, chlorides,

and sulfides. Two X-type ligands can coordinate with a divalent cation such as Cd^{2+} or Pb^{2+} to form covalent bonds.⁸⁶ In larger quantum dots, a surface monolayer of divalent cations is formed, which can coordinate with two X-type ligands to form MX_2 complexes, where M^{2+} is the divalent cation known as the Z-type ligand.⁹⁰ Due to the different types of interactions of ligands to the electronic core, the coupling strengths between the vibrational modes to electronic wavefunctions would be quite different.

1.4.2 Hot Carrier Cooling in QDs

Charge carriers are considered to be 'hot' when they occupy energy levels higher than the bandgap upon photoexcitation. They lose this excess energy via a nonradiative process called hot-carrier cooling. In a photoexcited quantum dot, the electrons that occupy higher energy levels ($1P_e$) above the band gap relax very quickly (subpicosecond regime) and nonradiatively to a lower energy state.⁹¹ Consequently, due to the irreversible loss of excitation energy, quantum dots exhibit low photoconversion efficiency in photovoltaic applications.⁹² Understanding the mechanisms of hot carrier cooling are of very high importance to ensure better performance of these materials in light harvesting applications.⁹³ Several mechanisms were proposed to understand the nature and mechanism of hot carrier cooling in recent years.^{91,94-96} Early theoretical studies proposed that the nonradiative relaxation is mediated by coupling of the exciton to lattice phonons.⁹⁴ But, the intraband spacings in the quantum dots are in the order of hundreds of meV while the energy of phonons is tens of meV (for example, phonons have an energy of 30 meV in CdSe QDs) which suggests that the relaxation could be a slow multiphonon process known as phonon-bottleneck.^{97,98} Alternative mechanisms proposed for the hot carrier cooling include nonradiative relaxation facilitated by Auger recombination.^{91,96} Auger

recombination occurs when the excess energy of photoexcited electron is transferred to hole in the valence band. The Auger process is mediated by strong Coulombic attraction between electrons and holes.^{99,100} The high density of states in the valence band of the QDs would facilitate the hole relaxation to the band edge. The hole relaxes nonradiatively by transferring energy to the lattice vibrations/phonons through a multiphonon process. In contradiction to Auger recombination mechanism, the hole relaxation rates observed in smaller quantum dots with higher energy gaps were much faster than larger quantum dots.^{91,100-102}

Further studies on hot carrier cooling studies on CdSe QDs with different surface modifications using inorganic and organic molecules revealed that surface ligands play an important role in the process.⁹⁹ These results have initiated investigations on the role of surface and surface-capping ligands in the hot carrier cooling. Guyot-Sionnest and coworkers studied the rates and mechanism of intraband relaxation in QDs capped with several ligands using transient absorption spectroscopy.^{95,103} They performed transient absorption studies on CdSe QDs capped with trioctylphosphine oxide (TOPO), oleic acid, oleylamine, thiols and concluded that the intraband relaxation rates are ligand-dependent in nature. They proposed that the intraband relaxation occurs via incoherent energy transfer to the vibrational modes of the surface ligand via dipole-dipole interaction.^{103,104}

Kambhampati group has shown that the electronic-to-vibrational energy transfer and Auger recombination mechanism are highly sensitive to QD's structure and surface chemistry. Their study shows that the intraband relaxation can be slowed down by decoupling the electronic states of the QD with vibrational states of the ligands using ZnS

layer.^{105,106} They point out that the surface vibrations induce nonadiabatic pathways for the hole relaxation in colloidal CdSe QDs.¹⁰⁵

Owing to spatially confined excitonic wavefunctions, the core electronic states are quantum mechanically mixed with ligand vibrational modes by bonding interactions, which leads to the delocalization of core electronic states to the surface of the QDs (Figure 1.4). Therefore, our group proposed that hot-carrier cooling in semiconductor quantum dots is mediated by a nonadiabatic radiationless mechanism, in which branching or promoting modes principally involve vibrational modes of surface capping ligands. In Tilluck et al.,¹⁰⁷ we provided the first evidence that coherent vibronic wavepacket motions involving mid-frequency modes of the surface ligands promote hot carrier cooling of electrons to the band edge by a nonadiabatic mechanism. The study involved understanding the mechanism of hot carrier cooling in hexadecylamine-capped CdSe QDs.

In the Chapter 3 of this dissertation, the nature of the structural, vibrational, and kinetic processes involved in the vibronic exciton mechanism of the nonradiative relaxation of excitons in oleate-capped QDs will be addressed. As an extension of the vibronic exciton mechanism, we propose that photoinduced charge transfer from the QD core to the surface ligand acceptor molecule is initiated via a coherent intermediate. In Chapter 4, the nature of the electronic-vibrational coupling that initiates charge transfer in the QD-acceptor complex needs to be established.

Studies of exciton relaxation dynamics in QDs were predominantly carried out using conventional spectroscopic techniques, such as time-resolved fluorescence studies and transient absorption spectroscopy using pulses of about ~ 100 fs long.^{91,95,99,103,104} Recently, several groups have employed two-dimensional electronic spectroscopy (2DES) to study

the energy transfer mechanisms in semiconductor nanocrystals.¹⁰⁸⁻¹¹³ Advantages of 2DES over conventional pump-probe spectroscopy are described in the experimental section. Several groups have detected electronic coherences between exciton levels of QDs and vibronic coherences arising from electron-phonon coupling.^{109,110,114,115} Earlier studies have also demonstrated the capability to distinguish the fine structure resulting from single and biexciton excitations in CdSe quantum dots, even in the presence of significant line broadening caused by variations in size and shape.¹¹⁶⁻¹¹⁸

In the next section, the experimental methods used to study the nonradiative relaxation mechanisms in carotenoids and semiconductor quantum dots are discussed. This section provides a brief introduction necessary for interpreting the results obtained from the multidimensional spectroscopy. An overview of third-order nonlinear signals, such as ground state bleaching, stimulated emission, excited state absorption, and quantum coherences and their corresponding Feynman diagrams will be discussed. Subsequently, the experimental implementation of the 2DES is described.

1.5 Multidimensional Electronic Spectroscopy

Two-dimensional electronic spectroscopy (2DES)¹²¹⁻¹²⁵ is a powerful technique to study the energy transfer mechanism in photosynthetic light harvesting^{11,126-131} and semiconductor quantum dots.^{107,108,111,113,116,132} Additionally, 2DES has also been employed to investigate the quantum coherences in ground and excited states in several systems. As discussed earlier, many studies on carotenoid photophysics and QDs have been conducted using ultrafast (~100 fs pulses) transient absorption and transient grating spectroscopy. 2DES offers several advantages over conventional transient absorption spectroscopy or femtosecond pump-probe spectroscopy. As a correlation spectroscopy technique, 2DES

projects out the correlation between the excitation energy and emitted energy, which is crucial for studying the energy transfer mechanisms in light harvesting. The exciton relaxation pathways manifest as the time evolution of off-diagonal crosspeaks in the 2D spectra.^{121,123} The broadband laser spectrum used to perform 2DES can span several excited states simultaneously. This enables us to probe the excitation energy flow through a cascade of energy levels and the subsequent relaxation to the ground state. The short pulses employed in 2DES provide partial relief from the inhomogeneous broadening of spectral features. Furthermore, short pulses that are smaller than the electronic dephasing of energy levels allow us to probe the electronic coherences. These short pulses also aid in accessing time-resolved vibrational coherences of energy up to 3000 cm⁻¹.

1.5.1 Excitation Pulse Sequence in 2DES

Two-dimensional electronic spectroscopy is a nonlinear spectroscopic technique performed using three very short pulses of duration, 6-7 fs scanned over two different time delays (Figure 1.5). The time delay between the first and second pulses is the coherence time τ , and that between the second and third pulses is the population time T . The first two pulses are the excitation pulses, and the third pulse is the probe pulse. The first two pump pulses are generated and the time delay between them are controlled using an adaptive pulse shaper. When the first pulse interacts with the sample, a coherence is created in the sample. Coherence is a linear superposition of ground and excited states. The coherence evolves with respect to the coherence time τ and undergoes free-induction decay. In the meantime, the second pulse interacts with the system and drive the evolving coherence into a population. The population created by the pulse pairs evolves along the population time T , after which a third pulse and a probe pulse interact with the system. This pulse

creates another coherence that in turn emits an electric field. The emitted signal travels along the probe beam and is detected as a pump-induced change in the probe transmission.

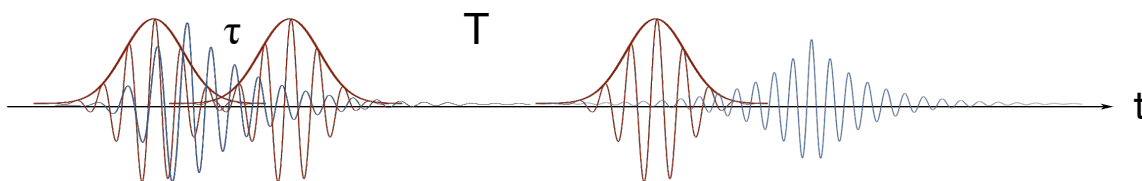


Figure 1.5. Broadband pulse sequences in the 2DES experiment. The red Gaussian pulse envelopes depict the excitation pulses in the pulse sequence. The blue signals represent the coherences emitted from the sample after the interaction of the pulses. The first pulse creates coherence that evolves over time, followed by the interaction of the second pulse to create a population. The third pulse interacts with the system to create another coherence and an evolving electric field (blue) is emitted from the sample. (Reproduced from Ryan Tilluck's dissertation,⁸³ adapted from work by the Jonas group.^{121,133})

1.5.2 Third-Order Nonlinear Optical Responses

The three types of signals detected using 2DES are: *ground-state bleaching (GSB)*, *stimulated emission (SE)*, and *excited-state absorption (ESA)*.^{122,133} The theoretical formulation for two-dimensional electronic correlations were developed by Jonas group and Fleming group.^{121,122,133,134} The phenomenological interpretation of the signals is adapted in this section are based on the works of Mukamel,¹³⁵ Hamm, and Zanni.¹³⁶ In order to provide a brief description of the above-mentioned signals, Albrecht wave mixing energy level diagram (WMEL)¹³⁷ and double-sided Feynman diagrams will be used in this section. In the WMEL diagrams, a system with three energy levels is used to understand the origin of the signals. The horizontal lines in the WMEL represent different energy levels in the system. The energy levels are labeled as '*g*' for ground state, '*1*' for the first excited energy level, and '*f*' for the second excited state at a higher energy level. The red arrows in

the WMEL represent the interaction of each laser pulse electric field with the system. In WMEL, the time progresses from left to right.

In the double-sided Feynman diagram, the left side represents the *ket* part of the wavefunction, whereas the right side represents the *bra* part of the wavefunction. The vertical lines show the evolution of the wavefunctions with each field-matter interaction. The field-matter interactions are represented by solid arrows and the emitted signal is represented by dashed arrows. The momentum vectors are represented by \mathbf{k}_n , where n is the order of their interactions with the system. To draw a connection between the two representations, the solid arrows within a WMEL represent a field matter interaction on the left side or *ket* side of the Feynman diagram, while the dashed arrow represents an interaction on the right side or *bra* side of the Feynman diagram.

Ground state bleaching (GSB) is the signal emitted by the system after the preparation of the population in the ground state during the first two pump interactions (Figure 1.6). The ground state is represented as gg in the system. The first interaction with the pump pulse creates a coherence in the system, where gg evolves to $1g$ or $g1$. The system evolves to $1g$ when the field-matter interaction occurs at the *ket* side of the Feynman diagram whereas the interaction at the *bra* side results in $g1$. This coherence evolves with respect to the coherence time τ . After a short interval of time, the second pulse interacts with the system and converts the evolving coherence into a population in the ground state, represented by gg . The third pulse creates another coherence $1g$ or $g1$ in the system which emits an electric field signal that can be detected. Depending on the phase of the two coherences created in the system, there are two types of pathways: rephasing and non-rephasing. When the coherences induced by the first and third pulses are of the same

phase, the resulting pathway is termed as non-rephasing pathway. In contrast, when the coherence has an opposite phase, the pathway is referred to as the rephasing pathway.

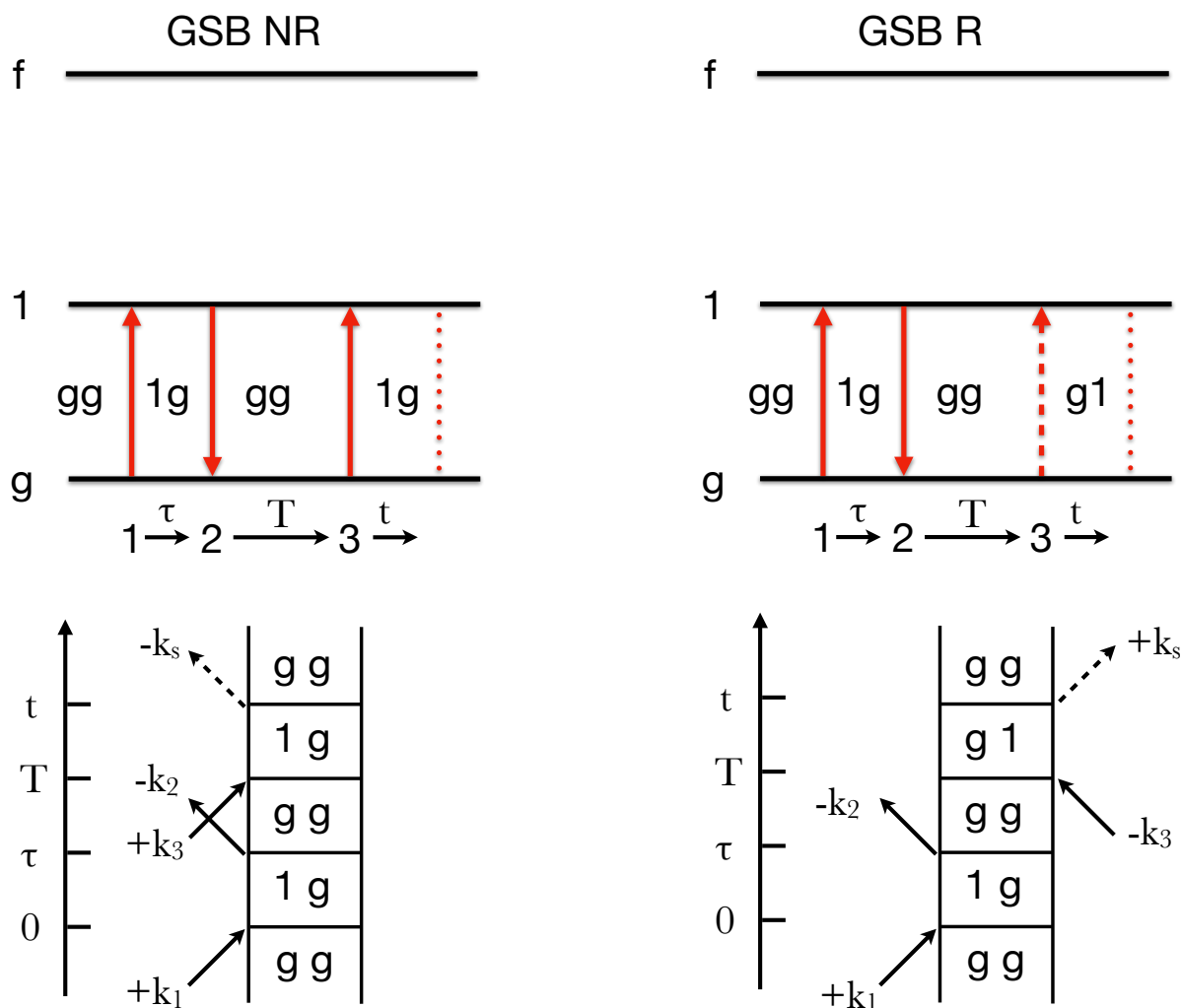


Figure 1.6. WMEL diagram (top) and Feynman diagram (bottom) of ground-state bleaching signal. The figures on the right correspond to the non-rephasing pathway, whereas those on the left correspond to the rephasing pathway. In the WMEL diagram, time evolves towards the right, and the field matter interactions are numbered as 1, 2, and 3 with marked time delays. The solid arrows represent the field-matter interaction on the *ket* side of the Feynman diagram, whereas the dashed arrows represent the interaction on the *bra* side. The dotted line in the WMEL and dashed arrow in the Feynman diagram represent the emitted signal after a series of field-matter interactions. The vertical line in the Feynman diagram represents the evolution of the time.

Stimulated emission (SE) is the signal emitted by the system after the preparation of the population in the excited state during the first two pump interactions (Figure 1.7). The first interaction with the pump pulse creates a coherence in the system where gg evolves to $1g$ or $g1$. The second pulse interacts with the system and converts the evolving coherence into a population in the excited state, which is represented by 11 . The third pulse drives an interaction downwards and creates another coherence $1g$ or $g1$ in the system; this coherence emits an electric field signal that can be detected as SE.

For excited state absorption (ESA), the first interaction with the pump pulse creates a coherence in the system, where gg evolves to $1g$ or $g1$ (Figure 1.8). The second pulse interacts with the system and converts the evolving coherence into a population in the excited state represented by 11 . The third pulse drives the population in the excited state to another excited state, f , to create coherences, $1f$ or $f1$, in the system. This coherence emits an electric field signal with a frequency of the energy difference between states 1 and f . This signal corresponds to the absorption from the first excited state of 1 .

By applying the law of conservation of momentum, the signals after three field-matter interactions can be detected along the directions, $\mathbf{k}_1 - \mathbf{k}_2 + \mathbf{k}_3$ for nonrephasing pathways and $-\mathbf{k}_1 + \mathbf{k}_2 + \mathbf{k}_3$ for the rephasing pathways. In practice, the beams are arranged in a boxcar geometry for the detection these signals. In boxcar experimental implementation, the first three pulses are aligned such that they form the corners of a box, while the signal is emitted along the fourth corner of the box. To detect the rephasing and nonrephasing pathways, the ordering of the first two pulses is interchanged.

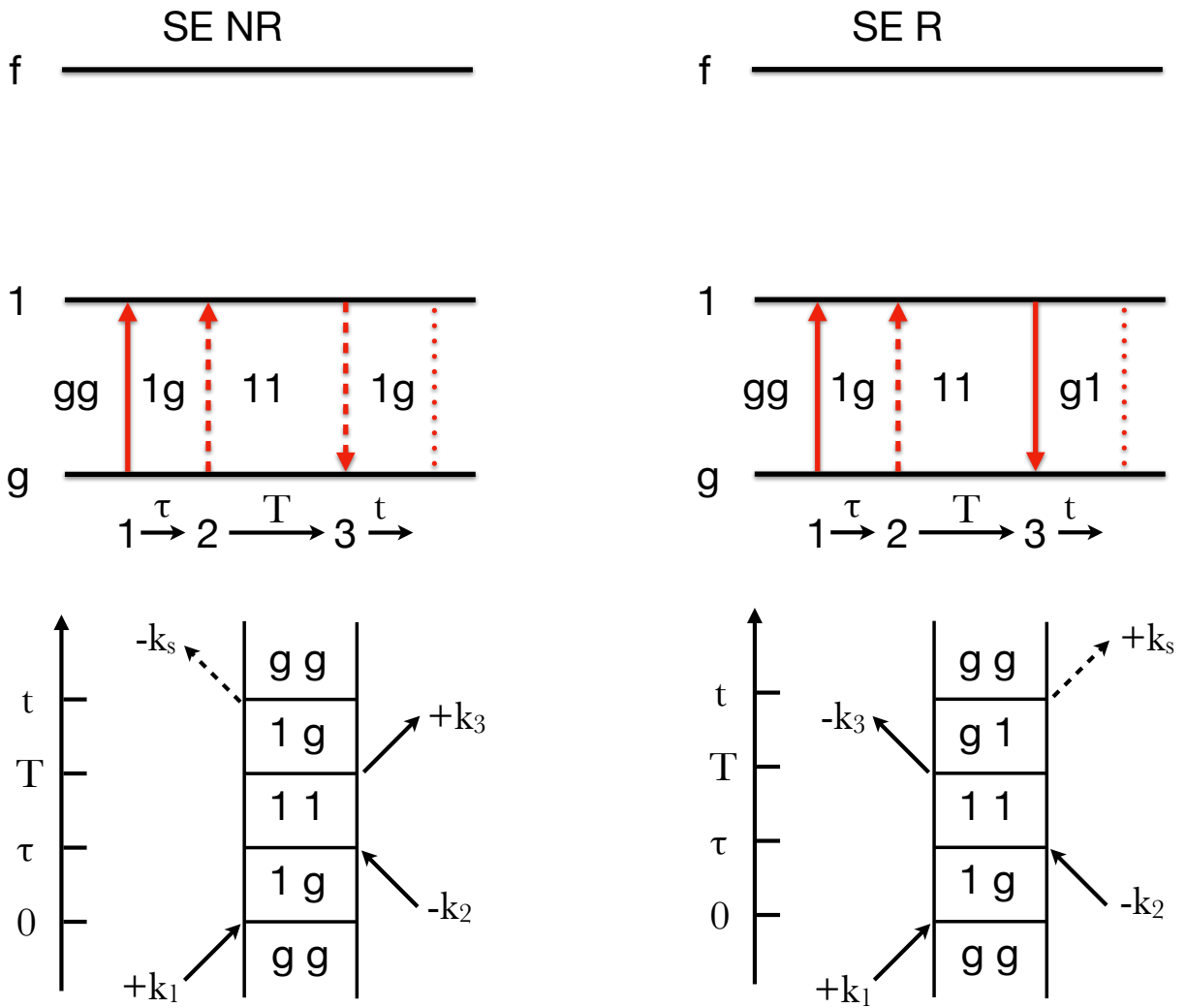


Figure 1.7. WMEL diagram (top) and Feynman diagram (bottom) of stimulated emission signals. The figures on the right correspond to the non-rephasing pathway, whereas those on the left correspond to the rephasing pathway.

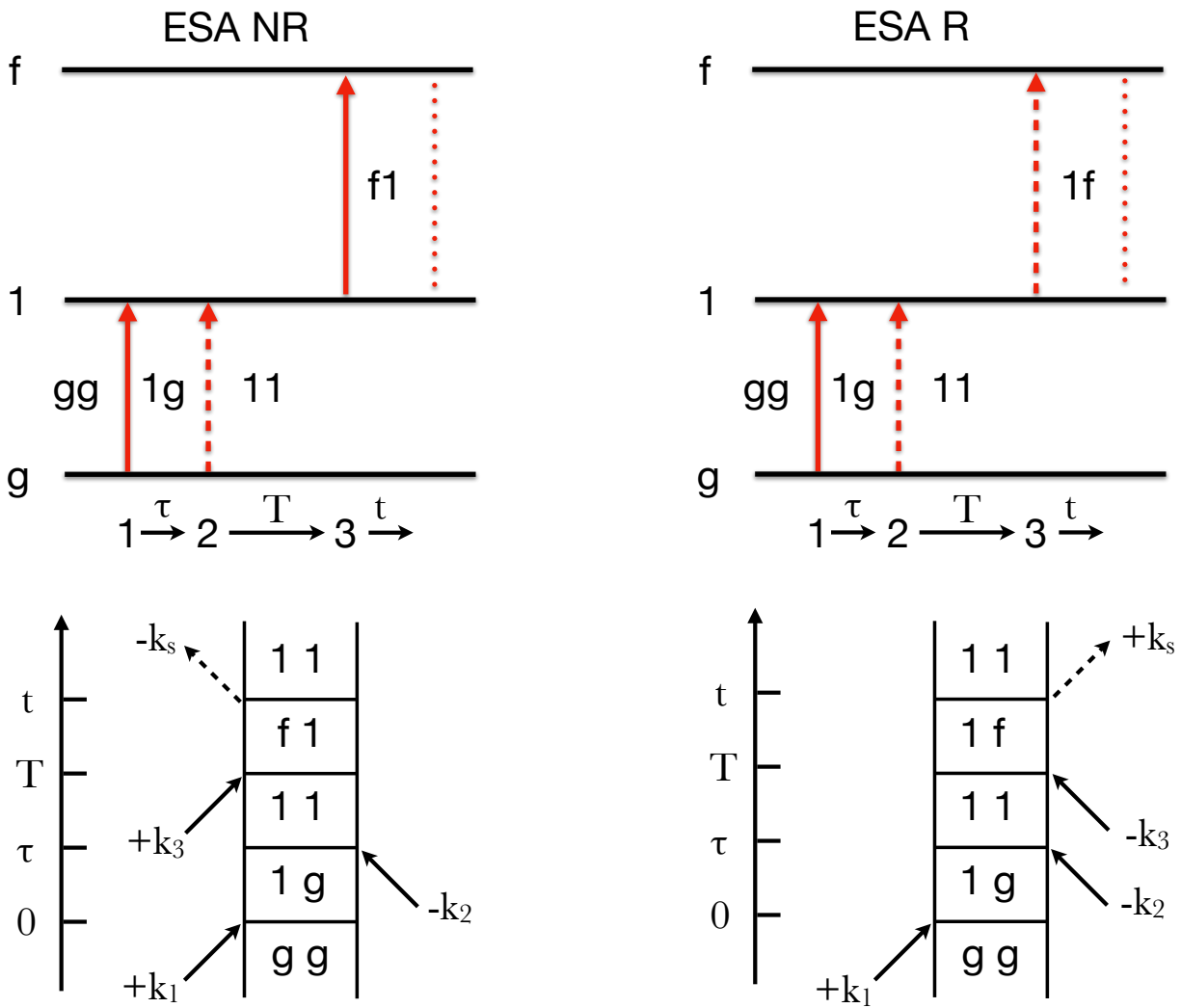


Figure 1.8. WMEL diagram (top) and Feynman diagram (bottom) of the excited-state absorption signal. The figures on the right correspond to the non-rephasing pathway, whereas those on the left correspond to the rephasing pathway.

1.5.3 Quantum Coherences in 2DES

The broadband spectrum accompanied by short pulses in the 2DES experiments spans a wide range of electronic states and vibrational states within both excited and ground states which allows us to monitor the evolution of coherent wavepacket motions.¹³⁸⁻¹⁴¹ In 2DES experiments, various kinds of coherences can be detected, including electronic coherence, vibrational coherence, and vibronic coherences.^{121,123,142,143} These coherences

exhibit distinct characteristics, such as differences in damping times and their position in the 2D spectrum.

Electronic coherences are observed in strongly coupled chromophores with a common ground state. They can be identified by the crosspeak positions and the frequency oscillations. For example, consider two electronic states, 1 and 2 , with a common ground state g . The first field-matter interaction creates coherence $g1$, followed by a second interaction that drives the system to 21 . In this case, a coherence is created between the excited states 1 and 2 which evolves along the population time, T . The frequency of this electronic coherence is equal to the energy difference between states, 1 and 2 (Figure 1.9). Since electronic coherences are observed owing to the superposition of electronic states, they are detected at the crosspeaks of the two states involved in the coherence in 2D spectra. The electronic coherences appear symmetric with respect to the diagonal. The damping times of these coherences are typically a few tens of femtoseconds.

Vibrational coherences, unlike electronic coherences, are observed between the vibrational energy levels in both the ground and excited states. Depending on the Franck-Condon overlap of the excited state energy levels, vibrational coherence peak patterns can be observed throughout the 2D spectrum.^{144,145} The peak patterns are spaced according to the vibrational quanta along the detection axis in the 2D spectrum. They exhibit a greater intensity along the lower energies of the excited states.^{144,146,147} As an example for the origin of vibrational coherence in the excited state or vibronic coherence, consider a two-level system with ground electronic state g and excited state 1 with vibrational levels $v = 0, 1$ (Figure 1.10).

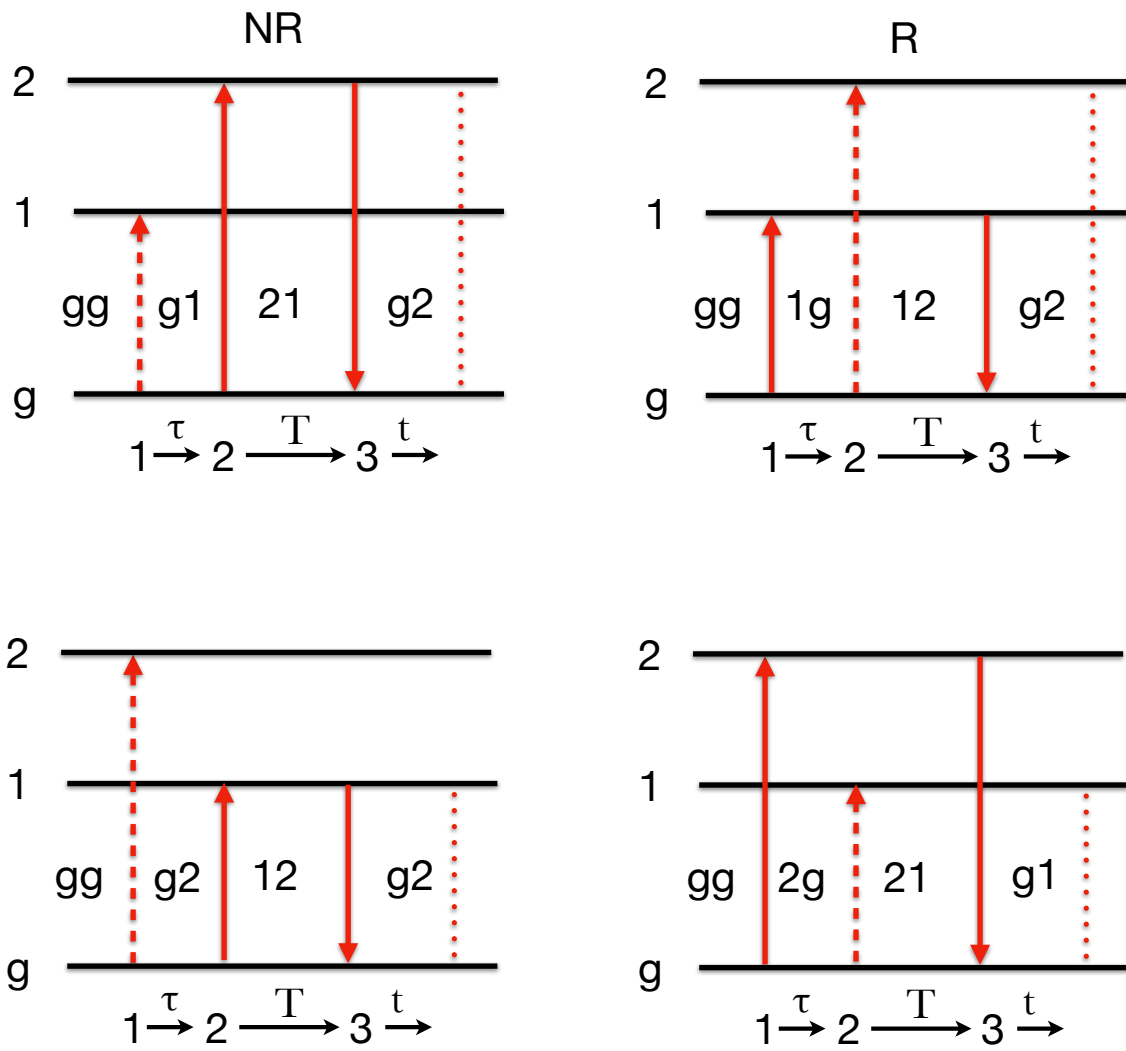


Figure 1.9. Example W MEL diagram for electronic coherences between excited electronic states, 1 and 2. The figures on the right correspond to the non-rephasing pathway, whereas those on the left correspond to the rephasing pathway.

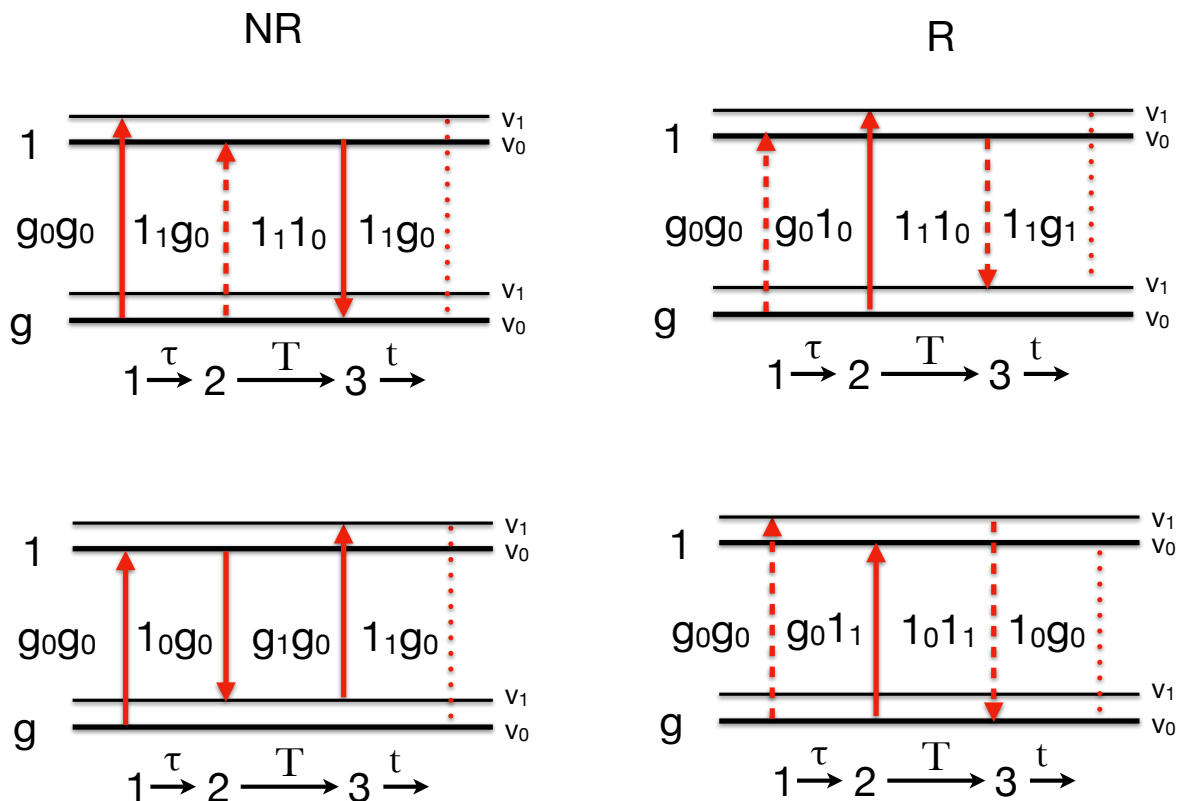


Figure 1.10. Example of W MEL diagram for vibrational coherences between ground and excited electronic state, 1 . Vibrational states are indicated by v_0 and v_1 . The figures on the right correspond to the non-rephasing pathway, whereas those on the left correspond to the rephasing pathway.

The first interaction drives the system to the first vibrational state of 1 represented by 1_1g_0 , and the second interaction drives the system to 1_11_0 . After the second interaction, a coherence is created between the vibrational states of the first excited state, 1 . This coherence evolves with respect to the population time T in the excited state, with the frequency of the energy difference between the two vibrational states. Vibronic coherences are characteristics of the excited state. They provide information on the vibrational motions activated in the excited states upon excitation. The damping times of vibronic coherences are dependent on the coupling between the electronic states and vibrational motions and the lifetime of the excited states.^{148,149} We have previously detected rapidly

damped vibronic wavepacket motions in the excited states in several light-harvesting systems undergoing rapid relaxation processes from the excited states.^{11,107,131} Some of the vibronic coherences are long lived and can be detected at the product states after the relaxation of excitation to the lower energy states.¹⁵⁰

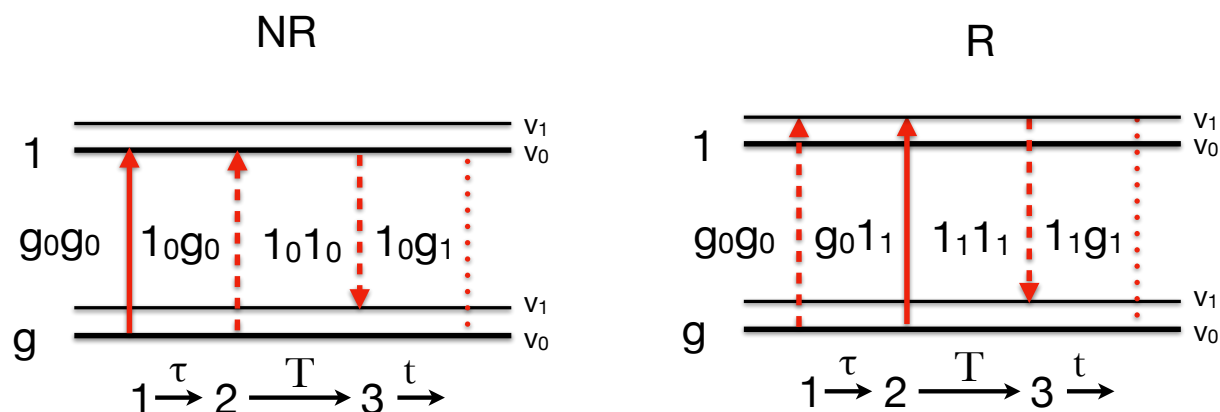


Figure 1.11. Example WMEL diagram for ground-state vibrational coherences (stimulated Raman) between ground and excited electronic state. Vibrational states are indicated by v_0 and v_1 . The figures on the right correspond to the non-rephasing pathway, whereas those on the left correspond to the rephasing pathway.

Ground-state vibrational coherences are observed when the first two excitation pulses create coherences in the ground vibrational states of the system. An example of ground-state coherence is stimulated Raman signals (Figure 1.11). The first interaction drives a coherence between the g_0 and 1_0 , and the second interaction creates a population in the 1_0 state. The third interaction drives the system to 1_0g_1 . This interaction creates a coherence between the vibrational levels in the ground state. The coherence that evolves with respect to T exhibits the frequency of vibrational motion in ground state with a damping time of vibrational dephasing (several hundreds of fs).

The natural light-harvesting systems are significantly complex in terms of presence of multiple electronic states and vibrational states. Hence, the vibronic coherences in these systems are much more intricate. The 2DES presents an additional advantage over TA to understand the vibronic mechanism of nonradiative relaxation by correlation of the coherences to excitation and detection energies. Short pulses aid in detection of a wide range of coherences from low to high frequencies which would not be resolved with 100 fs pulses.

1.6 Instrumentation

The earlier implementation of 2DES involved a diffractive optics-based approaches from the Miller group^{125,151,152} and Fleming group.¹²² The current 2DES setup in this thesis is based on the approach by Zanni and coworkers^{153,154} and Ogilvie and coworkers¹⁵⁵ where a pump-probe geometry is implemented (Figure 1.14). In the pump-probe configuration, the momentum vectors $\mathbf{k}_1 = \mathbf{k}_2$; therefore, the signal travels along \mathbf{k}_3 , which is the direction of the probe beam. In addition, the signal detected in pump-probe geometry is the sum of both nonrephasing and rephasing pathways. An adaptive pulse shaper is programmed to create a pulse pair in the pump beam.¹⁵⁶ The detection scheme in the current experimental setup employs a lock-in detection method following the work from Zigmantas and coworkers.¹⁵⁷

The excitation pulses are obtained from a Yb laser (Spectra-Physics Spirit-4W) with a 4 W output at 100 kHz repetition rate centered at 1040 nm. The noncollinear optical parametric amplifier (Spectra-Physics Spirit-NOPA-3H) pumped by the Yb laser is used to generate broadband pulses in the visible region. Inside the NOPA, the fundamental beam is split into two, one part passes through a white light continuum and the second part passes

through a series of second harmonic generation (SHG) and a third harmonic generation (THG). The third harmonic is mixed with the white light continuum at two amplification stages involving nonlinear crystals to generate a broadband (520-700 nm, centered at 600 nm) laser spectrum for the experiments (Figure 1.12).

The output beam from the NOPA is further split into two beams using a broadband dielectric beamsplitter (Layertec, Mellingen) to generate the pump and probe beams. Each pump and probe beams are processed using a programmable adaptive pulse shaper¹⁵⁶

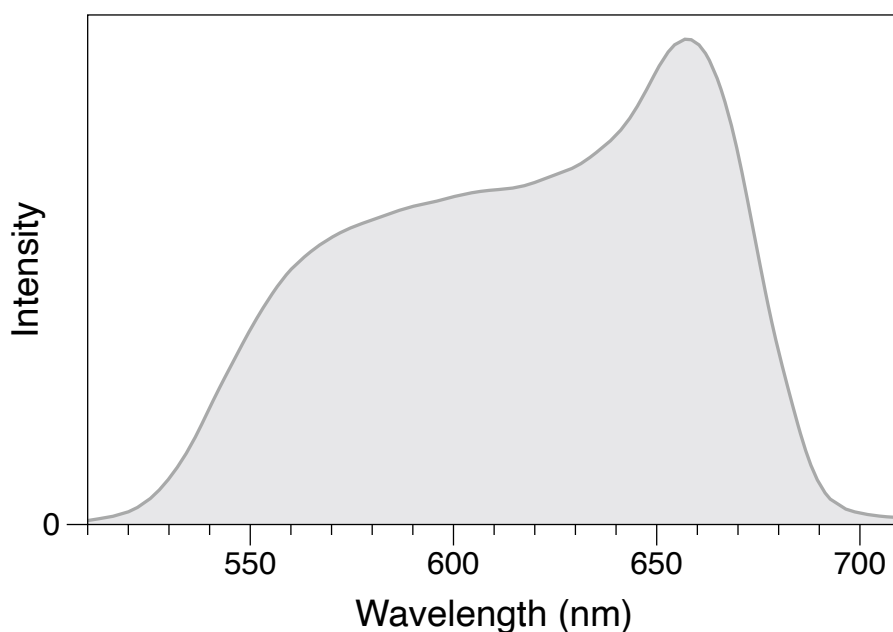


Figure 1.12. An example broadband laser spectrum in the range of 510-710 nm used in 2DES experiments. The full width at half maximum (FWHM) is 120 nm and the transform limited pulse duration was 6.8 fs.

(FemtoJock and FemtoJock P, Biophotonic Solutions Inc.). The pulse shapers consist of 128-pixel spatial light modulators (SLM) that are used to manipulate the phase and amplitude of the transmitted pulses. The FemtoJock on the pump beam contains two SLMs that are used to manipulate both the phase and amplitude of the pulses, whereas FemtoJock P has only one SLM that is used to manipulate only the phase of the pulses. Using the FemtoJock,

the pump pulses are split into two identical pump pulses, and the delay between them are varied by manipulating the phase and the amplitude of the electric field.

A detailed derivation of the pulse splitting to create a pulse replica and vary the time delay between them is provided in Ryan Tilluck's dissertation. In short, to create a pulse replica of incoming electric field, $E_{\text{in}}(\omega)$ and with a time delay τ and a phase difference ϕ between them, a phase and amplitude function, $M(\omega)$ is applied such that,

$$E_{\text{out}}(\omega) = M(\omega) E_{\text{in}}(\omega) \quad (1.1)$$

where $M(\omega) = |\cos(\omega\tau + \phi)|$ and phase mask, $\Phi(\omega) = \arg [1 + e^{-i(\omega\tau + \phi)}]$ and transmission mask, $T(\omega) = [1 + e^{-i(\omega\tau + \phi)}]^2$.

The adaptive pulse shapers use multiphoton intrapulse interference phase scan (MIIPS) to measure and compensate for the chirp on the pulses.¹⁵⁶ The output from thin second harmonic generation (SHG) crystal, beta-Barium borate crystal at sample position is used for the MIIPS scans. The pulse duration of the compressed pulses is characterized by interferometric autocorrelation of the pump pulse pairs. The SHG-frequency-resolved-optical gating (FROG) is also measured during the autocorrelation process (Figure 1.13). Additionally, multiple reflections on a pair of chirp mirrors (Ultrafast Innovations, Munich) also aid to compensate the chirp on. The combination of adaptive pulse shapers and chirp mirrors yield compressed pulses with transform-limited durations.

A thin achromatic half-wave retarder plate on the pump beam is used to rotate the polarization of the excitation pulses to magic angle (54.7°) with respect to the probe for the 2DES experiments on the QDs. The probe beam is horizontally polarized with respect to the optical bench. To calculate the nonlinear anisotropy signals, the polarization of the excitation pulses is at 45° with respect to the polarization of the probe beam. A polarization

of 45° will result in equal intensity of the electric field of the pulses along both the parallel and perpendicular directions. The population time T , that is, the time delay between the

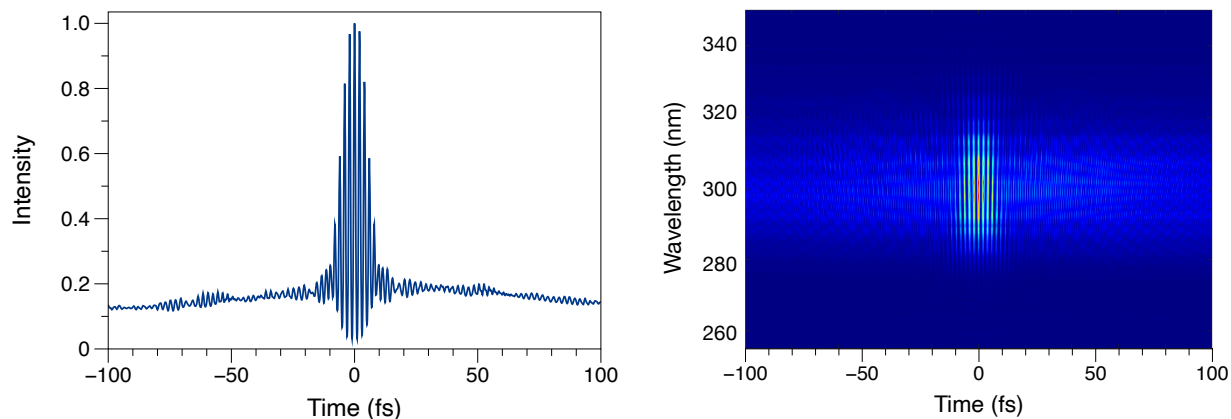


Figure 1.13. Interferometric autocorrelation of the pump pulses, determined as the integral of the SHG-FROG spectrogram¹⁵⁶ (left panel). SHG-FROG¹⁵⁸ spectrogram for the pump pulses, as measured with scanned pulse pairs prepared by the pump beam's pulse shaper in the 2DES spectrometer.

second and third pulses, is controlled using a time-of-flight delay stage controlled by nanometers (Melles Griot). The pump and probe beams are focused and overlapped just after the cuvette window to a beam size of 100 microns at the sample position using an off-axis parabolic mirror. The pump beam is terminated after the sample position.

The probe beam, along with the signal from the sample, was passed through an analyzer polarizer with its axis aligned parallel to the polarization of the probe beam. This analyzer polarizer can be rotated using a motorized stage (Thorlabs) to select the linear components of the signals parallel and perpendicular to the polarization of the excitation pulses. Further, the beam is focused using lens and spatially filtered to eliminate any straylight using a lens. The spectrograph of the detection scheme consists of a spherical mirror followed by a 300 gr/mm grating, which disperses the beam into the constituent

wavelengths. Another spherical mirror is used to focus the beam on to the CCD (Newton Andor 940).

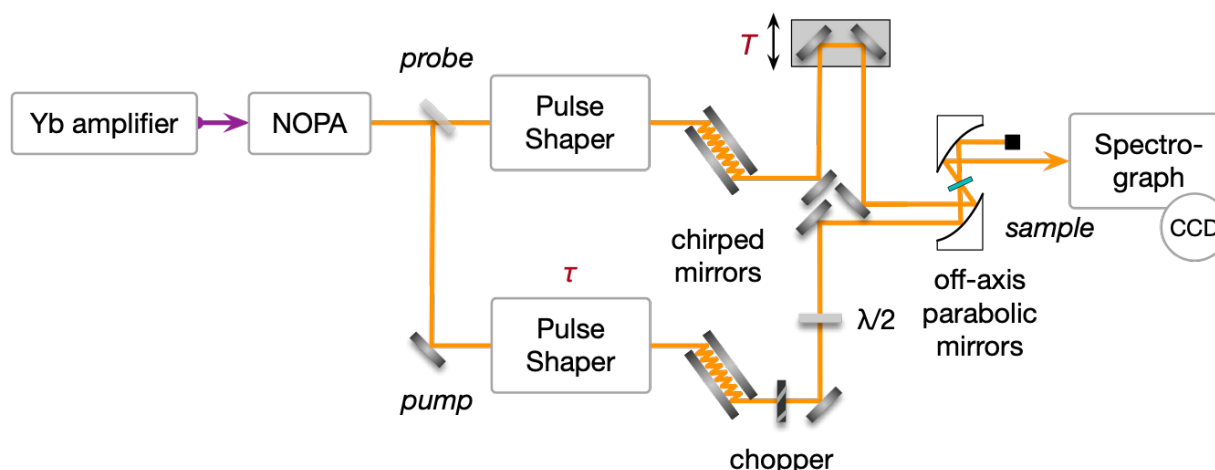


Figure 1.14. Instrumentation set up used in the 2DES experiment. The Yb laser (4W, 100 kHz, 1040 nm) is pumped to a NOPA to generate broadband visible pulses ranging from 500-700 nm. The adaptive pulse shapers and the pairs of chirp mirrors compress the pulse to the transform limit. The pulse shaper on the pump beam is manipulated to create a pulse pair and vary the time between the pump pulses. A time-of-flight delay stage is used to vary the time delay between the pump and the probe beams. The emitted signals are collected using a home-built spectrograph and a fast CCD.

The 2D spectrometer employs lock-in detection scheme based on design by Augulis and Zigmantas¹⁵⁷ to detect the signals. The pump beam is amplitude-modulated using a mechanical chopper (Thorlabs) at a frequency of 400 Hz. In the pump-probe geometry of the experimental setup, the signals are heterodyned along the probe beam. The CCD acquires spectra at a rate of 1 kHz. The CCD comprises of 2048 W \times 512 H pixels, of which the bottom 10 pixels are used to detect the signals. The signals are detected as pump induced change in probe intensity at the chopper frequency of 400 Hz. The signal intensity on the CCD is binned by a factor of 8 and undergoes shift register to single line. The CCD is set to acquire 800 spectra with a 1 millisecond exposure for each spectrum. The signals are

isolated by performing a fast Fourier transform (FFT) of the time series of intensity obtained at each detection wavelength.

1.7 Data Processing and Analysis

During a 2DES experiment, a series of spectra are collected for each population time T . The time T spans from -3 picosecond (ps) to several tens or hundreds of ps depending on the nature of the sample and the nature of the relaxation kinetics being probed. These spectra contain the amplitudes detected for each binned pixel of the CCD for each time point of the coherence time τ . In the experiments presented in this thesis, there were 101 spectra for τ time points (0-50 fs in 0.5 fs steps). Each data file consists of 256 x 101 array of amplitudes where 256 is the total number of the binned CCD pixels. The data processing is performed using MATLAB scripts in the initial stages.

The amplitude of the FFT for pump-induced change in probe-transmission undergoes decays with respect to time and damps out at about 20 fs (Figure 1.15). An offset subtraction is carried out to bring the oscillations centered around zero. The time points after the decay are removed and replaced with zeros. Owing to the symmetric nature of the signal oscillations, the amplitude at each detection wavelength is mirrored and concatenated. The data is further zero-padded to create 2^N data points for the FFT analysis. The FFT output contains both real and imaginary components, out of which the real components are extracted and plotted as a contour with excitation energy on the x-axis and detection energy on the y-axis. These steps are repeated for each T to generate a series of 2D spectra and associated data. Several iterations of the T -scans are analyzed individually and averaged to increase the signal-to-noise ratio of a particular run. The 95% confidence interval of the amplitudes at each T point is also calculated during the averaging process.

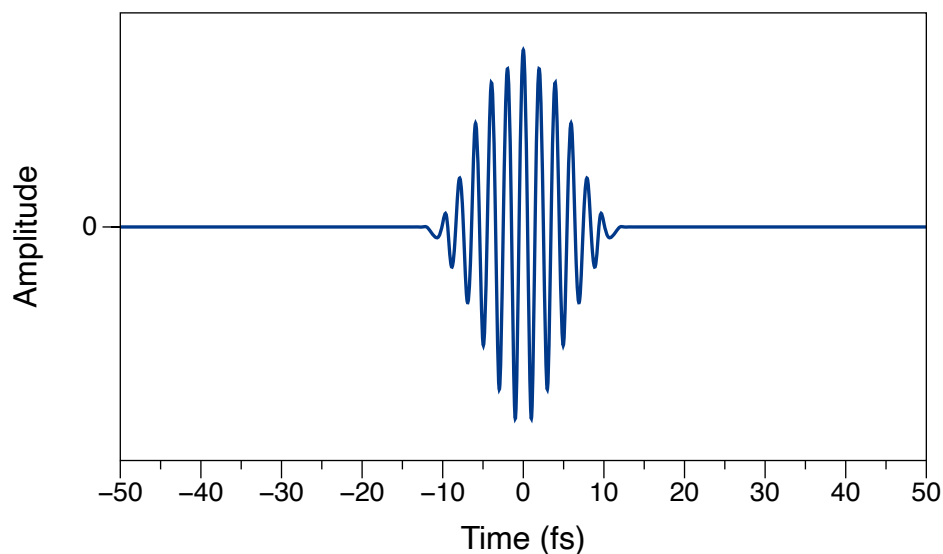


Figure 1.15. Evolution of the amplitude obtained after FFT of the pump-induced change in probe-transmission with respect to the time, integrated along the detection axis for CdSe QDs with 7 fs pulses. The coherent oscillations are isolated, mirrored and zero-padded prior to the FFT process.

To perform kinetic modeling of the energy relaxation processes in these systems, a part of the response along a desired excitation energy is averaged. This data contains amplitudes of the signals at all the detection wavelengths that evolve with time T . The signals are subjected to global modeling¹⁵⁹ performed using the CarpetView software package (Light Conversion). The kinetic models are subtracted from the signal responses at each coordinate in the 2D spectra to obtain the residuals. These residuals are subjected to FFT using Julia codes to obtain information on the frequencies of the modulations. Specific details of the coherence analysis used for each study are described in the following chapters. To characterize the frequencies and damping times of the modulations, linear prediction singular value decomposition (LPSVD) analysis is performed using MATLAB scripts.

REFERENCES

- (1) Ishizaki, A.; Fleming, G. R. Quantum Coherence in Photosynthetic Light Harvesting. *Annu. Rev. Condens. Matter Phys.* **2012**, *3* (1), 333–361.
- (2) Chenu, A.; Scholes, G. D. Coherence in Energy Transfer and Photosynthesis. *Annu. Rev. Phys. Chem.* **2015**, *66*, 69–96.
- (3) Rafiq, S.; Scholes, G. D. From Fundamental Theories to Quantum Coherences in Electron Transfer. *J. Am. Chem. Soc.* **2019**, *141* (2), 708–722.
- (4) Levine, B. G.; Martínez, T. J. Isomerization through Conical Intersections. *Annu. Rev. Phys. Chem.* **2007**, *58*, 613–634.
- (5) Nelson, T.; Fernandez-Alberti, S.; Roitberg, A. E.; Tretiak, S. Nonadiabatic Excited-State Molecular Dynamics: Modeling Photophysics in Organic Conjugated Materials. *Acc. Chem. Res.* **2014**, *47* (4), 1155–1164.
- (6) Tammie R. Nelson, Alexander J. White, Josiah A. Bjorgaard, Andrew E. Sifain, Yu Zhang, Benjamin Nebgen, Sebastian Fernandez-Alberti, Dmitry Mozyrsky, Adrian E. Roitberg*, and Sergei Tretiak*. Non-Adiabatic Excited-State Molecular Dynamics: Theory and Applications for Modeling Photophysics in Extended Molecular Materials. *Chemical reviews* **2020**, *120* (4), 2215–2287.
- (7) Domcke, W.; Yarkony, D.; Köppel, H. *Conical Intersections: Electronic Structure, Dynamics & Spectroscopy*; World Scientific, 2004.
- (8) Scholes, G. D.; Fleming, G. R.; Chen, L. X.; Aspuru-Guzik, A.; Buchleitner, A.; Coker, D. F.; Engel, G. S.; van Grondelle, R.; Ishizaki, A.; Jonas, D. M.; Lundeen, J. S.; McCusker, J. K.; Mukamel, S.; Ogilvie, J. P.; Olaya-Castro, A.; Ratner, M. A.; Spano, F. C.; Whaley, K. B.; Zhu, X. Using Coherence to Enhance Function in Chemical and Biophysical Systems. *Nature* **2017**, *543* (7647), 647–656.
- (9) Romero, E.; Augulis, R.; Novoderezhkin, V. I.; Ferretti, M.; Thieme, J.; Zigmantas, D.; van Grondelle, R. Quantum Coherence in Photosynthesis for Efficient Solar Energy Conversion. *Nat. Phys.* **2014**, *10* (9), 676–682.
- (10) Beljonne, D.; Pourtois, G.; Silva, C.; Hennebicq, E.; Herz, L. M.; Friend, R. H.; Scholes, G. D.; Setayesh, S.; Mullen, K.; Bredas, J. L. Interchain vs. Intrachain Energy Transfer in Acceptor-Capped Conjugated Polymers. *Proc. Natl. Acad. Sci. U. S. A.* **2002**, *99* (17), 10982–10987.
- (11) Tilluck, R. W.; Ghosh, S.; Guberman-Pfeffer, M. J.; Roscioli, J. D.; Gurchiek, J. K.; LaFountain, A. M.; Frank, H. A.; Gascón, J. A.; Beck, W. F. Interexciton Nonradiative

Relaxation Pathways in the Peridinin-Chlorophyll Protein. *Cell Reports Physical Science* **2021**, 2 (3), 100380.

- (12) Corrales, M. E.; González-Vázquez, J.; Balerdi, G.; Solá, I. R.; de Nalda, R.; Bañares, L. Control of Ultrafast Molecular Photodissociation by Laser-Field-Induced Potentials. *Nat. Chem.* **2014**, 6 (9), 785–790.
- (13) Saveant, J. M. Electron Transfer, Bond Breaking, and Bond Formation. *Acc. Chem. Res.* **1993**, 26 (9), 455–461.
- (14) Brumer, P.; Shapiro, M. Coherence Chemistry: Controlling Chemical Reactions [with Lasers]. *Acc. Chem. Res.* **1989**, 22 (12), 407–413.
- (15) Kerfeld, C. A. Water-Soluble Carotenoid Proteins of Cyanobacteria. *Arch. Biochem. Biophys.* **2004**, 430 (1), 2–9.
- (16) Blount, J. D. Carotenoids and Life-History Evolution in Animals. *Arch. Biochem. Biophys.* **2004**, 430 (1), 10–15.
- (17) Wu, Y. P.; Krogmann, D. W. The Orange Carotenoid Protein of *Synechocystis* PCC 68031. Publication No. 15377.1. *Biochimica et Biophysica Acta (BBA) - Bioenergetics* **1997**, 1322 (1), 1–7.
- (18) Kerfeld, C. A.; Sawaya, M. R.; Brahmandam, V.; Cascio, D.; Ho, K. K.; Trevithick-Sutton, C. C.; Krogmann, D. W.; Yeates, T. O. The Crystal Structure of a Cyanobacterial Water-Soluble Carotenoid Binding Protein. *Structure* **2003**, 11 (1), 55–65.
- (19) Boulay, C.; Abasova, L.; Six, C.; Vass, I.; Kirilovsky, D. Occurrence and Function of the Orange Carotenoid Protein in Photoprotective Mechanisms in Various Cyanobacteria. *Biochim. Biophys. Acta* **2008**, 1777 (10), 1344–1354.
- (20) Wilson, A.; Punginelli, C.; Gall, A.; Bonetti, C.; Alexandre, M.; Routaboul, J.-M.; Kerfeld, C. A.; van Grondelle, R.; Robert, B.; Kennis, J. T. M.; Kirilovsky, D. A Photoactive Carotenoid Protein Acting as Light Intensity Sensor. *Proc. Natl. Acad. Sci. U. S. A.* **2008**, 105 (33), 12075–12080.
- (21) Wilson, A.; Kinney, J. N.; Zwart, P. H.; Punginelli, C.; D'Haene, S.; Perreau, F.; Klein, M. G.; Kirilovsky, D.; Kerfeld, C. A. Structural Determinants Underlying Photoprotection in the Photoactive Orange Carotenoid Protein of Cyanobacteria. *J. Biol. Chem.* **2010**, 285 (24), 18364–18375.
- (22) Bao, H.; Melnicki, M. R.; Kerfeld, C. A. Structure and Functions of Orange Carotenoid Protein Homologs in Cyanobacteria. *Curr. Opin. Plant Biol.* **2017**, 37, 1–9.

- (23) Leverenz, R. L.; Sutter, M.; Wilson, A.; Gupta, S.; Thurotte, A.; Bourcier de Carbon, C.; Petzold, C. J.; Ralston, C.; Perreau, F.; Kirilovsky, D.; Kerfeld, C. A. PHOTOSYNTHESIS. A 12 Å Carotenoid Translocation in a Photoswitch Associated with Cyanobacterial Photoprotection. *Science* **2015**, *348* (6242), 1463–1466.
- (24) Gupta, S.; Guttman, M.; Leverenz, R. L.; Zhumadilova, K.; Pawlowski, E. G.; Petzold, C. J.; Lee, K. K.; Ralston, C. Y.; Kerfeld, C. A. Local and Global Structural Drivers for the Photoactivation of the Orange Carotenoid Protein. *Proc. Natl. Acad. Sci. U. S. A.* **2015**, *112* (41), E5567-74.
- (25) Kirilovsky, D.; Kerfeld, C. A. Cyanobacterial Photoprotection by the Orange Carotenoid Protein. *Nat Plants* **2016**, *2* (12), 16180.
- (26) Domínguez-Martín, M. A.; Sauer, P. V.; Kirst, H.; Sutter, M.; Bina, D.; Greber, B. J.; Nogales, E.; Polívka, T.; Kerfeld, C. A. Structures of a Phycobilisome in Light-Harvesting and Photoprotected States. *Nature* **2022**, *609* (7928), 835–845.
- (27) Polívka, T.; Sundström, V. Ultrafast Dynamics of Carotenoid Excited States-from Solution to Natural and Artificial Systems. *Chem. Rev.* **2004**, *104* (4), 2021–2071.
- (28) Fiedor, L.; Dudkowiak, A.; Pilch, M. The Origin of the Dark S1 State in Carotenoids: A Comprehensive Model. *J. R. Soc. Interface* **2019**, *16* (158), 20190191.
- (29) Gurchiek, J. K.; Rose, J. B.; Guberman-Pfeffer, M. J.; Tilluck, R. W.; Ghosh, S.; Gascón, J. A.; Beck, W. F. Fluorescence Anisotropy Detection of Barrier Crossing and Ultrafast Conformational Dynamics in the S2 State of β -Carotene. *J. Phys. Chem. B* **2020**. <https://doi.org/10.1021/acs.jpcc.0c06961>.
- (30) Polívka, T.; Sundström, V. Dark Excited States of Carotenoids: Consensus and Controversy. *Chem. Phys. Lett.* **2009**, *477* (1), 1–11.
- (31) Beck, W. F.; Bishop, M. M.; Roscioli, J. D.; Ghosh, S.; Frank, H. A. Excited State Conformational Dynamics in Carotenoids: Dark Intermediates and Excitation Energy Transfer. *Arch. Biochem. Biophys.* **2015**, *572*, 175–183.
- (32) Christensen, R. L.; Faksh, A.; Meyers, J. A.; Samuel, I. D. W.; Wood, P.; Schrock, R. R.; Hultsch, K. C. Optical Spectroscopy of Long Polyenes. *J. Phys. Chem. A* **2004**, *108* (40), 8229–8236.
- (33) Macpherson, A. N.; Gillbro, T. Solvent Dependence of the Ultrafast S2–S1 Internal Conversion Rate of β -Carotene. *J. Phys. Chem. A* **1998**, *102* (26), 5049–5058.
- (34) Ghosh, S.; Roscioli, J. D.; Bishop, M. M.; Gurchiek, J. K.; LaFountain, A. M.; Frank, H. A.; Beck, W. F. Torsional Dynamics and Intramolecular Charge Transfer in the S2

- (1(1)Bu(+)) Excited State of Peridinin: A Mechanism for Enhanced Mid-Visible Light Harvesting. *J. Phys. Chem. Lett.* **2016**, *7* (18), 3621–3626.
- (35) Ghosh, S.; Bishop, M. M.; Roscioli, J. D.; Mueller, J. J.; Shepherd, N. C.; LaFountain, A. M.; Frank, H. A.; Beck, W. F. Femtosecond Heterodyne Transient-Grating Studies of Nonradiative Decay of the S₂ (1(1)Bu(+)) State of β -Carotene: Contributions from Dark Intermediates and Double-Quantum Coherences. *J. Phys. Chem. B* **2015**, *119* (47), 14905–14924.
- (36) Cerullo, G.; Polli, D.; Lanzani, G.; De Silvestri, S.; Hashimoto, H.; Cogdell, R. J. Photosynthetic Light Harvesting by Carotenoids: Detection of an Intermediate Excited State. *Science* **2002**, *298* (5602), 2395–2398.
- (37) Sugisaki, M.; Fujiwara, M.; Nair, S. V.; Ruda, H. E.; Cogdell, R. J.; Hashimoto, H. Excitation-Energy Dependence of Transient Grating Spectroscopy in β -Carotene. *Phys. Rev. B Condens. Matter* **2009**, *80* (3), 035118.
- (38) Sashima, T.; Nagae, H.; Kuki, M.; Koyama, Y. A New Singlet-Excited State of All-Trans-Spheroidene as Detected by Resonance-Raman Excitation Profiles. *Chem. Phys. Lett.* **1999**, *299* (2), 187–194.
- (39) Tavan, P.; Schulten, K. Electronic Excitations in Finite and Infinite Polyenes. *Phys. Rev. B Condens. Matter* **1987**, *36* (8), 4337–4358.
- (40) Tavan, P.; Schulten, K. The Low-Lying Electronic Excitations in Long Polyenes: A PPP-MRD-CI Study. *J. Chem. Phys.* **1986**, *85* (11), 6602–6609.
- (41) Zhang, J.-P.; Inaba, T.; Watanabe, Y.; Koyama, Y. Sub-Picosecond Time-Resolved Absorption Spectroscopy of All-Trans-Neurosporene in Solution and Bound to the LH2 Complex from Rhodobacter Sphaeroides G1C. *Chem. Phys. Lett.* **2000**, *331* (2), 154–162.
- (42) Ostroumov, E. E.; Mulvaney, R. M.; Cogdell, R. J.; Scholes, G. D. Broadband 2D Electronic Spectroscopy Reveals a Carotenoid Dark State in Purple Bacteria. *Science* **2013**, *340* (6128), 52–56.
- (43) Ostroumov, E. E.; Mulvaney, R. M.; Anna, J. M.; Cogdell, R. J.; Scholes, G. D. Energy Transfer Pathways in Light-Harvesting Complexes of Purple Bacteria as Revealed by Global Kinetic Analysis of Two-Dimensional Transient Spectra. *J. Phys. Chem. B* **2013**, *117* (38), 11349–11362.
- (44) Fiedor, L.; Heriyanto; Fiedor, J.; Pilch, M. Effects of Molecular Symmetry on the Electronic Transitions in Carotenoids. *J. Phys. Chem. Lett.* **2016**, *7* (10), 1821–1829.

- (45) Efros, A. L.; Efros, Al. L. Interband Absorption of Light in a Semiconductor Sphere. *Sov. Phys. Semicond.* **1982**, 16 (7), 772-775.
- (46) Brus, L. E. Electron–Electron and Electron-Hole Interactions in Small Semiconductor Crystallites: The Size Dependence of the Lowest Excited Electronic State. *J. Chem. Phys.* **1984**, 80 (9), 4403–4409.
- (47) García de Arquer, F. P.; Talapin, D. V.; Klimov, V. I.; Arakawa, Y.; Bayer, M.; Sargent, E. H. Semiconductor Quantum Dots: Technological Progress and Future Challenges. *Science* **2021**, 373 (6555). <https://doi.org/10.1126/science.aaz8541>.
- (48) Kwoen, J.; Jang, B.; Lee, J.; Kageyama, T.; Watanabe, K.; Arakawa, Y. All MBE Grown InAs/GaAs Quantum Dot Lasers on on-Axis Si (001). *Opt. Express* **2018**, 26 (9), 11568–11576.
- (49) Franchi, S.; Trevisi, G.; Seravalli, L.; Frigeri, P. Quantum Dot Nanostructures and Molecular Beam Epitaxy. *Prog. Cryst. Growth Charact. Mater.* **2003**, 47 (2), 166–195.
- (50) Petroff, P. M.; DenBaars, S. P. MBE and MOCVD Growth and Properties of Self-Assembling Quantum Dot Arrays in III-V Semiconductor Structures. *Superlattices Microstruct.* **1994**, 15 (1), 15.
- (51) Sellin, R. L.; Ribbat, C.; Bimberg, D.; Rinner, F.; Konstanzer, H.; Kelemen, M. T.; Mikulla, M. High-Reliability MOCVD-Grown Quantum Dot Laser. *Electronics Letters; Stevenage* **2002**, 38 (16), 1–2.
- (52) Murray, C. B.; Norris, D. J.; Bawendi, M. G. Synthesis and Characterization of Nearly Monodisperse CdE (E = Sulfur, Selenium, Tellurium) Semiconductor Nanocrystallites. *J. Am. Chem. Soc.* **1993**, 115 (19), 8706–8715.
- (53) Dabbousi, B. O.; Rodriguez-Viejo, J.; Mikulec, F. V.; Heine, J. R.; Mattoussi, H.; Ober, R.; Jensen, K. F.; Bawendi, M. G. (CdSe)ZnS Core–Shell Quantum Dots: Synthesis and Characterization of a Size Series of Highly Luminescent Nanocrystallites. *J. Phys. Chem. B* **1997**, 101 (46), 9463–9475.
- (54) Murray, C. B.; Kagan, C. R.; Bawendi, M. G. Synthesis and Characterization of Monodisperse Nanocrystals and Close-Packed Nanocrystal Assemblies. *Annu. Rev. Mater. Sci.* **2000**, 30 (1), 545–610.
- (55) Klimov, V. I. *Nanocrystal Quantum Dots*; CRC Press, 2017.
- (56) Norris, D. J.; Sacra, A.; Murray, C. B.; Bawendi, M. G. Measurement of the Size Dependent Hole Spectrum in CdSe Quantum Dots. *Phys. Rev. Lett.* **1994**, 72 (16), 2612–2615.

- (57) Alivisatos, A. P.; Harris, A. L.; Levinos, N. J.; Steigerwald, M. L.; Brus, L. E. Electronic States of Semiconductor Clusters: Homogeneous and Inhomogeneous Broadening of the Optical Spectrum. *J. Chem. Phys.* **1988**, *89* (7), 4001–4011.
- (58) Roussignol, P.; Ricard, D.; Flytzanis, C.; Neuroth, N. Phonon Broadening and Spectral Hole Burning in Very Small Semiconductor Particles. *Phys. Rev. Lett.* **1989**, *62* (3), 312–315.
- (59) Bawendi, M. G.; Wilson, W. L.; Rothberg, L.; Carroll, P. J.; Jedju, T. M.; Steigerwald, M. L.; Brus, L. E. Electronic Structure and Photoexcited-Carrier Dynamics in Nanometer-Size CdSe Clusters. *Phys. Rev. Lett.* **1990**, *65* (13), 1623–1626.
- (60) Kang, K.; Kepner, A. D.; Hu, Y. Z.; Koch, S. W.; Peyghambarian, N.; Li, C.-Y.; Takada, T.; Kao, Y.; Mackenzie, J. D. Room Temperature Spectral Hole Burning and Elimination of Photodarkening in Sol-Gel Derived CdS Quantum Dots. *Appl. Phys. Lett.* **1994**, *64* (12), 1487–1489.
- (61) Norris, D. J.; Bawendi, M. G. Measurement and Assignment of the Size-Dependent Optical Spectrum in CdSe Quantum Dots. *Phys. Rev. B Condens. Matter* **1996**, *53* (24), 16338–16346.
- (62) Hoheisel, W.; Colvin, V. L.; Johnson, C. S.; Alivisatos, A. P. Threshold for Quasicontinuum Absorption and Reduced Luminescence Efficiency in CdSe Nanocrystals. *J. Chem. Phys.* **1994**, *101* (10), 8455–8460.
- (63) Rodrigues, P. A. M.; Tamulaitis, G.; Yu, P. Y.; Risbud, S. H. Size Selective Photoluminescence Excitation Spectroscopy in CdSe Nanocrystals. *Solid State Commun.* **1995**, *94* (8), 583–587.
- (64) Kuno, M.; Lee, J. K.; Dabbousi, B. O.; Mikulec, F. V.; Bawendi, M. G. The Band Edge Luminescence of Surface Modified CdSe Nanocrystallites: Probing the Luminescing State. *J. Chem. Phys.* **1997**, *106* (23), 9869–9882.
- (65) Norris, D. J.; Efros, A. L.; Rosen, M.; Bawendi, M. G. Size Dependence of Exciton Fine Structure in CdSe Quantum Dots. *Phys. Rev. B Condens. Matter* **1996**, *53* (24), 16347–16354.
- (66) B.-L. Huang, T.-L. Guo, S. Xu, Y. Ye, E.-G. Chen, Z.-X. Lin. Color Converting Film With Quantum-Dots for the Liquid Crystal Displays Based on Inkjet Printing. *IEEE Photonics J.* **2019**, No. 11, 1–9.
- (67) He S.-T. Wu, H. C. Recent Advances on Quantum-Dot-Enhanced Liquid-Crystal Displays. *IEEE J. Sel. Top. Quantum Electron.* **2017**, No. 23, 1–11.

- (68) Dai, X.; Deng, Y.; Peng, X.; Jin, Y. Quantum-Dot Light-Emitting Diodes for Large-Area Displays: Towards the Dawn of Commercialization. *Adv. Mater.* **2017**, *29* (14). <https://doi.org/10.1002/adma.201607022>.
- (69) Bozyigit, D.; Yarema, O.; Wood, V. Origins of Low Quantum Efficiencies in Quantum Dot LEDs. *Adv. Funct. Mater.* **2013**, *23* (24), 3024–3029.
- (70) Park, Y.-S.; Bae, W. K.; Baker, T.; Lim, J.; Klimov, V. I. Effect of Auger Recombination on Lasing in Heterostructured Quantum Dots with Engineered Core/Shell Interfaces. *Nano Lett.* **2015**, *15* (11), 7319–7328.
- (71) García-Santamaría, F.; Chen, Y.; Vela, J.; Schaller, R. D.; Hollingsworth, J. A.; Klimov, V. I. Suppressed Auger Recombination in “Giant” Nanocrystals Boosts Optical Gain Performance. *Nano Lett.* **2009**, *9* (10), 3482–3488.
- (72) Fan, F.; Voznyy, O.; Sabatini, R. P.; Bicanic, K. T.; Adachi, M. M.; McBride, J. R.; Reid, K. R.; Park, Y.-S.; Li, X.; Jain, A.; Quintero-Bermudez, R.; Saravanapavanantham, M.; Liu, M.; Korkusinski, M.; Hawrylak, P.; Klimov, V. I.; Rosenthal, S. J.; Hoogland, S.; Sargent, E. H. Continuous-Wave Lasing in Colloidal Quantum Dot Solids Enabled by Facet-Selective Epitaxy. *Nature* **2017**, *544* (7648), 75–79.
- (73) Lim, H.; Tsao, S.; Zhang, W.; Razeghi, M. High-Performance InAs Quantum-Dot Infrared Photodetectors Grown on InP Substrate Operating at Room Temperature. *Appl. Phys. Lett.* **2007**, *90* (13), 131112.
- (74) Konstantatos, G.; Howard, I.; Fischer, A.; Hoogland, S.; Clifford, J.; Klem, E.; Levina, L.; Sargent, E. H. Ultrasensitive Solution-Cast Quantum Dot Photodetectors. *Nature* **2006**, *442* (7099), 180–183.
- (75) Ren, A.; Yuan, L.; Xu, H.; Wu, J.; Wang, Z. Recent Progress of III–V Quantum Dot Infrared Photodetectors on Silicon. *J. Mater. Chem.* **2019**, *7* (46), 14441–14453.
- (76) McDonald, S. A.; Konstantatos, G.; Zhang, S.; Cyr, P. W.; Klem, E. J. D.; Levina, L.; Sargent, E. H. Solution-Processed PbS Quantum Dot Infrared Photodetectors and Photovoltaics. *Nat. Mater.* **2005**, *4* (2), 138–142.
- (77) Kirmani, A. R.; Luther, J. M.; Abolhasani, M.; Amassian, A. Colloidal Quantum Dot Photovoltaics: Current Progress and Path to Gigawatt Scale Enabled by Smart Manufacturing. *ACS Energy Lett.* **2020**, *5* (9), 3069–3100.
- (78) Rath, A. K.; Bernechea, M.; Martinez, L.; de Arquer, F. P. G.; Osmond, J.; Konstantatos, G. Solution-Processed Inorganic Bulk Nano-Heterojunctions and Their Application to Solar Cells. *Nat. Photonics* **2012**, *6* (8), 529–534.

- (79) Li, X.-B.; Tung, C.-H.; Wu, L.-Z. Semiconducting Quantum Dots for Artificial Photosynthesis. *Nature Reviews Chemistry* **2018**, *2* (8), 160–173.
- (80) Wu, H.-L.; Li, X.-B.; Tung, C.-H.; Wu, L.-Z. Semiconductor Quantum Dots: An Emerging Candidate for CO₂ Photoreduction. *Adv. Mater.* **2019**, *31* (36), e1900709.
- (81) Chen, X.; Li, N.; Kong, Z.; Ong, W.-J.; Zhao, X. Photocatalytic Fixation of Nitrogen to Ammonia: State-of-the-Art Advancements and Future Prospects. *Mater. Horiz.* **2018**, *5* (1), 9–27.
- (82) Lifshitz, E. Evidence in Support of Exciton to Ligand Vibrational Coupling in Colloidal Quantum Dots. *J. Phys. Chem. Lett.* **2015**, *6* (21), 4336–4347.
- (83) Tilluck, R. VIBRONIC COHERENCE IN LIGHT-HARVESTING PROTEINS AND SEMICONDUCTOR NANOMATERIALS. Doctor of Philosophy, Michigan State University, 2020.
- (84) Boles, M. A.; Ling, D.; Hyeon, T.; Talapin, D. V. The Surface Science of Nanocrystals. *Nat. Mater.* **2016**, *15* (2), 141–153.
- (85) Yin, Y.; Alivisatos, A. P. Colloidal Nanocrystal Synthesis and the Organic-Inorganic Interface. *Nature* **2005**, *437* (7059), 664–670.
- (86) Owen, J. Nanocrystal Structure. The Coordination Chemistry of Nanocrystal Surfaces. *Science* **2015**, *347* (6222), 615–616.
- (87) Kalyuzhny, G.; Murray, R. W. Ligand Effects on Optical Properties of CdSe Nanocrystals. *J. Phys. Chem. B* **2005**, *109* (15), 7012–7021.
- (88) Munro, A. M.; Jen-La Plante, I.; Ng, M. S.; Ginger, D. S. Quantitative Study of the Effects of Surface Ligand Concentration on CdSe Nanocrystal Photoluminescence. *J. Phys. Chem. C* **2007**, *111* (17), 6220–6227.
- (89) Green, M. L. H. A New Approach to the Formal Classification of Covalent Compounds of the Elements. *J. Organomet. Chem.* **1995**, *500* (1), 127–148.
- (90) Anderson, N. C.; Hendricks, M. P.; Choi, J. J.; Owen, J. S. Ligand Exchange and the Stoichiometry of Metal Chalcogenide Nanocrystals: Spectroscopic Observation of Facile Metal-Carboxylate Displacement and Binding. *J. Am. Chem. Soc.* **2013**, *135* (49), 18536–18548.
- (91) Klimov, V. I.; McBranch, D. W. Femtosecond P-to-S Electron Relaxation in Strongly Confined Semiconductor Nanocrystals. *Phys. Rev. Lett.* **1998**, *80* (18), 4028–4031.

- (92) Tisdale, W. A.; Williams, K. J.; Timp, B. A.; Norris, D. J.; Aydil, E. S.; Zhu, X.-Y. Hot-Electron Transfer from Semiconductor Nanocrystals. *Science* **2010**, *328* (5985), 1543–1547.
- (93) Fu, J.; Xu, Q.; Han, G.; Wu, B.; Huan, C. H. A.; Leek, M. L.; Sum, T. C. Hot Carrier Cooling Mechanisms in Halide Perovskites. *Nat. Commun.* **2017**, *8* (1), 1300.
- (94) Bockelmann, U.; Bastard, G. Phonon Scattering and Energy Relaxation in Two-, One-, and Zero-Dimensional Electron Gases. *Phys. Rev. B Condens. Matter* **1990**, *42* (14), 8947–8951.
- (95) Guyot-Sionnest, P.; Shim, M.; Matranga, C.; Hines, M. Intraband Relaxation in CdSe Quantum Dots. *Phys. Rev. B Condens. Matter* **1999**, *60* (4), R2181–R2184.
- (96) Efros, A. L.; Kharchenko, V. A.; Rosen, M. Breaking the Phonon Bottleneck in Nanometer Quantum Dots: Role of Auger-like Processes. *Solid State Commun.* **1995**, *93* (4), 281–284.
- (97) Inoshita, T.; Sakaki, H. Electron-Phonon Interaction and the so-Called Phonon Bottleneck Effect in Semiconductor Quantum Dots. *Physica B Condens. Matter* **1996**, *227* (1), 373–377.
- (98) Inoshita, T.; Sakaki, H. Electron Relaxation in a Quantum Dot: Significance of Multiphonon Processes. *Phys. Rev. B Condens. Matter* **1992**, *46* (11), 7260–7263.
- (99) Klimov, V. I.; Mikhailovsky, A. A.; McBranch, D. W.; Leatherdale, C. A.; Bawendi, M. G. Mechanisms for Intraband Energy Relaxation in Semiconductor Quantum Dots: The Role of Electron-Hole Interactions. *Phys. Rev. B Condens. Matter* **2000**, *61* (20), R13349–R13352.
- (100) Klimov, V. I., VI; Mikhailovsky, A. A.; McBranch, D. W.; Leatherdale, C. A.; Bawendi, M. G. Quantization of Multiparticle Auger Rates in Semiconductor Quantum Dots. *Science* **2000**, *287* (5455), 1011–1013.
- (101) Cooney, R. R.; Sewall, S. L.; Dias, E. A.; Sagar, D. M.; Anderson, K. E. H.; Kambhampati, P. Unified Picture of Electron and Hole Relaxation Pathways in Semiconductor Quantum Dots. *Phys. Rev. B Condens. Matter* **2007**, *75* (24), 245311.
- (102) Klimov, V. I.; McBranch, D. W.; Leatherdale, C. A.; Bawendi, M. G. Electron and Hole Relaxation Pathways in Semiconductor Quantum Dots. *Phys. Rev. B Condens. Matter* **1999**, *60* (19), 13740–13749.
- (103) Guyot-Sionnest, P.; Wehrenberg, B.; Yu, D. Intraband Relaxation in CdSe Nanocrystals and the Strong Influence of the Surface Ligands. *J. Chem. Phys.* **2005**, *123* (7), 074709.

- (104) Pandey, A.; Guyot-Sionnest, P. Slow Electron Cooling in Colloidal Quantum Dots. *Science* **2008**, *322* (5903), 929–932.
- (105) Cooney, R. R.; Sewall, S. L.; Anderson, K. E. H.; Dias, E. A.; Kambhampati, P. Breaking the Phonon Bottleneck for Holes in Semiconductor Quantum Dots. *Phys. Rev. Lett.* **2007**, *98* (17), 177403.
- (106) Kambhampati, P. Hot Exciton Relaxation Dynamics in Semiconductor Quantum Dots: Radiationless Transitions on the Nanoscale. *J. Phys. Chem. C* **2011**, *115* (45), 22089–22109.
- (107) Tilluck, R. W.; Mohan T M, N.; Hetherington, C. V.; Leslie, C. H.; Sil, S.; Frazier, J.; Zhang, M.; Levine, B. G.; Van Patten, P. G.; Beck, W. F. Vibronic Excitons and Conical Intersections in Semiconductor Quantum Dots. *J. Phys. Chem. Lett.* **2021**, *12* (39), 9677–9683.
- (108) Turner, D. B.; Hassan, Y.; Scholes, G. D. Exciton Superposition States in CdSe Nanocrystals Measured Using Broadband Two-Dimensional Electronic Spectroscopy. *Nano Lett.* **2012**, *12* (2), 880–886.
- (109) Caram, J. R.; Zheng, H.; Dahlberg, P. D.; Rolczynski, B. S.; Griffin, G. B.; Fidler, A. F.; Dolzhanikov, D. S.; Talapin, D. V.; Engel, G. S. Persistent Inter-Excitonic Quantum Coherence in CdSe Quantum Dots. *J. Phys. Chem. Lett.* **2014**, *5* (1), 196–204.
- (110) Caram, J. R.; Zheng, H.; Dahlberg, P. D.; Rolczynski, B. S.; Griffin, G. B.; Dolzhanikov, D. S.; Talapin, D. V.; Engel, G. S. Exploring Size and State Dynamics in CdSe Quantum Dots Using Two-Dimensional Electronic Spectroscopy. *J. Chem. Phys.* **2014**, *140* (8), 084701.
- (111) Cassette, E.; Dean, J. C.; Scholes, G. D. Two-Dimensional Visible Spectroscopy For Studying Colloidal Semiconductor Nanocrystals. *Small* **2016**, *12* (16), 2234–2244.
- (112) Lenngren, N.; Abdellah, M. A.; Zheng, K.; Al-Marri, M. J.; Zigmantas, D.; Žídek, K.; Pullerits, T. Hot Electron and Hole Dynamics in Thiol-Capped CdSe Quantum Dots Revealed by 2D Electronic Spectroscopy. *Phys. Chem. Chem. Phys.* **2016**, *18* (37), 26199–26204.
- (113) Collini, E.; Gattuso, H.; Levine, R. D.; Remacle, F. Ultrafast Fs Coherent Excitonic Dynamics in CdSe Quantum Dots Assemblies Addressed and Probed by 2D Electronic Spectroscopy. *J. Chem. Phys.* **2021**, *154* (1), 014301.
- (114) Griffin, G. B.; Ithurria, S.; Dolzhanikov, D. S.; Linkin, A.; Talapin, D. V.; Engel, G. S. Two-Dimensional Electronic Spectroscopy of CdSe Nanoparticles at Very Low Pulse Power. *J. Chem. Phys.* **2013**, *138* (1), 014705.

- (115) Collini, E.; Gattuso, H.; Kolodny, Y.; Bolzonello, L.; Volpato, A.; Fridman, H. T.; Yochelis, S.; Mor, M.; Dehnel, J.; Lifshitz, E.; Paltiel, Y.; Levine, R. D.; Remacle, F. Room-Temperature Inter-Dot Coherent Dynamics in Multilayer Quantum Dot Materials. *J. Phys. Chem. C* **2020**, *124* (29), 16222–16231.
- (116) Wong, C. Y.; Scholes, G. D. Using Two-Dimensional Photon Echo Spectroscopy to Probe the Fine Structure of the Ground State Biexciton of CdSe Nanocrystals. *J. Lumin.* **2011**, *131* (3), 366–374.
- (117) Wong, C. Y.; Scholes, G. D. Biexcitonic Fine Structure of CdSe Nanocrystals Probed by Polarization-Dependent Two-Dimensional Photon Echo Spectroscopy. *J. Phys. Chem. A* **2011**, *115* (16), 3797–3806.
- (118) Harel, E.; Rupich, S. M.; Schaller, R. D.; Talapin, D. V.; Engel, G. S. Measurement of Electronic Splitting in PbS Quantum Dots by Two-Dimensional Nonlinear Spectroscopy. *Phys. Rev. B Condens. Matter* **2012**, *86* (7), 075412.
- (119) Tully, J. C. Perspective: Nonadiabatic Dynamics Theory. *J. Chem. Phys.* **2012**, *137* (22), 22A301.
- (120) Tully, J. C. Nonadiabatic Molecular Dynamics. *Int. J. Quantum Chem.* **1991**, *40* (S25), 299–309.
- (121) Jonas, D. M. Two-Dimensional Femtosecond Spectroscopy. *Annu. Rev. Phys. Chem.* **2003**, *54*, 425–463.
- (122) Brixner, T.; Mancal, T.; Stiopkin, I. V.; Fleming, G. R. Phase-Stabilized Two-Dimensional Electronic Spectroscopy. *J. Chem. Phys.* **2004**, *121* (9), 4221–4236.
- (123) Cho, M. Coherent Two-Dimensional Optical Spectroscopy. *Chem. Rev.* **2008**, *108* (4), 1331–1418.
- (124) Ginsberg, N. S.; Cheng, Y.-C.; Fleming, G. R. Two-Dimensional Electronic Spectroscopy of Molecular Aggregates. *Acc. Chem. Res.* **2009**, *42* (9), 1352–1363.
- (125) Cowan, M. L.; Ogilvie, J. P.; Miller, R. J. D. Two-Dimensional Spectroscopy Using Diffractive Optics Based Phased-Locked Photon Echoes. *Chem. Phys. Lett.* **2004**, *386* (1), 184–189.
- (126) Engel, G. S.; Calhoun, T. R.; Read, E. L.; Ahn, T.-K.; Mancal, T.; Cheng, Y.-C.; Blankenship, R. E.; Fleming, G. R. Evidence for Wavelike Energy Transfer through Quantum Coherence in Photosynthetic Systems. *Nature* **2007**, *446* (7137), 782–786.
- (127) Lee, H.; Cheng, Y.-C.; Fleming, G. R. Coherence Dynamics in Photosynthesis: Protein Protection of Excitonic Coherence. *Science* **2007**, *316* (5830), 1462–1465.

- (128) Collini, E.; Wong, C. Y.; Wilk, K. E.; Curmi, P. M. G.; Brumer, P.; Scholes, G. D. Coherently Wired Light-Harvesting in Photosynthetic Marine Algae at Ambient Temperature. *Nature* **2010**, *463* (7281), 644–647.
- (129) Roscioli, J. D.; Ghosh, S.; LaFountain, A. M.; Frank, H. A.; Beck, W. F. Quantum Coherent Excitation Energy Transfer by Carotenoids in Photosynthetic Light Harvesting. *J. Phys. Chem. Lett.* **2017**, *8* (20), 5141–5147.
- (130) Roscioli, J. D.; Ghosh, S.; LaFountain, A. M.; Frank, H. A.; Beck, W. F. Structural Tuning of Quantum Decoherence and Coherent Energy Transfer in Photosynthetic Light Harvesting. *J. Phys. Chem. Lett.* **2018**, *9* (17), 5071–5077.
- (131) Sil, S.; Tilluck, R. W.; Mohan T. M., N.; Leslie, C. H.; Rose, J. B.; Domínguez-Martín, M. A.; Lou, W.; Kerfeld, C. A.; Beck, W. F. Excitation Energy Transfer and Vibronic Coherence in Intact Phycobilisomes. *Nat. Chem.* **2022**, 1–9.
- (132) Seiler, H.; Palato, S.; Sonnichsen, C.; Baker, H.; Kambhampati, P. Seeing Multiexcitons through Sample Inhomogeneity: Band-Edge Biexciton Structure in CdSe Nanocrystals Revealed by Two-Dimensional Electronic Spectroscopy. *Nano Lett.* **2018**, *18* (5), 2999–3006.
- (133) Gallagher Faeder, S. M.; Jonas, D. M. Two-Dimensional Electronic Correlation and Relaxation Spectra: Theory and Model Calculations. *J. Phys. Chem. A* **1999**, *103* (49), 10489–10505.
- (134) Hybl, J. D.; Albrecht, A. W.; Gallagher Faeder, S. M.; Jonas, D. M. Two-Dimensional Electronic Spectroscopy. *Chem. Phys. Lett.* **1998**, *297* (3), 307–313.
- (135) Mukamel, S. *Principles of Nonlinear Optical Spectroscopy*; 1995.
- (136) Hamm, P.; Zanni, M. *Concepts and Methods of 2D Infrared Spectroscopy*; Cambridge University Press, 2011.
- (137) Wilkinson, G. R. R. J. H. Clark and R. E. Hester (Editors). *Advances in Infrared and Raman Spectroscopy*, Vol. 12. Wiley, New York. 1985. *J. Raman Spectrosc.* **1986**, *17* (6), 487–487.
- (138) Fragnito, H. L.; Bigot, J.-Y.; Becker, P. C.; Shank, C. V. Evolution of the Vibronic Absorption Spectrum in a Molecule Following Impulsive Excitation with a 6 fs Optical Pulse. *Chem. Phys. Lett.* **1989**, *160* (2), 101–104.
- (139) Dexheimer, S. L.; Wang, Q.; Peteanu, L. A.; Pollard, W. T.; Mathies, R. A.; Shank, C. V. Femtosecond Impulsive Excitation of Nonstationary Vibrational States in Bacteriorhodopsin. *Chem. Phys. Lett.* **1992**, *188* (1), 61–66.

- (140) Pollard, W. T.; Fragnito, H. L.; Bigot, J.-Y.; Shank, C. V.; Mathies, R. A. Quantum-Mechanical Theory for 6 Fs Dynamic Absorption Spectroscopy and Its Application to Nile Blue. *Chem. Phys. Lett.* **1990**, *168* (3), 239–245.
- (141) Ruhman, S.; Joly, A. G.; Nelson, K. A. Time-Resolved Observations of Coherent Molecular Vibrational Motion and the General Occurrence of Impulsive Stimulated Scattering. *J. Chem. Phys.* **1987**, *86* (11), 6563–6565.
- (142) Tian, P.; Keusters, D.; Suzuki, Y.; Warren, W. S. Femtosecond Phase-Coherent Two-Dimensional Spectroscopy. *Science* **2003**, *300* (5625), 1553–1555.
- (143) Ogilvie, J. P.; Kubarych, K. J. Chapter 5 Multidimensional Electronic and Vibrational Spectroscopy: An Ultrafast Probe of Molecular Relaxation and Reaction Dynamics. In *Advances In Atomic, Molecular, and Optical Physics*; Academic Press, 2009; Vol. 57, pp 249–321.
- (144) Butkus, V.; Zigmantas, D.; Valkunas, L.; Abramavicius, D. Vibrational vs. Electronic Coherences in 2D Spectrum of Molecular Systems. *Chem. Phys. Lett.* **2012**, *545*, 40–43.
- (145) Turner, D. B.; Wilk, K. E.; Curmi, P. M. G.; Scholes, G. D. Comparison of Electronic and Vibrational Coherence Measured by Two-Dimensional Electronic Spectroscopy. *J. Phys. Chem. Lett.* **2011**, *2* (15), 1904–1911.
- (146) Butkus, V.; Zigmantas, D.; Abramavicius, D.; Valkunas, L. Distinctive Character of Electronic and Vibrational Coherences in Disordered Molecular Aggregates. *Chem. Phys. Lett.* **2013**, *587*, 93–98.
- (147) Butkus, V.; Alster, J.; Bašinskaitė, E.; Augulis, R. N.; Neuhaus, P.; Valkunas, L.; Anderson, H. L.; Abramavicius, D.; Zigmantas, D. Discrimination of Diverse Coherences Allows Identification of Electronic Transitions of a Molecular Nanoring. *J. Phys. Chem. Lett.* **2017**, *8* (10), 2344–2349.
- (148) Chenu, A.; Christensson, N.; Kauffmann, H. F.; Mančal, T. Enhancement of Vibronic and Ground-State Vibrational Coherences in 2D Spectra of Photosynthetic Complexes. *Sci. Rep.* **2013**, *3*, 2029.
- (149) McHale, J. L. *Molecular Spectroscopy*, 2nd ed.; CRC Press, 2017.
- (150) Pollard, W. T.; Mathies, R. A. Analysis of Femtosecond Dynamic Absorption Spectra of Nonstationary States. *Annu. Rev. Phys. Chem.* **1992**, *43* (1), 497–523.
- (151) Cowan, M. L.; Bruner, B. D.; Huse, N.; Dwyer, J. R.; Chugh, B.; Nibbering, E. T. J.; Elsaesser, T.; Miller, R. J. D. Ultrafast Memory Loss and Energy Redistribution in the Hydrogen Bond Network of Liquid H₂O. *Nature* **2005**, *434* (7030), 199–202.

- (152) Ogilvie, J. P.; Armstrong, M.; Nagy, A.; Miller, R. J. D. Diffractive Optics-Based Heterodyne Detected Three-Pulse Photon Echo. In *The Thirteenth International Conference on Ultrafast Phenomena*; Optica Publishing Group: Washington, D.C., 2002. <https://doi.org/10.1364/up.2002.wd20>.
- (153) Shim, S.-H.; Zanni, M. T. How to Turn Your Pump-Probe Instrument into a Multidimensional Spectrometer: 2D IR and Vis Spectroscopies via Pulse Shaping. *Phys. Chem. Chem. Phys.* **2009**, *11* (5), 748–761.
- (154) Grumstrup, E. M.; Shim, S.-H.; Montgomery, M. A.; Damrauer, N. H.; Zanni, M. T. Facile Collection of Two-Dimensional Electronic Spectra Using Femtosecond Pulse-Shaping Technology. *Opt. Express* **2007**, *15* (25), 16681–16689.
- (155) Myers, J. A.; Lewis, K. L. M.; Tekavec, P. F.; Ogilvie, J. P. Two-Color Two-Dimensional Fourier Transform Electronic Spectroscopy with a Pulse-Shaper. *Opt. Express* **2008**, *16* (22), 17420–17428.
- (156) Lozovoy, V. V.; Pastirk, I.; Dantus, M. Multiphoton Intrapulse Interference. IV. Ultrashort Laser Pulse Spectral Phase Characterization and Compensation. *Opt. Lett.* **2004**, *29* (7), 775–777.
- (157) Augulis, R.; Zigmantas, D. Two-Dimensional Electronic Spectroscopy with Double Modulation Lock-in Detection: Enhancement of Sensitivity and Noise Resistance. *Opt. Express* **2011**, *19* (14), 13126–13133.
- (158) DeLong, K. W.; Trebino, R.; Hunter, J.; White, W. E. Frequency-Resolved Optical Gating with the Use of Second-Harmonic Generation. *J. Opt. Soc. Am. B, JOSAB*. <https://doi.org/10.1364/JOSAB.11.002206>.
- (159) van Stokkum, I. H. M.; Larsen, D. S.; van Grondelle, R. Global and Target Analysis of Time-Resolved Spectra. *Biochim. Biophys. Acta* **2004**, *1657* (2–3), 82–104.

Chapter 2: Broadband 2DES Detection of Vibrational Coherence in the S_x State of Ketocarotenoid Canthaxanthin

The nonadiabatic mechanism that mediates nonradiative decay of the bright S_2 state to the lower energy dark S_1 state of carotenoids involves population of an intermediate state, S_x , in several instances. The nature of S_x remains to be determined definitively, but it has been recently suggested that S_x corresponds to conformationally distorted molecules evolving along out-of-plane coordinates of the isoprenoid backbone near a low barrier between planar and distorted conformations on the S_2 potential surface. In this chapter, the electronic and vibrational dynamics accompanying the formation of S_x in toluene solutions of the ketocarotenoid canthaxanthin (CAN) are characterized with broadband two-dimensional electronic spectroscopy (2DES) with 7.8 fs excitation pulses and detection of the linear polarization components of the third-order nonlinear optical signal. A stimulated-emission cross peak in the 2DES spectrum accompanies the formation of S_x in < 20 fs following excitation of the main absorption band. S_x is prepared instantaneously, however, with excitation of hot-band transitions associated with distorted conformations of CAN's isoprenoid backbone in the low frequency onset of the main absorption band. Vibrational coherence oscillation maps and modulated anisotropy transients show that S_x undergoes displacements from the Franck–Condon S_2 state along out-of- plane coordinates as it passes to the S_1 state. The results are consistent with the conclusion that CAN's carbonyl-substituted β -ionone rings impart an intramolecular charge-transfer character that frictionally slows the passage from S_x to S_1 compared to carotenoids lacking carbonyl substitution. Despite the longer lifetime, the S_1 state of CAN is formed with retention of vibrational coherence after passing through a conical intersection seam with the S_x state.

The work presented in this chapter has been adapted from *J. Chem. Phys.* **2021**, *155*, 035103.

2.1 Introduction

The light-harvesting functions performed by carotenoids in photosynthetic organisms chiefly employ the lowest two excited singlet states, S_1 and S_2 , which are $\pi \rightarrow \pi^*$ excitations of a carotenoid's conjugated isoprenoid backbone.¹⁻⁴ The S_2 state can be prepared optically by transitions in the strong mid-visible absorption band; S_1 is considered a "dark" state, lacking electric-dipole allowed optical transitions to or from the ground state, S_0 .^{5,6} In condensed phases and in the binding sites of proteins, the S_2 state decays non-radiatively to the S_1 state usually in <200 fs after absorption of light. Owing to the extremely short timescale, the relaxation process is accompanied by only a few vibrations of the skeletal normal modes of the isoprenoid backbone. The decay to the S_1 state is accordingly very likely to be mediated by a nonadiabatic mechanism,^{7,8} involving strong coupling of electronic and vibrational motions.

Considerable evidence has accumulated, however, showing that the S_2 state does not directly decay to the S_1 state. An intermediate, usually labeled S_x , is detected in <20 fs after optical preparation of the S_2 state in several carotenoids.^{2,9,10} The structural and spectroscopic nature of S_x remains uncertain. The measured lifetime of S_x in unsubstituted carotenoids^{9,11} is consistent with the fluorescence lifetime usually stated for S_2 .² An assignment of S_x to the ${}^1B_u^-$ state^{12,13} was suggested early on by Zhang *et al.*¹⁴ and by Cerullo *et al.*,⁹ but this assignment would apply formally only to a planar carotenoid with C_{2h} symmetry. Ostroumov *et al.*¹⁵ assigned the X state they detected in two-dimensional electronic spectroscopy (2DES)¹⁶ studies of carotenoids in the LH2 light-harvesting protein

from purple bacteria to a direct excitation to the $^1B_u^-$ state. In their picture, the $^1B_u^-$ state borrows oscillator strength for absorption transitions from the nearby S_2 state via a Herzberg–Teller coupling;^{17,18} in the absence of symmetry breaking, the $^1B_u^-$ state would be expected to be a dark state.⁹

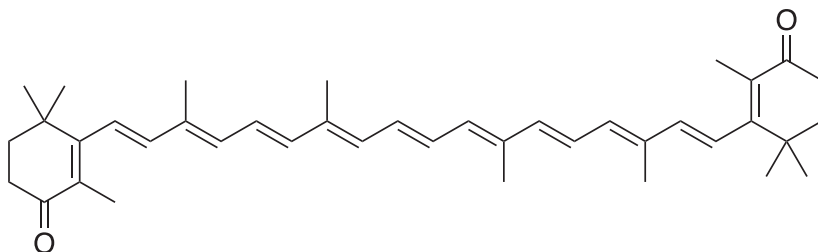


Figure 2.1. Structure of canthaxanthin.

Our finding that the lifetime of S_x is considerably longer in the carbonyl-substituted carotenoid peridinin, however, raises the possibility that S_x should be assigned instead to a conformationally distorted S_2 structure moving along out-of-plane coordinates of the isoprenoid backbone toward a conical intersection (CI) seam with the S_1 state.^{3,11,19,20} This general idea has found additional support from recent fluorescence studies. The S_x state is the likely origin of a broad fluorescence emission band in β -carotene solutions at cryogenic temperatures. The fluorescence anisotropy measured for β -carotene in aprotic solutions at room temperature indicates that the emission transition dipole moment (TDM) is rotated as much as 50° relative to that of the Franck–Condon S_2 state. These observations suggest that torsional and pyramidal distortions near the center of the isoprenoid backbone are initiated in S_x .⁶ In this article, we report that broadband 2DES can be used to detect the formation of the S_x state in toluene solutions of the ketocarotenoid canthaxanthin (CAN). The structure of CAN differs from that of β -carotene only by the addition of a carbonyl to

each of the β -ionone (cyclohexene) end rings (Figure 2.1). The carbonyls are thought to be essential to the role served by CAN as a light sensor in the orange carotenoid protein, which mediates photoprotective nonphotochemical quenching mechanisms in the phycobilisome in cyanobacteria.²¹ The 2DES spectra shown in this Chapter establish that S_x forms in <20 fs after optical preparation of the S_2 state of CAN by transitions in the main absorption band. Furthermore, it is shown that S_x is formed directly by vertical transitions of molecules in the ground-state ensemble that contribute to the broad low frequency onset of the main absorption band. Characterization of the high-frequency vibrational coherences in the 2DES spectrum establishes that S_x and S_1 are displaced structurally from the Franck-Condon S_2 state along out-of-plane modes of the isoprenoid backbone. Despite the presence of the carbonyl substituents, which substantially lengthen the lifetime of S_x to 440 fs, the results indicate that radiationless decay from S_x to S_1 occurs in CAN with retention of vibrational coherence.

2.2 Experimental Methods

2.2.1 Samples

CAN was used as received from Sigma-Aldrich (32993-2MG). In order to assess its purity, reversed-phase high-performance liquid chromatography (HPLC) of CAN solutions in acetonitrile was performed with a Waters Atlantis T3 5 μ m analytical column (4.6 \times 250 mm²) and detection with an Agilent Prostar 325 two-channel UV/vis detector at 480 and 364 nm. The chromatograms establish that >95% of the eluted sample corresponds to the all-trans configuration and that shorter carotenoids are not present. For femtosecond spectroscopy, samples of CAN were dissolved in toluene (Sigma-Aldrich 179418) to obtain an absorbance of 0.3 at 545 nm (18350 cm⁻¹) for a 1-mm path length static cuvette and

then centrifuged in a desktop microcentrifuge at 17 000g to pellet light-scattering particles. The CAN samples were kept in the dark prior to performing femtosecond spectroscopy experiments. The linear absorption spectrum was measured before and after exposure to the laser. Neither changes in the absorbance nor changes in the shape of the linear spectrum were observed after the samples were used in the recording of 2DES spectra, but a fresh sample was put in place after three iterations of the data acquisition process.

2.2.2 Linear Spectroscopy

Linear absorption spectra of CAN samples were recorded at room temperature (23 °C) with a Shimadzu UV-2600 spectrometer.

2.2.3 Two-Dimensional Electronic Spectroscopy

2DES spectra were recorded using a pump–probe optical configuration with adaptive pulse shaping²² to compress the laser pulses and to prepare the excitation pulse sequence (pulse 1– τ –pulse 2) required for the three-pulse stimulated photon-echo experiment.¹⁶ The instrumentation and methods were introduced in an earlier publication.²² Excitation pulses were obtained from a noncollinear optical parametric amplifier (NOPA, Spectra-Physics Spirit-NOPA-3H), which was pumped by the third harmonic of a 1.04 μm amplified Yb laser (Spectra-Physics Spirit-4W, 400 fs pulses at a 100 kHz repetition rate, 4 W average power). The pump and probe beams in the spectrometer were split from the NOPA output by a broadband dielectric beamsplitter (Layertec, Mellingen), processed by an adaptive pulse shaper (FemtoJock and FemtoJock P, respectively, Biophotonic Solutions), and then compressed by multiple reflections on pairs of broadband chirped mirrors (Ultrafast Innovations, Munich). For the present experiments, the NOPA's signal beam output spectrum (Figure 2.2) was centered at 590 nm (~ 55 nm FWHM; 520–700 nm usable

range). The excitation pulse energy was attenuated to 4.5 nJ per pulse, as measured at the sample's position. The pump beam's plane of linear polarization was rotated 45° from that of the probe beam by a thin achromatic half-wave retarder plate. The two beams were focused by off-axis parabolic mirrors to 100 μm spots overlapped spatially just after the front window of the sample cuvette. The excitation pulses in both beams were characterized by MIIPS scans²³ conducted with a thin β-barium borate crystal, which was placed at the sample's position following a single cuvette window. The estimated pulse duration for both beams at the sample position was 7.8 fs. Residual phase plots (Figures A2.1 and A2.2), and SHG-FROG spectrograms²⁴ (Figure A2.3) are presented in the appendix.

2DES spectra were recorded by programming the pump beam's pulse shaper to scan the coherence time interval between the two pump pulses, τ , from 0 to 50 fs with 0.5 fs steps to obtain the excitation axis after Fourier transformation. Longer τ scans produced identical spectra but with a lower signal/noise ratio. The detection axis of the 2DES spectrum was measured directly by measuring the pump-induced change in probe transmission through the sample with a home-built 0.2 m spectrograph (300 gr/mm diffraction grating) and a fast CCD detector (Andor Newton 940) using a phase-sensitive detection protocol and amplitude modulation of the pump pulses.²⁵ The waiting time interval between the second pump pulse and the probe pulse, T , was scanned by a time-of-flight delay line from 0 to 20 fs with a 2.5 fs spacing; the 25 to 500 fs range was then sampled at 5 fs intervals. An additional dataset, with scans reaching out to $T = 20,000$ fs, was used to measure the lifetime of the S_1 state. Each reported 2DES spectrum was determined as the average of the spectra from six successive T scans. Owing to the use of the pump-probe optical geometry and amplitude modulation of the pump-pulse pair, the

2DES spectra reported here are intrinsically autophased. The spectra obtained using this approach are the sum of those from the rephasing and non-rephasing nonlinear optical pathways.²²

Linear polarization components of the 2DES signal were measured by analyzing the transmitted probe beam after collimation and prior to the input of the spectrograph with a calcite Glan-laser polarizer. The polarizer was rotated by a motorized stage in successive T scans to select the parallel and perpendicular signal components, A_{\parallel} and A_{\perp} , respectively, relative to the pump beam's plane of linear polarization. A dichroism-free total-amplitude signal, K , is obtained from the two components as

$$K = A_{\parallel} + 2A_{\perp} \quad (2.1)$$

where K is proportional to the excited-state population prepared by the pump pulses.²⁶

The anisotropy,

$$r = \frac{A_{\parallel} - A_{\perp}}{A_{\parallel} + 2A_{\perp}} \quad (2.2)$$

measures the depolarization resulting from changes in the orientation of the excited-state TDM by internal motions or by global rotations of the entire molecular framework. In some cases, the anisotropy signal includes contributions from electronic coherence of degenerate excited states.²⁷⁻²⁹ Because the pump-probe spectra of carotenoids exhibit zero crossings when ground-state bleaching (GSB) or stimulated emission (SE) bands overlap with excited-state absorption (ESA) bands, r is useful only where the total amplitude $K \neq 0$.

2.3 Results

2.3.1 Linear Spectroscopy

Figure 2.2 shows the linear absorption spectrum of CAN in toluene solvent at room temperature (23 °C). The spectrum is plotted as the oscillator strength, $\epsilon(\nu)/\nu$, which is obtained from the absorption spectrum, $\epsilon(\nu)$, and the wavenumber ν (cm^{-1}). The spectrum

of the excitation pulses used in the 2DES experiment is plotted superimposed. The oscillator-strength spectrum of CAN is smooth and unstructured; in comparison, the absorption spectrum of β -carotene exhibits a partially resolved vibronic progression with respect to the C=C and C-C stretching modes of the isoprenoid backbone. Numerical simulations performed previously with the multimode Brownian oscillator model^{11,30} indicate that the carbonyl substituents on the β -ionone end rings (Figure 2.1) broaden the spectrum by increasing the system-bath coupling (or solvation reorganization energy), λ .

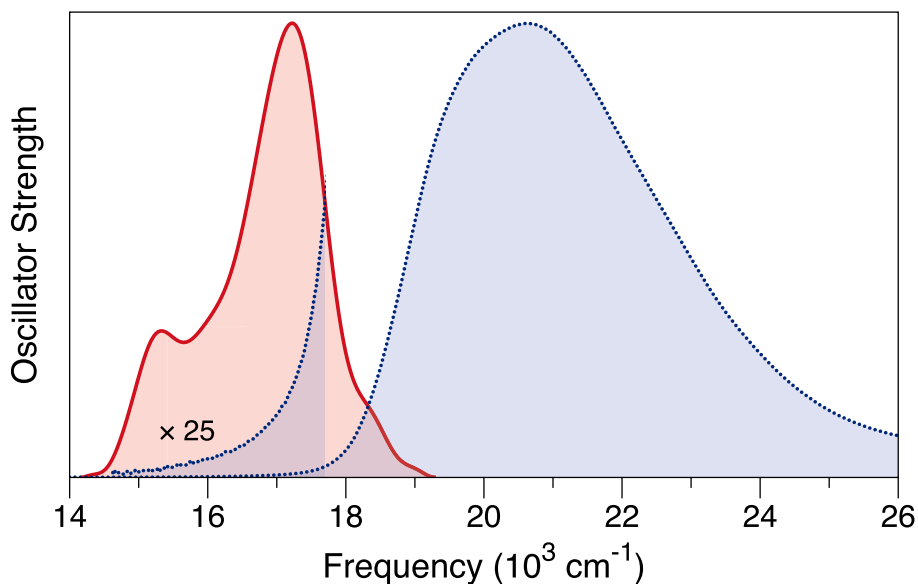


Figure 2.2. Linear absorption spectrum of CAN in toluene solvent (blue dotted curve), plotted with respect to the wavenumber ν as the relative oscillator strength, $\epsilon(\nu)/\nu$. The 14000–17000- cm^{-1} range of the spectrum is also plotted with a $\times 25$ scaling of the ordinate. The laser intensity spectrum from the broadband excitation pulses used in the 2DES experiments (red solid curve) is superimposed.

The carbonyl substituents accentuate an additional feature in the absorption spectrum of ketocarotenoids over the 14000–18000 cm^{-1} range, a broad “tail” in the low frequency onset of the main absorption band. This region of the linear absorption spectrum has been

assigned to vertical transitions to the ${}^1B_u^-$ state¹⁵ or to hot-band transitions of thermally excited molecules with distorted conformations of the isoprenoid backbone.³¹

2.3.2 2DES Spectra

Figure 2.3 presents 2DES K spectra acquired at several T delays selected from the 0-500 fs dataset from CAN in toluene. The NOPA spectrum used in these experiments spans the red tail and includes a portion of the main absorption band (Figure 2.2), which allows both regions to be characterized in parallel in the same 2DES experiment. A comparable laser tuning was used previously in the broadband 2DES study by Ostroumov et al.¹⁵ of carotenoids in the LH2 protein from purple bacteria. Sugisaki et al.¹⁰ used tunable 20 fs pulses to excite corresponding regions of the absorption spectrum of β -carotene in separate transient grating experiments. The CAN concentration was adjusted for the 2DES experiments to obtain an optical density of 0.3 at 18350 cm^{-1} , approximately where the normalized laser and absorption spectra cross. These conditions are optimal for excitation of molecules in the main absorption band. The 2DES spectra presented in Figure 2.3 are normalized by the laser intensity spectrum along both axes.

The 2DES K spectra exhibit distinct responses along the excitation axis in the red tail and main absorption band regions. At short delays T , a diagonal band of positive-going signal derived from GSB and SE from the S_2 state is superimposed on a broader band of negative-going ESA transitions to a manifold of higher energy singlet states, S_n . The positive band oscillates parallel to the diagonal of the spectrum over the $T = 0\text{-}50$ fs range, with a recurrence back to the diagonal observed at $T = 35$ fs, which indicates directly that the spectrum is strongly modulated by vibrational coherences. Scanning frame-by-frame through the entire dataset reveals strong amplitude oscillations over most of the spectrum.

However, as T advances, a resolved SE cross peak spanning from the 17500 cm^{-1} region to the lower frequency limit of the detection axis develops in the main band excitation region

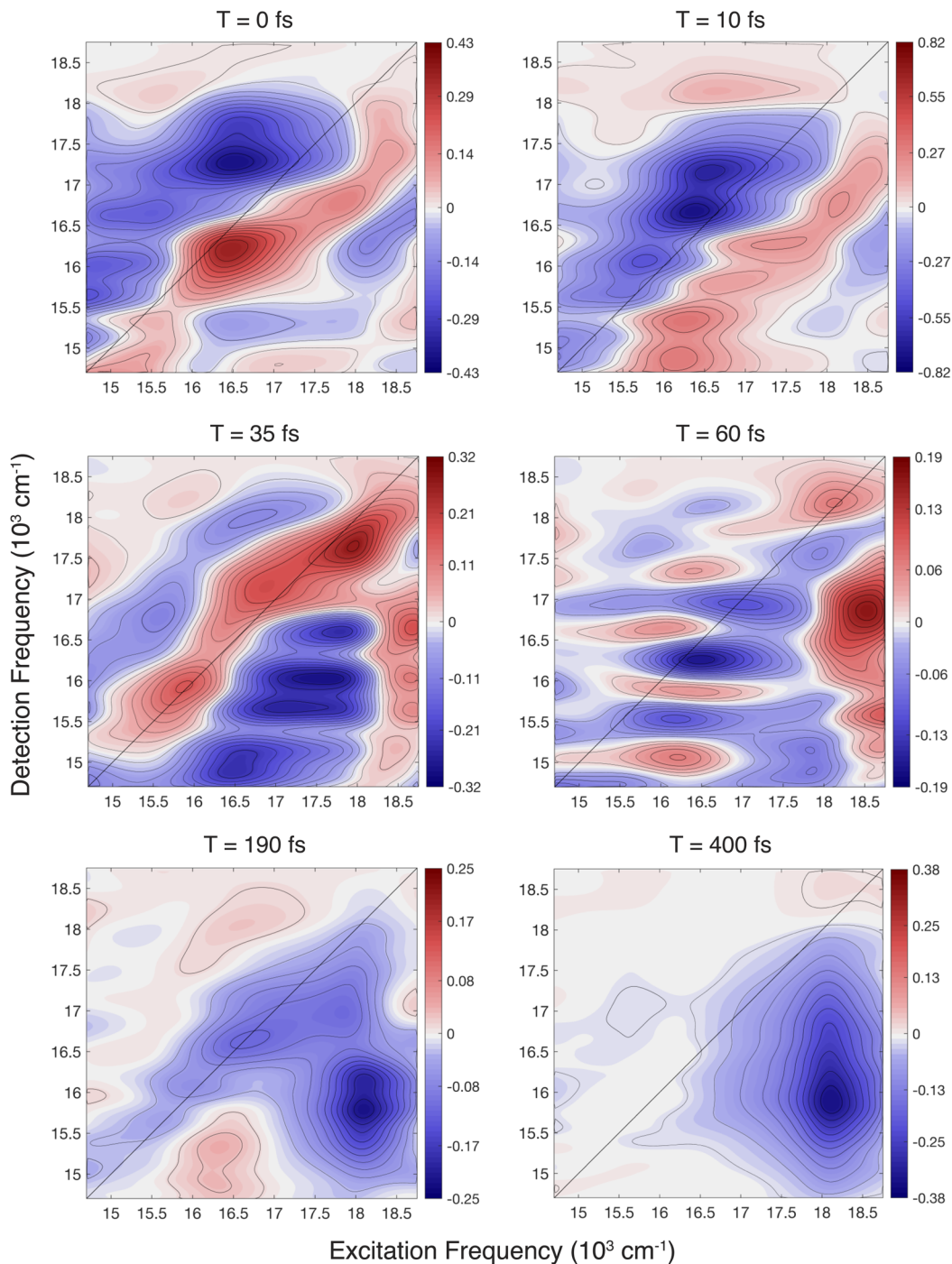


Figure 2.3. Evolution of total amplitude (K) 2DES spectra from CAN in toluene at six waiting times T .

from $T > 20$ fs onward and disappears at $T > 100$ fs. The $T = 0$ and $T = 10$ -fs spectra show that a comparable region of SE can be observed in the red tail region at shorter delays T than in the main band. At longer delays, the red tail region exhibits a series of alternating SE and ESA regions spaced by ~ 500 cm^{-1} , which is consistent with interference of the SE and ESA transitions due to vibronic progressions of modes of the isoprenoid backbone, as discussed in the following. Finally, relatively strong regions of ESA characteristic of the S_1 state develop below the diagonal at $T > 150$ fs in both excitation regions. The ESA spectrum observed at $T = 400$ fs dominates the entire spectrum from the main excitation band well into the red tail, and it persists throughout as the S_1 state decays to S_0 over the $T = 1$ –10-ps range.

2.3.3 Global and Target Modeling of the 2DES spectra

The time evolution of the non-oscillatory population signals in the 2DES K spectra during the nonradiative relaxation from S_2 to S_1 can be approximately described by global and target modeling.³² This approach fits the 2DES spectra using a linear combination of evolution-associated difference spectra (EADS) for each of the spectrokinetic species in a kinetic model, here describing the nonradiative decay pathway between the singlet excited states of CAN. The kinetic scheme used in these global models defines a population compartment labeled S_x that serves as an intermediate between the S_2 state prepared by the excitation pulses and the S_1 state. The EADS are weighted in the global model by the waiting time T dependence of the populations for the spectrokinetic species. The main band and red tail regions of the excitation axis were modeled separately. Figure 2.4 shows the two-dimensional (2D) global model for the main absorption band region from 17700 to 18750 cm^{-1} . The EADS from the S_2 state contains alternating ESA and GSB/SE features

parallel to the diagonal of the spectrum spaced by $\sim 1200 \text{ cm}^{-1}$, which indicates a vibronic progression principally due to displacements of the ground state S_0 , the resonant S_2 state, and a higher singlet excited state S_n with respect to the C–C and C=C stretching modes of the isoprenoid backbone of CAN. The vibronic structure is partially resolved at short T delays compared to the electronic dephasing time owing to partial relief of the inhomogeneous broadening evident in the linear absorption spectrum. (The global model is convoluted with a 12-fs Gaussian-shaped instrument-response function centered at $T = 0 \text{ fs}$.)

The instantaneous compartment from the S_2 state decays very rapidly in the global model, in $13.6 \pm 1.2 \text{ fs}$, to yield the S_x intermediate. This time constant is comparable to those determined previously for β -carotene¹¹ and for peridinin¹⁹ in heterodyne transient grating experiments. The rise of S_x is temporally and spectrally well-resolved from the S_2 compartment in terms of the delayed formation of its off-diagonal cross peak, which consists of a broad band of net SE character spanning most of the detection axis. The EADS from S_x also incorporates a GSB signal along the diagonal of the spectrum, which is initially obscured by the diagonal ESA band from the S_2 state. This finding confirms that S_2 and S_x share the same electronic ground state. The S_x compartment decays in $440 \pm 10 \text{ fs}$ to S_1 , which is associated with a broad band of ESA centered at 16000 cm^{-1} . As determined with a second dataset with a longer T axis reaching out to 20 ps, the lifetime of S_1 for excitations in the main band is $4.1 \pm 0.2 \text{ ps}$. This value is consistent with that determined previously in 1D pump–probe experiments with excitation nearer to the absorption maximum.³³ Owing to the short time axis for the $T = 0\text{-}500 \text{ fs}$ dataset of the global model, we did not include a

compartment for the S_0^* state, a long-lived (ps lifetime) ground-state intermediate that has been often observed following radiationless decay from the S_1 state in carotenoids.²

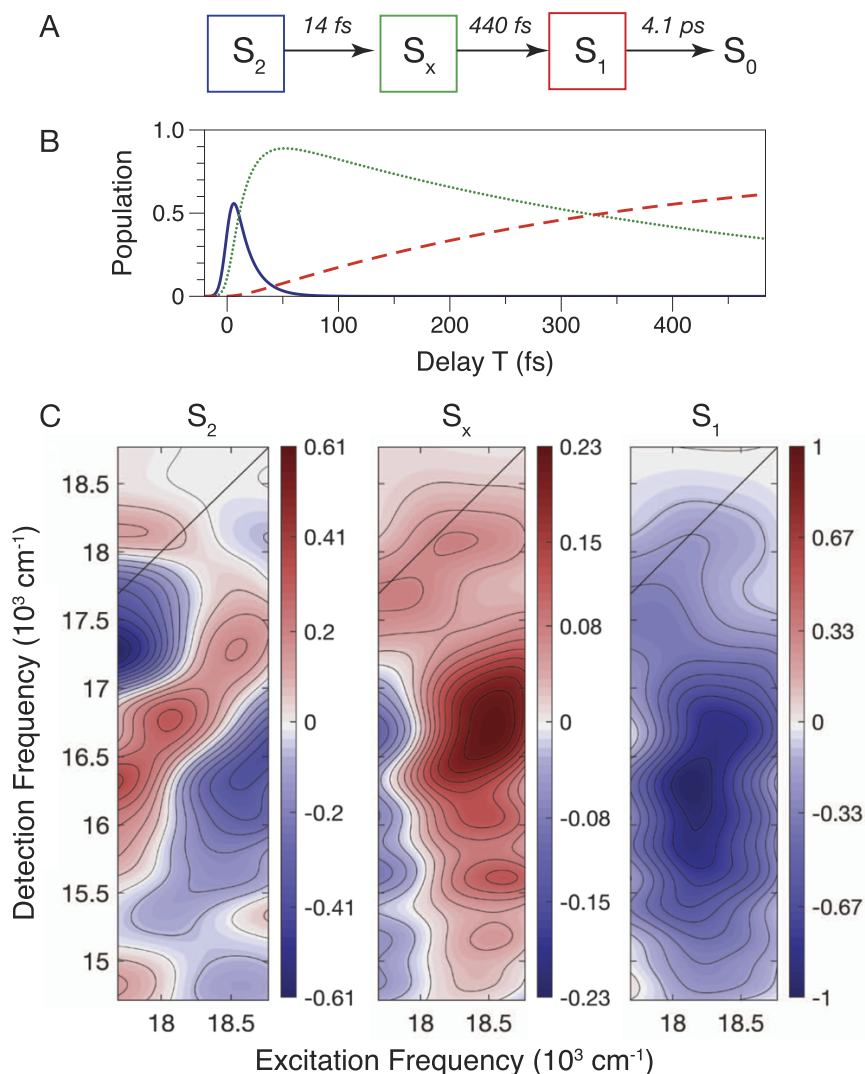


Figure 2.4. 2D global and target model for the main band excitation region of the 2DES K spectra from CAN in toluene. (a) Kinetic scheme and time constants for nonradiative decay of the S_2 state via an intermediate, S_x , to the S_1 state. (b) Time dependence of the populations for the S_2 (blue), S_x (green dotted), and S_1 (red dashed) spectrokinetic species. (c) 2D evolution-associated difference spectra (EADS) for the three spectrokinetic species. The EADS are scaled relative to the maximum of the ESA signal in the S_1 compartment.

Slices of the 2DES spectra at specific excitation wavenumbers in the main absorption band were modeled separately in a series of one-dimensional (1D) global models to probe the dependence of the response as the excitation is tuned toward the red tail region and to allow comparison of the fitted set of EADS with the line shapes determined in earlier experiments with ~ 100 -fs excitation pulses. Figure A2.4 in the supplementary material presents the 1D model for excitation at 18500 cm^{-1} . The EADS for S_x in this model is broader and substantially red-shifted of that determined for the S_2 state of β -carotene by de Weerd et al.³⁴ with pump-probe spectroscopy and from the time-resolved fluorescence upconversion spectrum reported by Macpherson and Gillbro.³⁵ As the excitation frequency is scanned over the main band region toward the red tail of the absorption spectrum, the lifetime of the S_2 state shortens markedly, but the lifetime of the S_x state remains mostly constant. The global model determined for the $16700\text{--}17700\text{ cm}^{-1}$ part of the red tail region of the excitation axis of the 2DES spectrum of CAN is reported in Figure 2.5. This model indicates that the S_x state is the first state in the kinetic scheme for this region of the absorption spectrum with an appreciable lifetime.

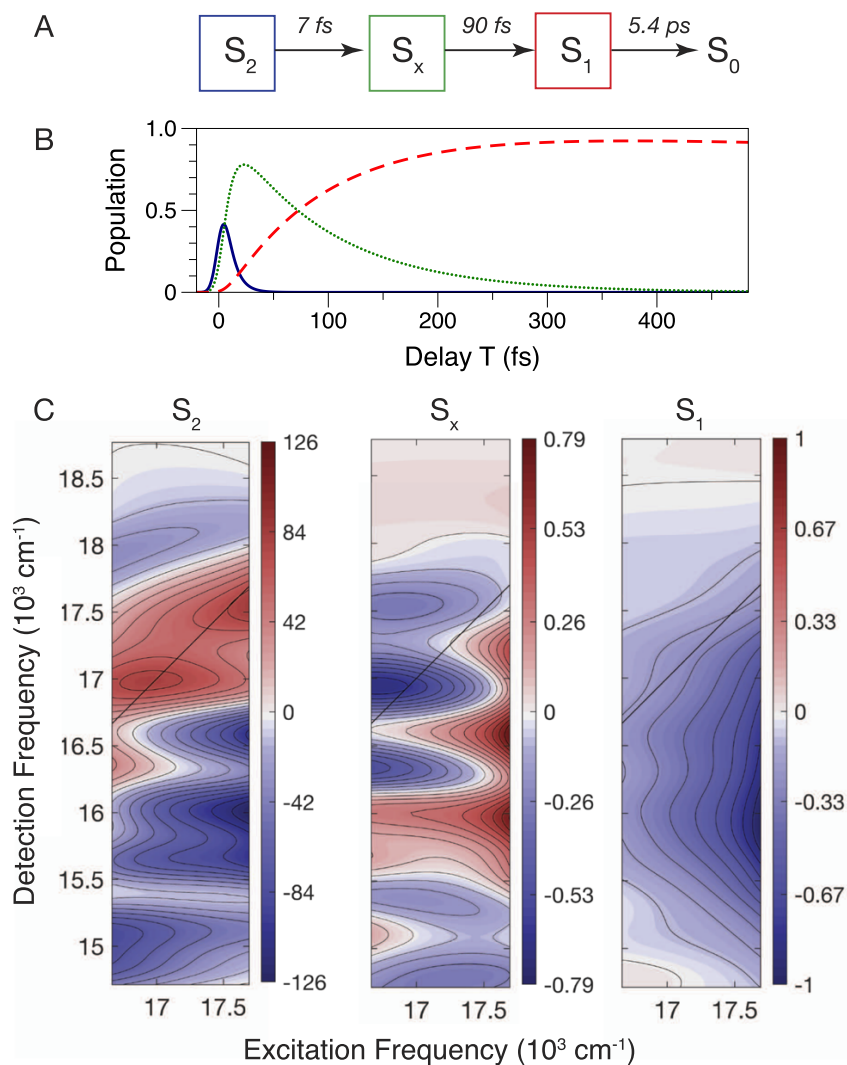


Figure 2.5. 2D global and target model for the red tail excitation region of the 2DES *K* spectra from CAN in toluene. (a) Kinetic scheme and time constants for nonradiative decay of the S_2 state via an intermediate, S_x , to the S_1 state. (b) Time dependence of the populations for the S_2 (blue), S_x (green dotted), and S_1 (red dashed) spectrokinetic species. (c) 2D evolution-associated difference spectra (EADS) for the three spectrokinetic species. The EADS are scaled relative to the maximum of the ESA signal in the S_1 compartment in the main band region (Figure 2.4).

The instantaneous S_2 compartment in this model can be mainly attributed to a nonresonant response, given its amplitude compared to the subsequent population-dependent compartments and its very short lifetime, 7.3 ± 0.7 fs, which is shorter than the 12-fs instrument-response width estimated in these experiments. The S_x compartment exhibits a significantly shorter lifetime, 90 ± 10 fs, than the 440-fs lifetime for S_x in the main absorption band, but it persists long enough to make it clear that it is due to excited-state population produced by resonant excitation of molecules absorbing in the red tail. The EADS for the S_x intermediate here includes overlapping net ESA and net SE bands displaced well below the diagonal of the spectrum, but as noted above, a fast moving off-diagonal SE band can be observed in this excitation region at short delays in the 2DES spectra. The S_1 species that is produced upon decay of S_x shares the off-diagonal spectral profile of the S_1 state in the main absorption band, but its amplitude decreases as the absorption oscillator strength decays toward lower frequencies along the excitation axis. These findings strongly suggest that excitations of CAN in the red tail region of the ground state absorption spectrum promptly prepare a structure analogous to that of S_x in the main band, but its decay to S_1 is considerably more rapid; however, the lifetime of S_1 determined in the global model for the red tail excitation region, 5.4 ± 0.3 ps, is somewhat longer than that obtained for S_1 in the main band. The different lifetimes determined for S_x and S_1 in the red tail suggest that the structures for these states are somewhat different from those obtained with excitation in the main absorption band.

2.3.4 Vibrational Coherence

The 2DES spectrum from CAN is strongly modulated by vibrational coherences associated with modes of the isoprenoid backbone. Analysis of the overlapping

contributions from excited state and ground state coherences is aided by the oscillation maps provided in Figure 2.6, each of which shows the Fourier amplitude at a selected frequency ωT as a function of the $(\omega_{ex}, \omega_{det})$ coordinates in the 2DES spectrum. These frequencies were selected from the principal components observed in the Fourier amplitude spectra determined at several coordinates sampled from the 2DES spectra in the region of the S_x cross peak; Figure 2.7 and 2.8 include examples of the K transients and the corresponding Fourier amplitude spectra observed near the cross peak from S_x . Additional maps, at 100 cm^{-1} (Figure A2.5) and 1800 cm^{-1} (Figure A2.6), are included in the supplementary material. The maps were generated by Fourier transformation with respect to the waiting time T after subtracting the nonoscillating population signal fit by an overdetermined global model. The residual transients were zero padded to interpolate the frequency axis, but the intrinsic resolution, 77 cm^{-1} , is determined by the sampled T range from 70 to 500 fs. The $T < 70$ fs range was discarded to avoid contamination from oscillatory signals at short delays T , including those associated with temporal overlap of the second and third excitation pulses and those from instantaneous nonresonant responses in the red tail region.

The $\omega_1 = 1520 \text{ cm}^{-1}$ mode is assigned to C=C in-plane stretching vibrations of the isoprenoid backbone of a carotenoid. (The numbering adopted here is as commonly used in the literature on resonance Raman spectroscopy of carotenoids, as reviewed by Robert et al.^{36,37}) For the excitation region corresponding to the main absorption band, the most intense peak in the oscillation map for the ω_1 mode is observed near to the diagonal of the spectrum. Two additional peaks are observed below the diagonal at intervals nearly matching the mode frequency. The spacing of the peaks is consistent with the intensity

pattern anticipated for a displaced pair of harmonic oscillator potentials, as modeled by Butkus et al.³⁸ and by Egorova,³⁹ with the additional provision that the patterns for the rephasing and nonrephasing nonlinear optical pathways are superimposed here. Peaks would be expected in a similar progression spaced by ω_1 above the diagonal of the oscillation map, but the pattern is truncated in the high-frequency corner of the 2DES spectrum by the tuning of the laser spectrum.

In the red tail region of the excitation axis, peaks are also observed in the ω_1 oscillation map above and below the diagonal in partially resolved sum and difference combinations,^{18,40} which arise from mixing with the other principal modes of the isoprenoid backbone. The distinct $\sim 500\text{ cm}^{-1}$ spacing likely corresponds to combinations of ω_1 with the $\omega_3 = 1005\text{ cm}^{-1}$ and/or $\omega_4 = 960\text{ cm}^{-1}$ modes. Combination bands are also observed in the red tail region of the oscillation maps at other mode frequencies. This finding is consistent with the proposal that the photoselected molecules in the red tail region assume a distribution of non-planar conformations³¹ because the vibrational modes of distorted conformations of the isoprenoid backbone would be more strongly mixed than those for planar all-trans configurations. A partially resolved node between the main band and red tail excitation regions of the oscillation map can be explained by interference of the signals in the two regions, which would be expected due to the shift of phase that accompanies detuning from the center of a spectral band.^{38,41} Note also that the toluene solvent contributes a nonresonant background at several vibrational frequencies close to those of CAN, increasingly as the inner-filter attenuation of the laser intensity by the CAN solute molecules decreases, but the restriction of the peak patterns along the excitation axis as observed here indicates predominantly resonant excitations. Furthermore, linear

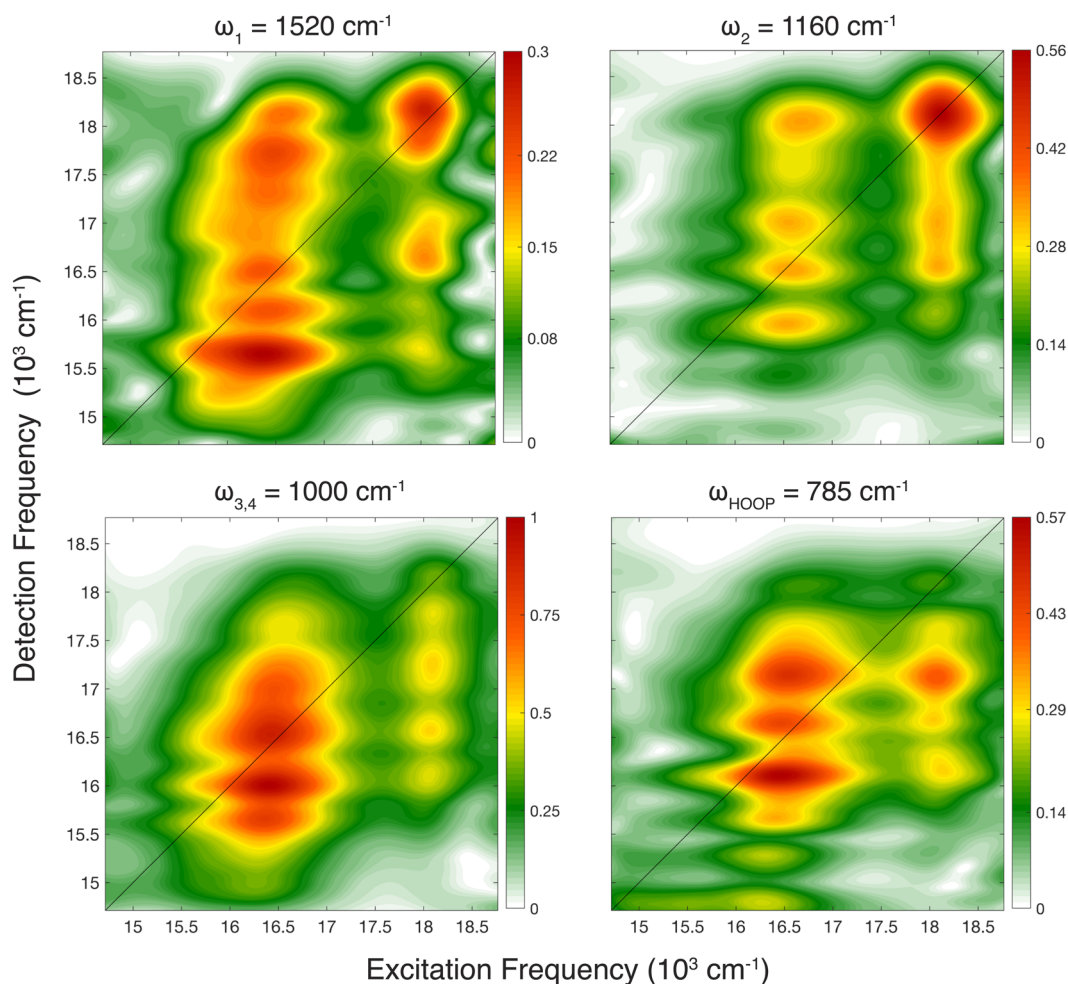


Figure 2.6. Oscillation maps for the principal vibrational coherences detected in the 2DES K spectra from CAN in toluene.

prediction singular-value decomposition models of modulated transients at key coordinates of the 2DES spectrum (not shown) indicate that the damping times for the modulation components are typically < 400 fs, which is similar to the lifetime of S_x in the main band region, whereas the vibrational dephasing time for toluene vibrations in the liquid is 5 ps.⁴²

The oscillation map observed for the $\omega_2 = 1160$ cm^{-1} mode is analogous to that of ω_1 , but some interesting differences are observed in the intensity patterns. The ω_2 mode arises from C–C stretching vibrations coupled to in-plane C–H bending motions near the center of

the isoprenoid backbone.⁴³ In the main band excitation region, the peaks below the diagonal of the spectrum are not as well resolved as in the ω_1 map, perhaps due to differences in excited-state and ground-state mode frequencies for the overlapping SE and GSB peaks, respectively. Furthermore, unlike the oscillation maps for the other modes, the peaks observed for ω_2 in the red tail excitation region are weaker than the diagonal peak observed in the main band. This observation is consistent with the idea that the red tail region includes molecules with out-of-plane distortions. The normal coordinate analysis of β -carotene discussed by Koyama et al.⁴³ indicates that the resonance Raman intensity of the ω_2 mode is weaker in cis configurations compared to all-trans configurations.

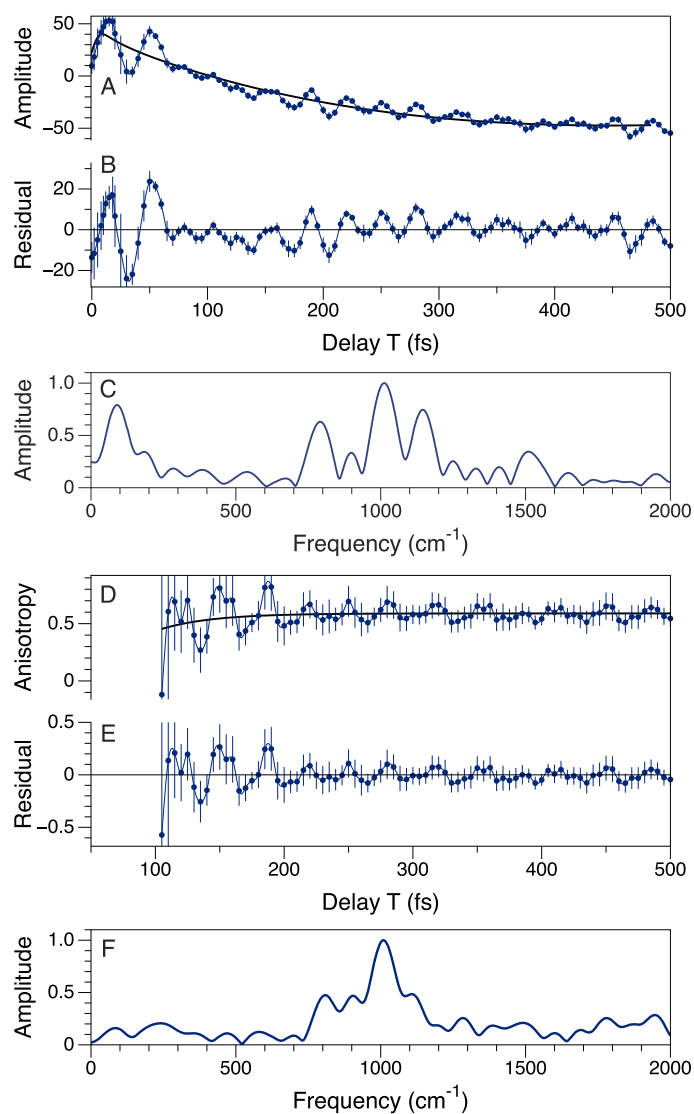


Figure 2.7. Total amplitude K and anisotropy r transients with excitation at 18200 cm^{-1} and detection at 16750 cm^{-1} in the S_x cross peak in the main band excitation region. (a) K transient, with the fit from the global model (from Figure 2.4) superimposed. (b) Residual (K -global model) transient. (c) Fourier transform amplitude spectrum of the K residual over the $T = 70$ - 500 fs range. (d) Anisotropy r transient, with a fitted exponential (40 fs time constant). (e) Residual (r -exponential fit) transient. (f) Fourier transform amplitude spectrum of the r residual over the $T = 100$ - 500 fs range. Error bars show the 95% confidence intervals for the K and r amplitudes.

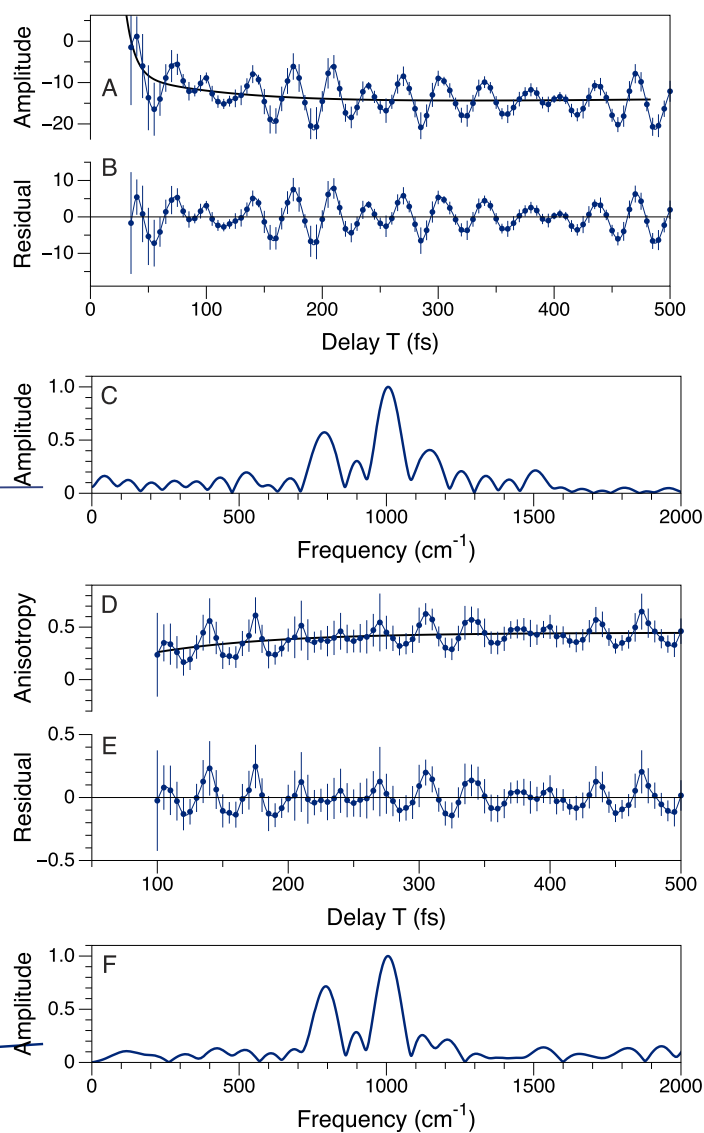


Figure 2.8. Total amplitude K and anisotropy r transients with excitation at 17200 cm^{-1} and detection at 16750 cm^{-1} in the S_x cross peak in the red tail excitation region. (a) K transient, with the fit from the global model (Figure 2.5) superimposed. (b) Residual (K -global model) transient. (c) Fourier transform amplitude spectrum of the K residual over the $T = 70$ - 500 fs range. (d) Anisotropy r transient, with a fitted exponential (92 fs time constant). (e) Residual (r -exponential fit) transient. (f) Fourier transform amplitude spectrum of the r residual over the $T = 100$ - 500 fs range. Error bars show the 95% confidence intervals for the K and r amplitudes.

The oscillation map shown in Figure 2.6 for 1000 cm^{-1} displays unresolved contributions in the spectra from two modes, ω_3 and ω_4 . The $\omega_3 = 1005\text{ cm}^{-1}$ mode is assigned to in-plane rocking motions of methyl groups near the center of the isoprenoid backbone, whereas the $\omega_4 = 960\text{ cm}^{-1}$ mode is assigned to hydrogen-out-of-plane (HOOP) motions coupled to torsions of the C=C bonds. This mode is usually quite weak in the resonance Raman spectrum of all-trans carotenoids.⁴³⁻⁴⁵ A similar pattern in the oscillation map is observed for the local HOOP vibration at $\omega_{HOOP} = 785\text{ cm}^{-1}$ in the red tail and main band excitation regions. This mode was also detected by Liebel et al.^{46,47} in impulsive pump–continuum probe experiments with β -carotene. That this vibration is prominent in the 2DES spectrum from CAN is a strong indication that S_x and/or S_1 undergo out-of-plane distortions that weaken the conjugation near the center of the isoprenoid backbone.

The displacement well below the diagonal of the oscillation map of the strongest peaks for the ω_3 and/or ω_4 and the ω_{HOOP} modes resolves the patterns due to excited-state vibrational coherences³⁹ in S_x and/or S_1 from the overlapping ground-state vibrational coherences from S_2 . The T range employed for the Fourier transformation principally monitors the S_x compartment, but it also includes the rise of the S_1 compartment, especially in the red tail. The short lifetime of S_2 limits its contributions over the sampled T range to stimulated Raman (ground-state) coherences, which is consistent with the strongest peaks in the oscillation maps from ω_1 and ω_2 being on the diagonal of the 2DES spectrum.

2.3.5 Anisotropy

The general conclusion from the oscillation maps discussed above is that S_x and perhaps S_1 exhibit vibrational coherences in out-of-plane modes of the isoprenoid backbone of CAN, and the pattern of amplitudes is different from those observed in

resonance Raman spectra. These points can be further considered by examining anisotropy transients sampled below the diagonal of the 2DES spectrum in regions associated with S_x in the global models. In the simplest picture, the anisotropy provides information on the orientation of the TDM relative to the photoselected direction for the optically prepared S_2 state. Figures 2.7 and 2.8 compare the K and r transients sampled in the main band and red tail excitation regions, respectively, near the maximum amplitude of the S_x EADS. The r transients are limited to $T > 100$ fs to avoid the zero-crossing by K in the main band. (Additional K transients sampled on the diagonal for S_2 and off-diagonal for the S_1 EADS are included in the supplementary material as Figs. A2.7–A10.)

In the main band excitation region, the r transient [Figure 2.7(d)] exhibits oscillations yielding a simplified Fourier amplitude spectrum [Figure 2.7(f)], with the in-plane ω_1 and ω_2 components significantly attenuated compared to their counterparts in the spectrum [Figure 2.7(c)] from the K transient [Figure 2.7(a)]. The amplitude oscillations in K can be described as an interference pattern, with repeating partial cancellation and recurrence regions along the T axis arising mainly from the superpositions of the oscillations from the ~ 1000 and 1160 cm^{-1} modes with those from the more resolved 1520 cm^{-1} mode. Modes with out-of-plane character are clearly more prominent in the r spectrum, and ω_4 apparently contributes a partially resolved peak in the $\sim 950\text{ cm}^{-1}$ region next to the peak for ω_3 . In comparison, the Fourier amplitude spectra of K [Figure 2.8(c)] and r [Figure 2.8(f)] are more similar with excitation in the red tail, and the 785 cm^{-1} component is stronger than in the main band. The out-of-plane modes would be expected to modulate the direction of the excited-state TDM of a carotenoid, so their appearance in the r transients should be expected if S_x is displaced along those coordinates from the Franck–

Condon geometry. Note that if a twisted or pyramidal distortion near the center of the isoprenoid backbone occurs, even the ω_3 wagging mode would likely cause the direction of the TDM to wobble, and it appears prominently in the r spectrum in both excitation regions. Of course, a normal coordinate analysis for an all-trans configuration of a carotenoid can only be used in a limited way here to infer the character of motion, especially if an out-of-plane distortion results in mixing of the modes of the isoprenoid backbone as suggested by the oscillation maps. In contrast, the ω_1 and ω_2 modes are mainly modulations of the bond lengths along the direction of the isoprenoid backbone; these modes would not be expected to modulate the TDM direction as strongly.

The r transients shown in Figures 2.7 and 2.8 also indicate exponentially rising trends with shorter time constants than those for the decay of S_x . The initially lower average r values observed at $T = 100$ fs are consistent with the suggestion that the isoprenoid backbone of CAN undergoes an out-of-plane displacement shortly after optical preparation of the S_2 state. The fluorescence anisotropy from CAN in toluene exhibits a value of 0.30 with excitation in the main band region used here (results not shown), which corresponds to an average value for the internal rotation of the excited-state TDM of $\sim 25^\circ$ relative to that of the photoselected Franck–Condon S_2 state.⁶ The rising r trend observed subsequently is in general agreement with the previous proposal by de Weerd et al.³⁴ in the case of β -carotene that the isoprenoid backbone relaxes toward a planar conformation in S_1 after undergoing twisting deformations in the S_2 state, but their picture would expect a slower response accompanying vibrational cooling in S_1 after nonradiative decay from S_x . An additional issue to consider, however, is raised by the work of Jonas and co-workers,^{48,49} who have pointed out that the pump–probe anisotropy carries distinct information content

from that of the fluorescence anisotropy when ESA signals are present owing to the involvement of a second higher-energy excited electronic state in the third-order nonlinear optical response. In the present case, the strength of the ESA contributions to the signal at the S_x cross peak increases with respect to T as population is transferred between S_x and S_1 . The S_n states involved in the ESA transitions in carotenoids are likely to exhibit TDMs oriented more or less along the direction of the isoprenoid backbone,^{6,50} but they would not necessarily be perfectly aligned with that of the resonant S_2 state because the TDMs of the singlet states of the carotenoids are calculated to be displaced by a few degrees relative to the molecular framework.⁶ This displacement introduces a possible electronic state dependence for the orientation of the photoselected TDMs contributing to the nonlinear optical signal during the nonradiative decay process. This issue might account for the observation that an $r > 0.4$ value is reached at the end of the recordings, especially in Figure 2.7 for the main band region.

In sum, these findings indicate that while the oscillations in the anisotropy are potentially useful for determining the character of motion in the vibrational coherence in the S_x state, the relaxation response from the anisotropy is complicated owing to the superposition of the trajectory taken in the S_2 and S_x states with its projection onto the higher S_n potential surfaces for the ESA transitions. As already discussed for the case of β -carotene, we anticipate that a direct use of information from fluorescence anisotropy measurements will allow a more detailed discussion about the TDM direction taken by CAN upon optical excitation to the S_2 state.

2.4 Discussion

The broadband 2DES studies of CAN in toluene solution presented herein provide some important new details of the structural dynamics that follow optical preparation of the S_2 state of a carotenoid by transitions in the main absorption band by demonstrating that the S_x state intermediate can be temporally and spectroscopically resolved in terms of a broad SE cross peak in the 2DES spectrum. Additionally, the results indicate that vertical transitions in the red tail region of the linear absorption spectrum prepare S_x directly, but the subsequent decay to the S_1 state is faster than with excitation in the main absorption band. Taken together, these findings clarify that the nonradiative decay mechanism is initiated by C–C and C=C stretching displacements from the Franck–Condon geometry followed by out-of-plane vibrational distortions of the isoprenoid backbone. The out-of-plane character of S_x and S_1 is revealed especially by the mixing of the character of the vibrational modes from the isoprenoid backbone that contribute to the excited-state vibrational coherence and by their prominence in the anisotropy.

The general hypothesis that has emerged from our work on carotenoids so far is that although the S_0 state tends to favor essentially planar, all-trans structures, absorption of light causes the S_2 state to evolve rapidly toward a pyramidal conformation near a seam of CIs with the S_1 state. Figure 2.9 provides a schematic description of this picture by sketching how the potential energy surfaces of the singlet excited states of a carotenoid depend on a reaction coordinate initiated by optical excitation to the S_2 state. The key event in the proposed nonradiative decay pathway from S_2 to S_1 is the passage over a low barrier on the S_2 potential surface that divides the regions favoring planar and out-of-plane

distorted structures. The present results emphasize that most of these events, even passage to S_1 , occur on timescales shorter than those for pure vibrational dephasing.

The S_x state is attributed in this picture to molecules that have begun out-of-plane deformations near the barrier region on the S_2 surface after an initial displacement principally along the ω_1 and ω_2 , C=C and C-C stretching modes of the isoprenoid backbone. The initial displacement from the Franck-Condon geometry contributes to the change in bond-length alternation along the isoprenoid backbone that is noted upon excitation to the S_2 state,⁵¹ and it gives rise to the ground-state vibrational coherences that contribute to the oscillation maps near the diagonal of the 2DES spectrum. In a previous review,³ we suggested that the presence of low barriers on the potential surfaces for the singlet excited states provides a ready explanation for the time evolution of the ESA signals in the near-IR assigned to S_x , as observed by Cerullo et al.⁹ in their broadband pump-probe experiments. The barrier on the S_2 surface has the additional implication that tuning of the excitation energy controls the fraction of the S_2 molecules having enough potential energy to cross over the barrier.⁶ Depending on the energy of the Franck-Condon geometry relative to the height of the barrier, the S_x state would be formed by crossing the barrier within a vibrational period of the C=C and C-C stretching modes or the S_2 state would be retained in the planar minimum region. Given that global modeling of the main band excitation region of the 2DES spectra from CAN does not require a branched radiationless decay pathway, we suggest that the carbonyl substituents lower the effective barrier height significantly compared to that of an unsubstituted carotenoid like β -carotene by stabilizing the gradient region of the potential surface, which develops an ICT character as the molecule advances along the out-of-plane coordinates to the CI seam near the S_2 (S_x) minimum.

The scheme shown in Figure 2.9 suggests that excitations in the red tail region would prepare S_x directly via vertical optical transitions directly to the out-of-plane gradient of the S_2 potential surface. The results are consistent with this idea because the global model for the red tail excitation region of the 2DES spectrum indicates that the Franck–Condon S_2 state has a negligible lifetime prior to evolution to the S_x compartment and because these molecules eventually yield an S_1 compartment exhibiting a spectral profile matching that for S_1 with the main band excitation. The oscillation maps indicate that excitations of this region of the spectrum results in enhanced mixing of the vibrational modes of the isoprenoid backbone compared to excitations of the main band region of the linear absorption spectrum because the combination peaks are more prominent than in the main band region.

For molecules passing over the barrier after excitation in the main absorption band or optically prepared past the barrier in the red tail region, the scheme shown in Figure 2.9 further suggests that the S_1 state is formed by evolution down the S_2 gradient and through a seam of CIs near the S_2 minimum. The lifetime of S_x detected in the red tail region is considerably shorter, by a factor of four, than that detected in the main band; the larger initial force of displacement that would arise from a direct optical transition to the S_x gradient and the shorter distance along the reaction coordinate from the Franck–Condon geometry to the CI seam may contribute to this shortening of the lifetime. In both cases, however, solvent friction would retard the evolution along the reaction coordinate near the CI seam owing to the induction of ICT character that accompanies increasing out-of-plane displacement of a conjugated polyene.^{52,53} It should be kept in mind, however, that this picture for the potential energy surfaces is intrinsically multicoordinate. The structural

trajectory taken following a vertical excitation to the gradient on the S_2 potential surface due to excitation in the red tail region may be considerably different from that after excitation in the main band, which implies that the S_1 structures produced upon

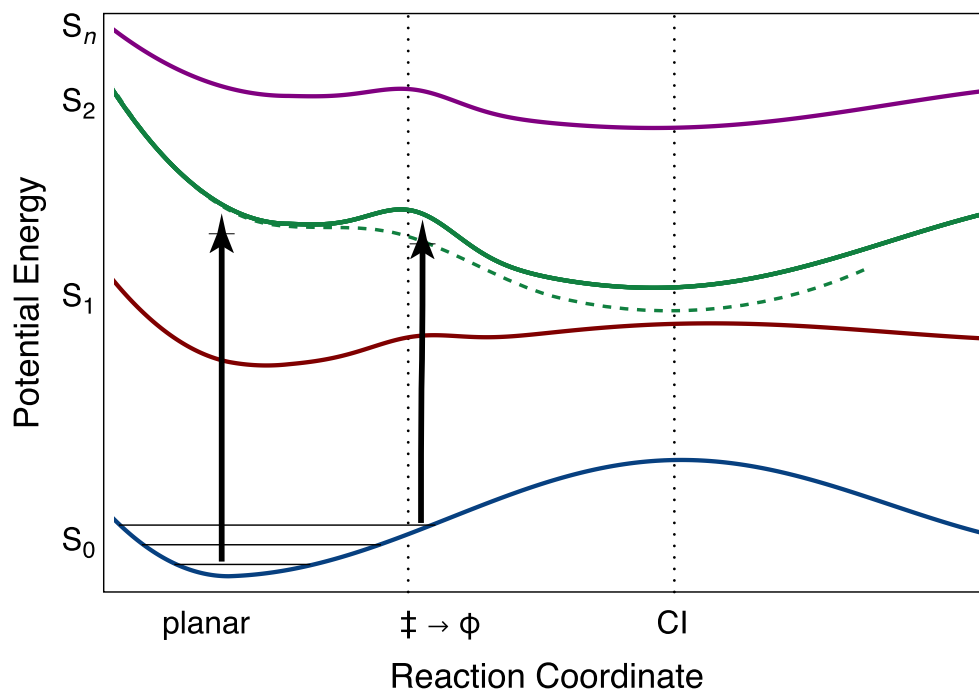


Figure 2.9. Schematic representations for the potential energy surfaces for the singlet states of a carotenoid, plotted here as a function of a reaction coordinate composed of sequential displacements from the Franck–Condon geometry of the optically prepared S_2 state with respect to the C–C and C=C stretching and out-of-plane (ϕ) coordinates of the isoprenoid backbone. Planar and distorted conformations are divided by a low barrier at the structure marked ‡ on the reaction coordinate axis. The dashed curve indicates that the S_2 surface will be stabilized by displacements with respect to the out-of-plane coordinates when the isoprenoid backbone is carbonyl substituted, as in CAN. The mixed S_2 , S_1 , and S_0 surfaces are proposed to converge near the geometry of the S_2 minimum owing to a conical intersection (CI) of the diabatic surfaces. Arrows indicate vertical optical transitions from planar and distorted conformations to the S_2 state. Adapted from Ref. 6.

nonradiative decay might have different conformations. This idea is suggested by the finding that the lifetime of S_1 is somewhat longer with excitation in the red tail region than in the main absorption band.

Despite the solvent friction near to the CI seam, the results show definitively that the S_1 state is formed with retention of vibrational coherence after passing from the S_x part of the S_2 potential surface. This finding is in agreement with the conclusions by Liebel et al.⁴⁷ for β -carotene, where excited-state vibrational coherence in several modes lacking resonance Raman activity was observed in S_1 . Figures A2.8 and A2.10 indicate, however, that the vibrational coherence near the center of the ESA cross peak from S_1 is stronger in the red tail than with excitation in the main band. This finding is consistent with the shorter lifetime observed for S_x for the red tail region. The modulated waveform detected for the main band excitation (Figure A2.8) in this case is relatively weak compared to the confidence intervals for the amplitude samples, but even here the results indicate that S_1 is formed with retention of vibrational coherence because peaks are evident below the diagonal in the oscillation maps at 1800 cm^{-1} (Figure A2.6). Owing to partial inversion of the C-C/C=C bond-length alternation pattern in the S_1 state,⁵¹ the mode frequency for the C=C bond upshifts markedly to 1785 cm^{-1} from the 1520 cm^{-1} natural frequency observed in the resonance Raman spectrum for all-trans or cis configurations, respectively.^{35,46,47,54,55}

The present results regrettably do not provide definitive information on the vibrational modes that promote nonradiative decay from S_x to S_1 for CAN. The principal modes of the isoprenoid backbone have relatively short damping times, $<400\text{ fs}$, which is similar to the lifetime of S_x , but they undergo several vibrational recurrences during the passage from the Franck-Condon region to the CI seam. Accordingly, these components are likely to be

serving as spectator modes rather than driving progress along the reaction coordinate. In contrast, especially considering the probable contribution from solvent friction as the ICT character develops, the reaction-coordinate modes ought to be much more rapidly damped. Indeed, the tuning and coupling modes that define the branching plane⁵⁶ for the CI seam with S_1 might be expected only to carry out only a single excursion after being launched by the onset of the S_x gradient. Alternative candidates for the branching modes for the nonadiabatic mechanism would include delocalized torsional modes of the isoprenoid backbone at natural frequencies in the 300–700 cm^{-1} region.⁴³ These modes would be expected to be strongly damped near the CI seam, but their half periods are compatible with the anisotropy kinetics and the S_x lifetimes determined in the global models.

REFERENCES

- (1) Polívka, T.; Sundström, V. Ultrafast Dynamics of Carotenoid Excited States-from Solution to Natural and Artificial Systems. *Chem. Rev.* **2004**, *104* (4), 2021–2071.
- (2) Polívka, T.; Sundström, V. Dark Excited States of Carotenoids: Consensus and Controversy. *Chem. Phys. Lett.* **2009**, *477* (1), 1–11.
- (3) Beck, W. F.; Bishop, M. M.; Roscioli, J. D.; Ghosh, S.; Frank, H. A. Excited State Conformational Dynamics in Carotenoids: Dark Intermediates and Excitation Energy Transfer. *Arch. Biochem. Biophys.* **2015**, *572*, 175–183.
- (4) Hashimoto, H.; Uragami, C.; Yukihiro, N.; Gardiner, A. T.; Cogdell, R. J. Understanding/Unravelling Carotenoid Excited Singlet States. *J. R. Soc. Interface* **2018**, *15* (141). <https://doi.org/10.1098/rsif.2018.0026>.
- (5) Fiedor, L.; Dudkowiak, A.; Pilch, M. The Origin of the Dark S1 State in Carotenoids: A Comprehensive Model. *J. R. Soc. Interface* **2019**, *16* (158), 20190191.
- (6) Gurchiek, J. K.; Rose, J. B.; Guberman-Pfeffer, M. J.; Tilluck, R. W.; Ghosh, S.; Gascón, J. A.; Beck, W. F. Fluorescence Anisotropy Detection of Barrier Crossing and Ultrafast Conformational Dynamics in the S2 State of β -Carotene. *J. Phys. Chem. B* **2020**. <https://doi.org/10.1021/acs.jpcc.0c06961>.
- (7) Levine, B. G.; Martínez, T. J. Isomerization through Conical Intersections. *Annu. Rev. Phys. Chem.* **2007**, *58*, 613–634.
- (8) Tully, J. C. Perspective: Nonadiabatic Dynamics Theory. *J. Chem. Phys.* **2012**, *137* (22), 22A301.
- (9) Cerullo, G.; Polli, D.; Lanzani, G.; De Silvestri, S.; Hashimoto, H.; Cogdell, R. J. Photosynthetic Light Harvesting by Carotenoids: Detection of an Intermediate Excited State. *Science* **2002**, *298* (5602), 2395–2398.
- (10) Sugisaki, M.; Fujiwara, M.; Nair, S. V.; Ruda, H. E.; Cogdell, R. J.; Hashimoto, H. Excitation-Energy Dependence of Transient Grating Spectroscopy in β -Carotene. *Phys. Rev. B Condens. Matter* **2009**, *80* (3), 035118.
- (11) Ghosh, S.; Bishop, M. M.; Roscioli, J. D.; Mueller, J. J.; Shepherd, N. C.; LaFountain, A. M.; Frank, H. A.; Beck, W. F. Femtosecond Heterodyne Transient-Grating Studies of Nonradiative Decay of the S2 (1(1)Bu(+)) State of β -Carotene: Contributions from Dark Intermediates and Double-Quantum Coherences. *J. Phys. Chem. B* **2015**, *119* (47), 14905–14924.

- (12) Tavan, P.; Schulten, K. Electronic Excitations in Finite and Infinite Polyenes. *Phys. Rev. B Condens. Matter* **1987**, *36* (8), 4337–4358.
- (13) Tavan, P.; Schulten, K. The Low-Lying Electronic Excitations in Long Polyenes: A PPP-MRD-CI Study. *J. Chem. Phys.* **1986**, *85* (11), 6602–6609.
- (14) Zhang, J.-P.; Inaba, T.; Watanabe, Y.; Koyama, Y. Sub-Picosecond Time-Resolved Absorption Spectroscopy of All-Trans-Neurosporene in Solution and Bound to the LH2 Complex from Rhodobacter Sphaeroides G1C. *Chem. Phys. Lett.* **2000**, *331* (2), 154–162.
- (15) Ostroumov, E. E.; Mulvaney, R. M.; Cogdell, R. J.; Scholes, G. D. Broadband 2D Electronic Spectroscopy Reveals a Carotenoid Dark State in Purple Bacteria. *Science* **2013**, *340* (6128), 52–56.
- (16) Jonas, D. M. Two-Dimensional Femtosecond Spectroscopy. *Annu. Rev. Phys. Chem.* **2003**, *54*, 425–463.
- (17) Azumi, T.; Matsuzaki, K. What Does the Term “Vibronic Coupling” Mean? *Photochem. Photobiol.* **1977**, *25* (3), 315–326.
- (18) Bizimana, L. A.; Carbery, W. P.; Gellen, T. A.; Turner, D. B. Signatures of Herzberg-Teller Coupling in Three-Dimensional Electronic Spectroscopy. *J. Chem. Phys.* **2017**, *146* (8), 084311.
- (19) Ghosh, S.; Roscioli, J. D.; Bishop, M. M.; Gurchiek, J. K.; LaFountain, A. M.; Frank, H. A.; Beck, W. F. Torsional Dynamics and Intramolecular Charge Transfer in the S₂ (1(1)Bu(+)) Excited State of Peridinin: A Mechanism for Enhanced Mid-Visible Light Harvesting. *J. Phys. Chem. Lett.* **2016**, *7* (18), 3621–3626.
- (20) Ghosh, S.; Bishop, M. M.; Roscioli, J. D.; LaFountain, A. M.; Frank, H. A.; Beck, W. F. Femtosecond Heterodyne Transient Grating Studies of Nonradiative Deactivation of the S₂ (1(1)Bu(+)) State of Peridinin: Detection and Spectroscopic Assignment of an Intermediate in the Decay Pathway. *J. Phys. Chem. B* **2016**, *120* (15), 3601–3614.
- (21) Kerfeld, C. A.; Melnicki, M. R.; Sutter, M.; Dominguez-Martin, M. A. Structure, Function and Evolution of the Cyanobacterial Orange Carotenoid Protein and Its Homologs. *New Phytol.* **2017**, *215* (3), 937–951.
- (22) Shim, S.-H.; Zanni, M. T. How to Turn Your Pump-Probe Instrument into a Multidimensional Spectrometer: 2D IR and Vis Spectroscopies via Pulse Shaping. *Phys. Chem. Chem. Phys.* **2009**, *11* (5), 748–761.

- (23) Lozovoy, V. V.; Pastirk, I.; Dantus, M. Multiphoton Intrapulse Interference. IV. Ultrashort Laser Pulse Spectral Phase Characterization and Compensation. *Opt. Lett.* **2004**, *29* (7), 775–777.
- (24) DeLong, K. W.; Trebino, R.; Hunter, J.; White, W. E. Frequency-Resolved Optical Gating with the Use of Second-Harmonic Generation. *J. Opt. Soc. Am. B, JOSAB*. <https://doi.org/10.1364/JOSAB.11.002206>.
- (25) Augulis, R.; Zigmantas, D. Two-Dimensional Electronic Spectroscopy with Double Modulation Lock-in Detection: Enhancement of Sensitivity and Noise Resistance. *Opt. Express* **2011**, *19* (14), 13126–13133.
- (26) Alavi, D. S.; Hartman, R. S.; Waldeck, D. H. Optically Heterodyned Polarization Spectroscopy. Measurement of the Orientational Correlation Function. *J. Chem. Phys.* **1990**, *92* (7), 4055–4066.
- (27) Wynne, K.; Hochstrasser, R. M. Anisotropy as an Ultrafast Probe of Electronic Coherence in Degenerate Systems Exhibiting Raman Scattering, Fluorescence, Transient Absorption and Chemical Reactions. *J. Raman Spectrosc.* **1995**, *26* (7), 561–569.
- (28) Wynne, K.; Hochstrasser, R. M. Coherence Effects in the Anisotropy of Optical Experiments. *Chem. Phys.* **1993**, *171* (1), 179–188.
- (29) Kitney-Hayes, K. A.; Ferro, A. A.; Tiwari, V.; Jonas, D. M. Two-Dimensional Fourier Transform Electronic Spectroscopy at a Conical Intersection. *J. Chem. Phys.* **2014**, *140* (12), 124312.
- (30) Gurchiek, J. K.; Bao, H.; Domínguez-Martín, M. A.; McGovern, S. E.; Marquardt, C. E.; Roscioli, J. D.; Ghosh, S.; Kerfeld, C. A.; Beck, W. F. Fluorescence and Excited-State Conformational Dynamics of the Orange Carotenoid Protein. *J. Phys. Chem. B* **2018**, *122* (6), 1792–1800.
- (31) Balevičius, V., Jr; Pour, A. G.; Savolainen, J.; Lincoln, C. N.; Lukeš, V.; Riedle, E.; Valkunas, L.; Abramavicius, D.; Hauer, J. Vibronic Energy Relaxation Approach Highlighting Deactivation Pathways in Carotenoids. *Phys. Chem. Chem. Phys.* **2015**, *17* (29), 19491–19499.
- (32) van Stokkum, I. H. M.; Larsen, D. S.; van Grondelle, R. Global and Target Analysis of Time-Resolved Spectra. *Biochim. Biophys. Acta* **2004**, *1657* (2–3), 82–104.
- (33) Chábera, P.; Fuciman, M.; Hříbek, P.; Polívka, T. Effect of Carotenoid Structure on Excited-State Dynamics of Carbonyl Carotenoids. *Phys. Chem. Chem. Phys.* **2009**, *11* (39), 8795–8803.

- (34) de Weerd, F. L.; van Stokkum, I. H. M.; van Grondelle, R. Subpicosecond Dynamics in the Excited State Absorption of All-Trans- β -Carotene. *Chem. Phys. Lett.* **2002**, *354* (1), 38–43.
- (35) Macpherson, A. N.; Gillbro, T. Solvent Dependence of the Ultrafast S₂–S₁ Internal Conversion Rate of β -Carotene. *J. Phys. Chem. A* **1998**, *102* (26), 5049–5058.
- (36) Robert, B. Resonance Raman Spectroscopy. *Photosynth. Res.* **2009**, *101* (2–3), 147–155.
- (37) Llansola-Portoles, M. J.; Pascal, A. A.; Robert, B. Electronic and Vibrational Properties of Carotenoids: From in Vitro to in Vivo. *J. R. Soc. Interface* **2017**, *14* (135).
<https://doi.org/10.1098/rsif.2017.0504>.
- (38) Butkus, V.; Zigmantas, D.; Valkunas, L.; Abramavicius, D. Vibrational vs. Electronic Coherences in 2D Spectrum of Molecular Systems. *Chem. Phys. Lett.* **2012**, *545*, 40–43.
- (39) Egorova, D. Self-Analysis of Coherent Oscillations in Time-Resolved Optical Signals. *J. Phys. Chem. A* **2014**, *118* (44), 10259–10267.
- (40) Farfan, C. A.; Turner, D. B. Interference among Multiple Vibronic Modes in Two-Dimensional Electronic Spectroscopy. *Sci. China Ser. A Math.* **2020**, *8* (2), 157.
- (41) Butkus, V.; Zigmantas, D.; Abramavicius, D.; Valkunas, L. Distinctive Character of Electronic and Vibrational Coherences in Disordered Molecular Aggregates. *Chem. Phys. Lett.* **2013**, *587*, 93–98.
- (42) Niu, K.; Lee, S.-Y. Analysis of Time Resolved Femtosecond and Femtosecond/Picosecond Coherent Anti-Stokes Raman Spectroscopy: Application to Toluene and Rhodamine 6G. *J. Chem. Phys.* **2012**, *136* (6), 064504.
- (43) Koyama, Y.; Takatsuka, I.; Nakata, M.; Tasumi, M. Raman and Infrared Spectra of the All-Trans, 7-Cis, 9-Cis, 13-Cis and 15-Cis Isomers of β -Carotene: Key Bands Distinguishing Stretched or Terminal-Bent Configurations Form Central-Bent Configurations. *J. Raman Spectrosc.* **1988**, *19* (1), 37–49.
- (44) Okamoto, H.; Sekimoto, Y.; Tasumi, M. Assignment and Anharmonicity Analysis of Overtone and Combination Bands Observed in the Resonance Raman Spectra of Carotenoids. *Spectrochim. Acta A* **1994**, *50* (8), 1467–1473.
- (45) Ou-Yang, S.-L.; Wu, N.-N.; Tian, Y.-J. Effect of High Pressure on the Molecular Structure and π -Electrons Delocalization of Canthaxanthin as Revealed by Raman Spectra. *Journal of Spectroscopy* **2015**, *2015*. <https://doi.org/10.1155/2015/467089>.
- (46) Liebel, M.; Kukura, P. Broad-Band Impulsive Vibrational Spectroscopy of Excited Electronic States in the Time Domain. *J. Phys. Chem. Lett.* **2013**, *4* (8), 1358–1364.

- (47) Liebel, M.; Schnedermann, C.; Kukura, P. Vibrationally Coherent Crossing and Coupling of Electronic States during Internal Conversion in β -Carotene. *Phys. Rev. Lett.* **2014**, *112* (19), 198302.
- (48) Qian, W.; Jonas, D. M. Role of Cyclic Sets of Transition Dipoles in the Pump-Probe Polarization Anisotropy: Application to Square Symmetric Molecules and Perpendicular Chromophore Pairs. *J. Chem. Phys.* **2003**, *119* (3), 1611–1622.
- (49) Farrow, D. A.; Smith, E. R.; Qian, W.; Jonas, D. M. The Polarization Anisotropy of Vibrational Quantum Beats in Resonant Pump-Probe Experiments: Diagrammatic Calculations for Square Symmetric Molecules. *J. Chem. Phys.* **2008**, *129* (17), 174509.
- (50) Dolan, P. M.; Miller, D.; Cogdell, R. J.; Birge, R. R.; Frank, H. A. Linear Dichroism and the Transition Dipole Moment Orientation of the Carotenoid in the LH2 Antenna Complex in Membranes of Rhodospseudomonas Acidophila Strain 10050. *J. Phys. Chem. B* **2001**, *105* (48), 12134–12142.
- (51) Fuß, W.; Haas, Y.; Zilberg, S. Twin States and Conical Intersections in Linear Polyenes. *Chem. Phys.* **2000**, *259* (2), 273–295.
- (52) Michl, J.; Bonacic-Koutecky, V. *Electronic Aspects of Organic Photochemistry*; Wiley, 1990.
- (53) Malhado, J. P.; Spezia, R.; Hynes, J. T. Dynamical Friction Effects on the Photoisomerization of a Model Protonated Schiff Base in Solution. *J. Phys. Chem. A* **2011**, *115* (16), 3720–3735.
- (54) Hashimoto, H.; Koyama, Y. The C—C Stretching Raman Lines of [β -Carotene Isomers in the S1 State as Detected by Pump-Probe Resonance Raman Spectroscopy. *Chem. Phys. Lett.* **1989**, *154* (4), 321 – 325.
- (55) Kraack, J. P.; Wand, A.; Buckup, T.; Motzkus, M.; Ruhman, S. Mapping Multidimensional Excited State Dynamics Using Pump-Impulsive-Vibrational-Spectroscopy and Pump-Degenerate-Four-Wave-Mixing. *Phys. Chem. Chem. Phys.* **2013**, *15* (34), 14487–14501.
- (56) Atchity, G. J.; Xantheas, S. S.; Ruedenberg, K. Potential Energy Surfaces near Intersections. *J. Chem. Phys.* **1991**, *95* (3), 1862–1876.

APPENDIX

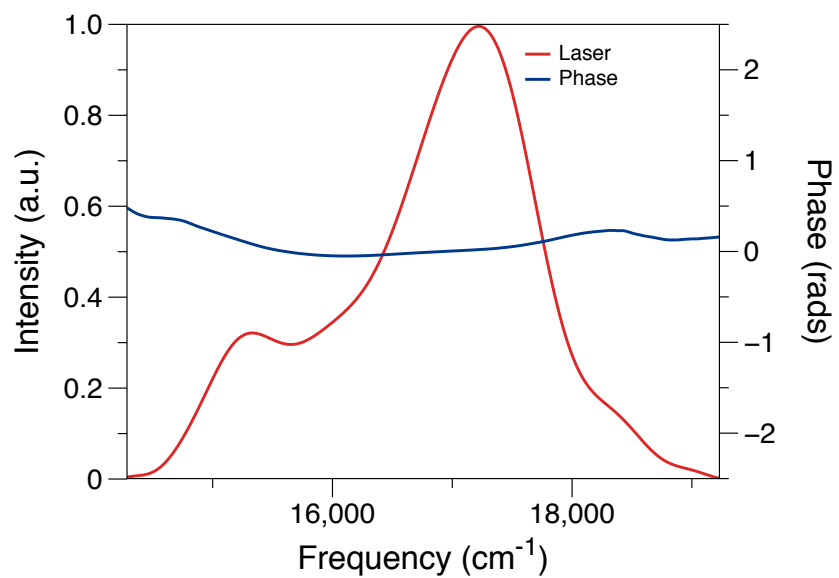


Figure A2.1. Laser intensity and residual phase spectrum for the laser pulses in the pump beam of the 2DES spectrometer, with the latter determined at the sample's position by MIIPS scans²³ after compression.

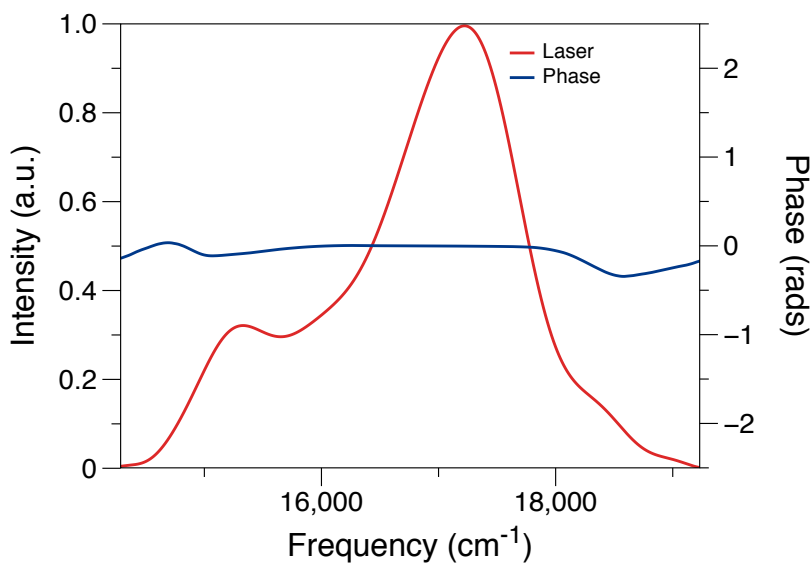


Figure A2.2. Laser intensity and residual phase spectrum for the laser pulses in the probe beam of the 2DES spectrometer, with the latter determined at the sample's position by MIIPS scans after compression.

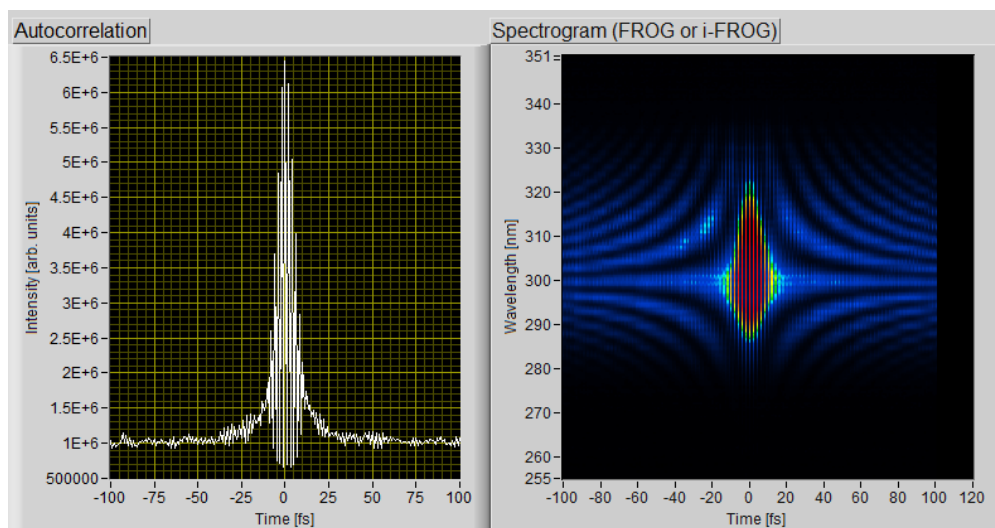


Figure A2.3. Interferometric autocorrelation and SHG-FROG²⁴ spectrograms for the pump pulses, as measured with scanned pulse pairs prepared by the pump beam's pulse shaper.

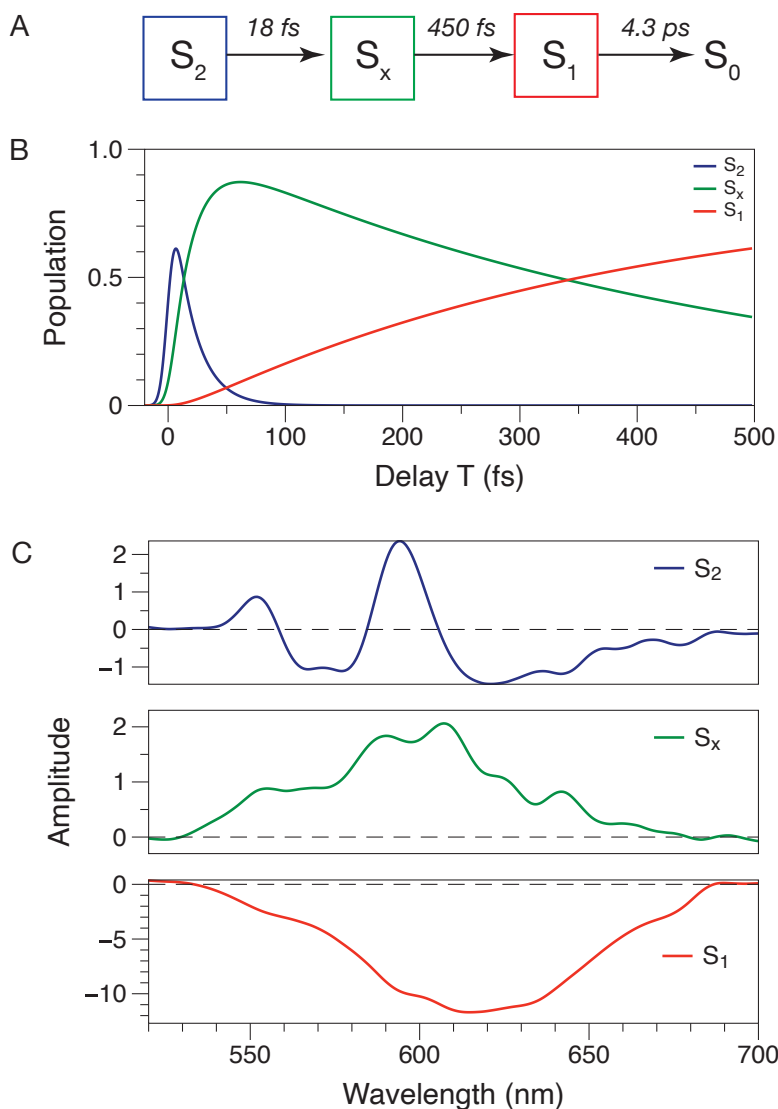


Figure A2.4. 1D global and target model for the 2DES spectra from CAN in toluene, with excitation at 18500 cm^{-1} (540 nm). (a) Kinetic scheme for nonradiative decay of the resonant S_2 state via the intermediate S_x to the S_1 state. (b) Time dependence of the populations for the S_2 , S_x , and S_1 spectrokinetic species. (c) Evolution-associated difference spectra (EADS) for the three spectrokinetic species.

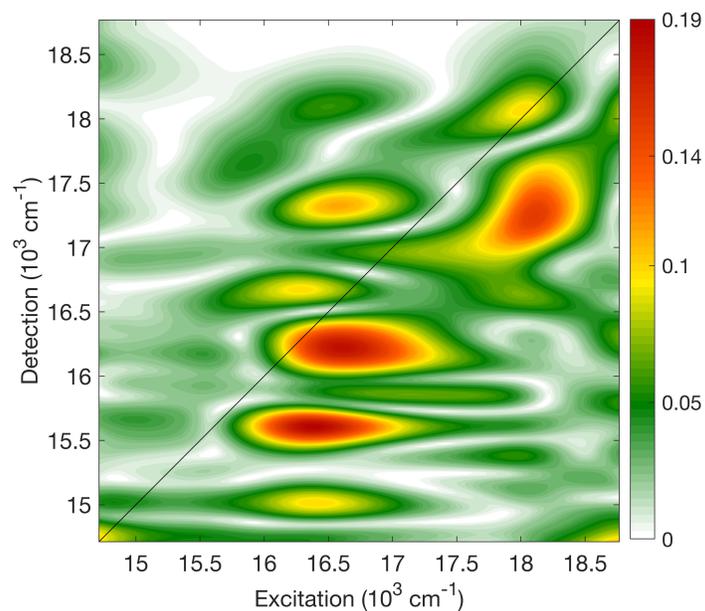


Figure A2.5. Oscillation map for vibrational coherence at 100 cm^{-1} detected in the 2DES K spectra from CAN in toluene.

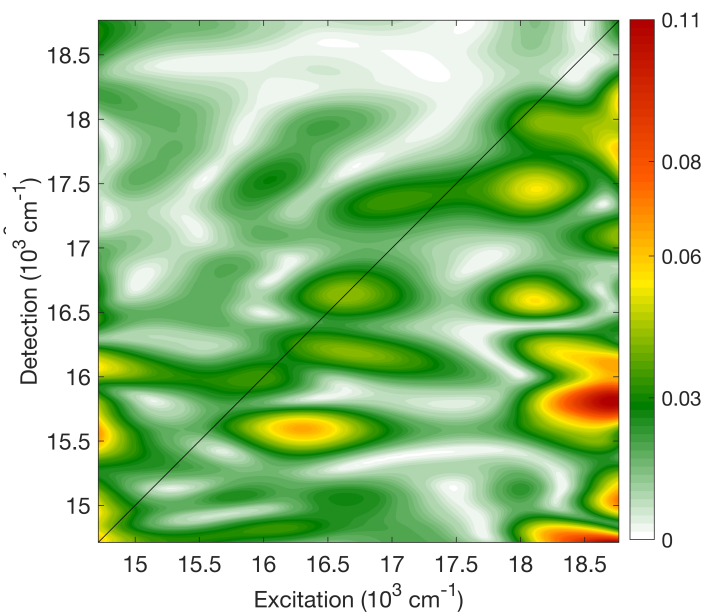


Figure A2.6. Oscillation map for vibrational coherence at 1800 cm^{-1} detected in the 2DES K spectra from CAN in toluene.

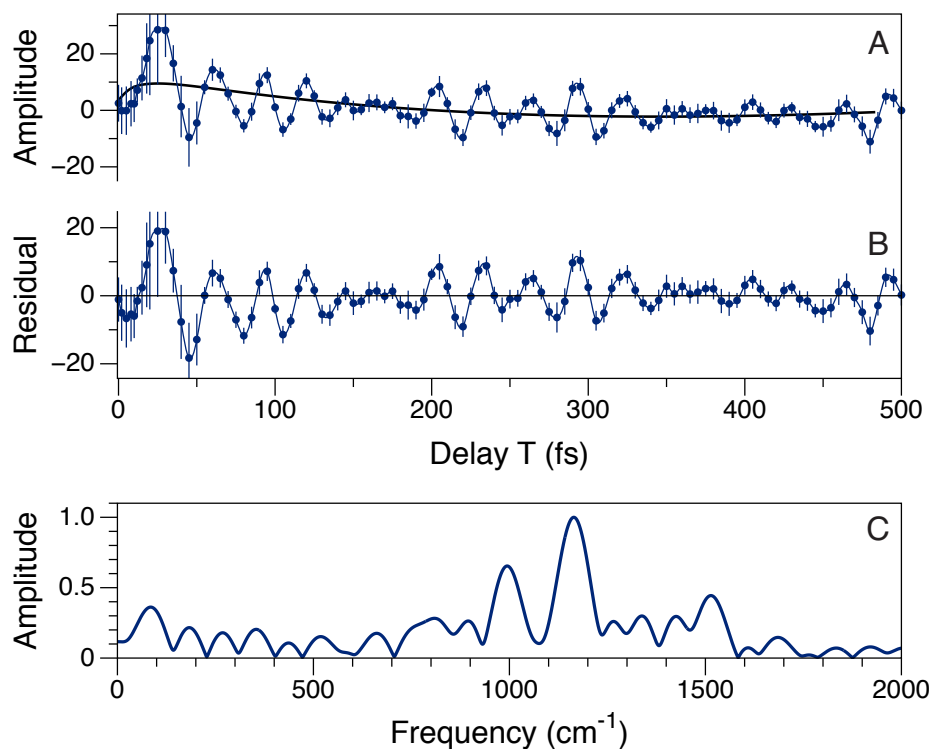


Figure A2.7. Total amplitude K transient and modulation spectrum on the diagonal in the main band excitation region. (a) K transient with excitation at 18200 cm^{-1} and detection at 18200 cm^{-1} , with the fit from the global model (red curve) superimposed. (b) Residual (K - global model) transient. (c) Fourier transform amplitude spectrum of the residual over the $T = 75\text{-}500\text{ fs}$ range. In (b,c) the bars show the 95% confidence intervals for the K amplitudes.

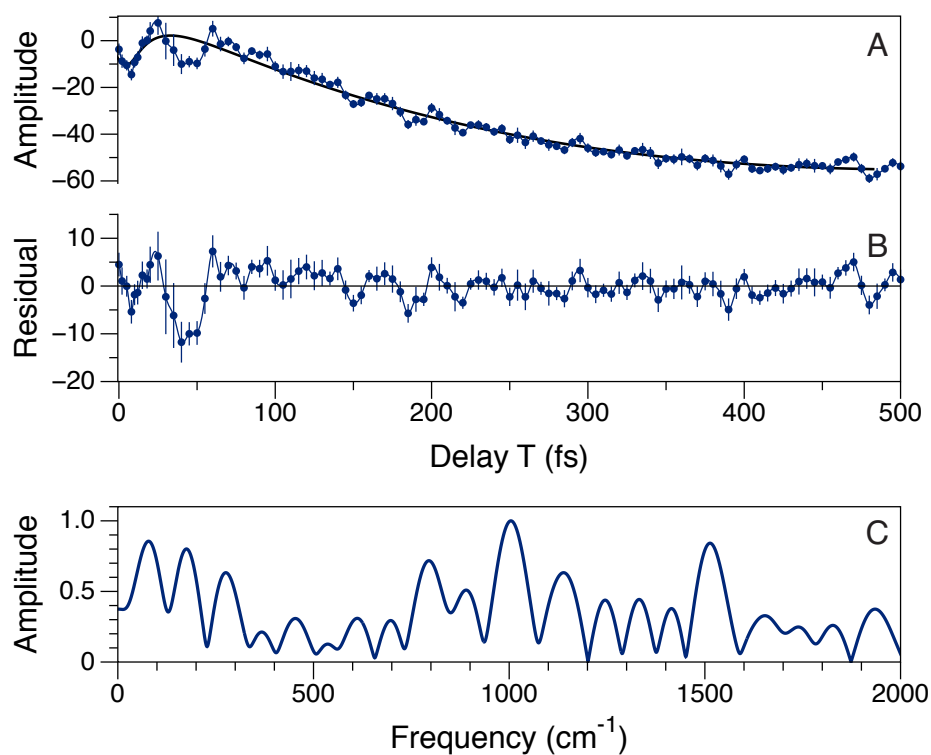


Figure A2.8. Total amplitude K transient and modulation spectrum in the S_1 cross peak in the main band excitation region. (a) K transient with excitation at 18200 cm^{-1} and detection at 15500 cm^{-1} , with the fit from the global model (red curve) superimposed. (b) Residual ($K - \text{global model}$) transient. (c) Fourier transform amplitude spectrum of the residual over the $T = 75\text{-}500 \text{ fs}$ range. In (b,c) the bars show the 95% confidence intervals for the K amplitudes.

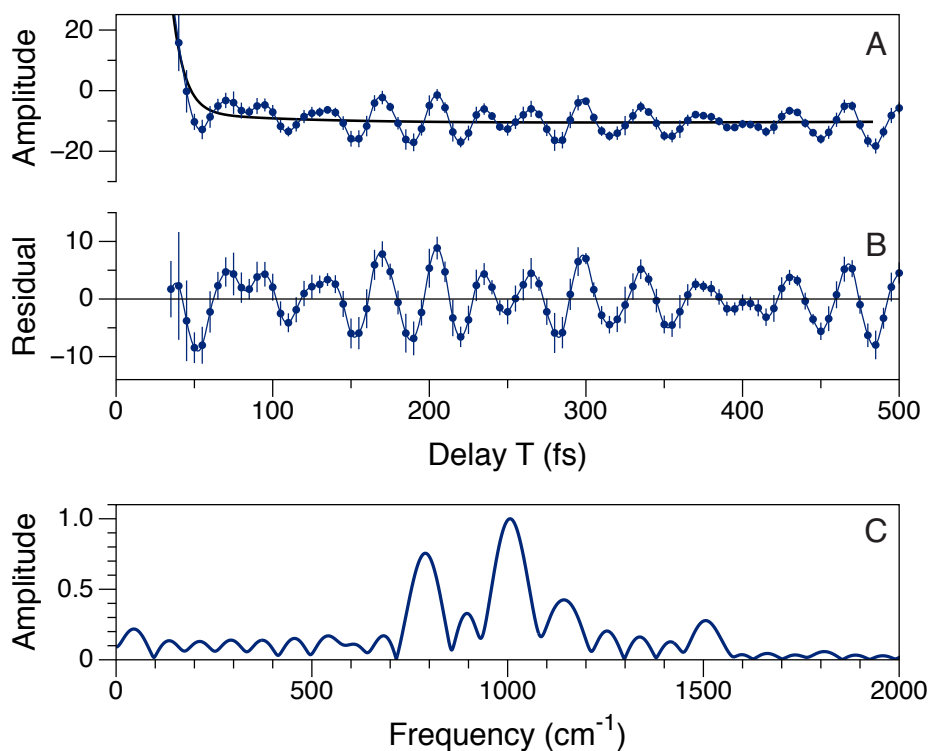


Figure A2.9. Total amplitude K transient and modulation spectrum on the diagonal in the red tail excitation region. (a) K transient with excitation at 17200 cm^{-1} and detection at 17200 cm^{-1} , with the fit from the global model (red curve) superimposed. (b) Residual (K - global model) transient. (c) Fourier transform amplitude spectrum of the residual over the $T = 75\text{-}500\text{ fs}$ range. In (b,c) the bars show the 95% confidence intervals for the K amplitudes.

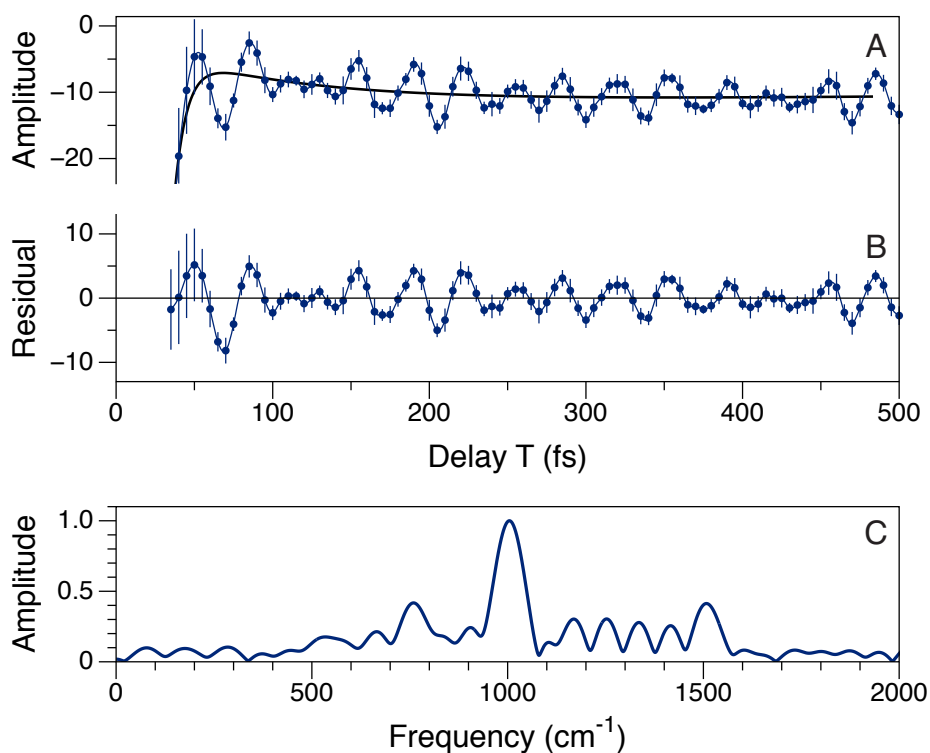


Figure A2.10. Total amplitude K transient and modulation spectrum in the S_1 cross peak in the red tail excitation region. (a) K transient with excitation at 17200 cm^{-1} and detection at 15500 cm^{-1} , with the fit from the global model (red curve) superimposed. (b) Residual (K - global model) transient. (c) Fourier transform amplitude spectrum of the residual over the $T = 75\text{-}500\text{ fs}$ range. In (b,c) the bars show the 95% confidence intervals for the K amplitudes.

Chapter 3: Electronic-Vibrational Coherences in Oleate-capped CdSe Quantum Dots

Exciton relaxation in semiconductor quantum dots (QDs) is strongly dependent on the nature and extent of passivation of the surface by organic ligands. To determine how the ligands participate in nonradiative decay mechanisms, we characterized preparation of CdSe QDs capped oleate ligands using broadband multidimensional spectroscopy with 7-fs laser pulses. Population transfer to the band edge and then to the photoluminescent state after optical preparation of the X3 exciton ($1P_e$ state) is revealed in two-dimensional electronic spectra (2DES) by the time evolution of an off-diagonal cross peak. This process involves excited-state coherent wavepacket motions through a cascade of conical intersections between exciton potential-energy surfaces. Excitation and mode specific oscillation maps allow us to probe excited state wavepacket motions at frequencies matching the vibrational modes of the organic ligands. These observations indicate that the ligand vibrations are quantum coherently mixed with the core electronic states of the QDs. These results raise new opportunities for engineering photoinduced electron transfer processes in QDs through control of electronic-vibrational coupling with organic ligands.

3.1 Introduction

Semiconductor quantum dots (QDs) are of high interest because their optoelectronic properties can be tuned by varying size, shape, and surface chemistry.¹⁻³ As a result, QDs are used in several applications including solar cells, lasers, catalysis, biomedical sensing, and imaging.^{4,5,58,61,64,67} In a photoexcited QD, the electrons that occupy higher energy levels ($1P_e$) above the band gap rapidly (subpicosecond regime) relax to a lower energy state via nonradiative relaxation.^{5,6} This irreversible loss of excitation energy in QDs contributes to low efficiency in photovoltaic applications. The nonradiative relaxation mechanism in QDs is strongly influenced by the interaction of QD core with the organic molecules on the surface.^{7,8}

Early reports from Guyot-Sionnest group have proposed that the surface ligands facilitate intraband relaxation via ligand vibrations. In such mechanism, ligand vibrational modes are considered to accept energy and serve as a sink to the electron relaxation from higher to lower electronic state.⁷ Further studies from Pandey and Guyot-Sionnest have shown that the intraband relaxation can be significantly slowed by isolating the QD core from the surface ligands by incorporating a ZnSe inorganic shell.⁸ The studies from Kambhampati group have reported the influence of surface and surface ligands in multiple aspects of carrier relaxation including electronic-to-vibrational energy transfer, electron-phonon coupling and Auger relaxation rates.⁹ They have shown that the holes in colloidal CdSe QDs relax through a surface based nonadiabatic channel while the electrons relax primarily through Auger mechanism.¹⁰

Owing to spatially confined excitonic wavefunctions, the core electronic states are quantum mechanically mixed with surface ligands by bonding interactions, which leads to

the delocalization of core electronic states to the surface ligands. Weiss and coworkers have investigated the relaxation of exciton confinement in QDs via delocalization of the core wavefunction to the surface ligands using phenyldithiocarbamate (PTC) molecule.^{11,12} The orbital overlap of PTC molecule with the QD core results in delocalization of the hole-wavefunction.¹¹ This delocalization of the wavefunction increases the exciton confinement radius of the QDs resulting in lower optical band gaps and thus a red-shift in the absorption spectrum. They have further manipulated these interactions to achieve photoinduced hole transfer from CdS QDs to phenothiazine molecular acceptor.¹³

The recent study from our group demonstrated that the vibrational motions of the surface ligands promote the nonradiative relaxation pathway in hexadecylamine-capped CdSe QDs via mixing of core electronic states of the quantum dot and vibrational states of the surface ligands.¹⁴ Modulations corresponding to torsional, wagging and scissoring modes of the alkylamine entities were observed during the relaxation from the X3 exciton energy level to lower energy levels like X1 and PL. This study proposed a nonadiabatic mechanism for the relaxation of X3 via a cascade of conical intersections (CIs)¹⁵ where coherent wavepacket motions are following the optical excitation of X3 (Figure 3.1). In this chapter, results from broadband multidimensional spectroscopic studies of vibronic coherences aiding the hot carrier cooling in oleate-capped CdSe quantum will be presented. Additionally, a global analysis of X3 is being carried out on these quantum dots to characterize the nature and kinetics of the exciton relaxation. The main results indicate that the stretching and rocking vibrational motions of the carboxylate along with mixed vibrations of QD core facilitate the vibronic exciton mechanism of hot-carrier cooling.

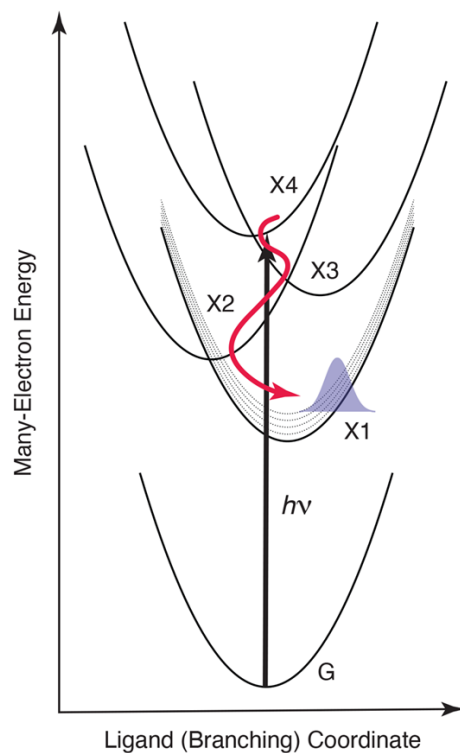


Figure 3.1. Schematic representation of the potential energy surface representing the relaxation of optical excitation via a cascade of conical intersections via coherent wavepacket motions. Adapted from Tilluck et al.¹⁴

3.2 Experimental Methods

3.2.1 CdSe Quantum Dot Synthesis and Characterization

The 2DES studies on CdSe quantum dots presented in this chapter were synthesized by the Van Patten laboratory at Middle Tennessee State University (MTSU). For the synthesis of these particles, cadmium oxide (99.5% metals basis) and oleic acid (99%) were purchased from Sigma Aldrich, St. Louis, MO. Chloroform (A.C.S. reagent grade) was obtained from Alfa Aesar (Haverhill, MA). Selenium powder was purchased from STREM (Newburyport, MA). Octadecene (90%) was purchased from Acros Organics (Geel, Belgium).

CdSe QDs were synthesized following a modified phosphine-free synthesis previously reported by Jasieniak et al.¹⁶ A Se precursor stock solution was prepared by evacuating 0.1280 g of Se in 16 mL of octadecene (ODE) for 30 min and then heating under nitrogen at 200°C for 2 h. A separate stock solution of Cd-oleate was prepared by evacuating 0.0478 g of CdO and 1.0163 g of 99% oleic acid in 12 mL of ODE for 30 min. The Cd solution was then heated under nitrogen at 100 °C for 1 h. The Cd-oleate solution was then heated to 285 °C, and 3.6 mL of the Se precursor was rapidly injected. The growth temperature was maintained at 265 °C for 30 min. After the first growth step, UV/Vis measurements were taken using a modernized Cary 14 spectrophotometer, and the absorbance was measured at 618 nm (5.49 nm diameter). A second injection was performed by heating the QD solution to 265 °C and slowly injecting 1 mL of the Se precursor using a New Era Pump Systems NE-300 syringe pump at a rate of 80 µL/min. The QD solution was then allowed to grow for an additional 30 min, after which UV/Vis measurements were taken, and the absorbance was measured at 640 nm (6.95 nm diameter). The resulting QD solution was purified by two cycles of precipitation by spinning in a microcentrifuge at 17000 × g and resuspension using a chloroform/acetonitrile solvent/antisolvent combination.

To verify the size of the QDs, transmission electron micrographs (TEM) were obtained using a Hitachi 7650 transmission electron microscope. A single drop of purified QDs suspended in toluene was deposited onto a carbon-coated copper TEM grid, which was then placed in a petri dish on filter paper and allowed to dry overnight. The microscope was operated at an accelerating voltage of 100 kV and at 500,000× direct magnification. The size distribution was determined using ImageJ software.

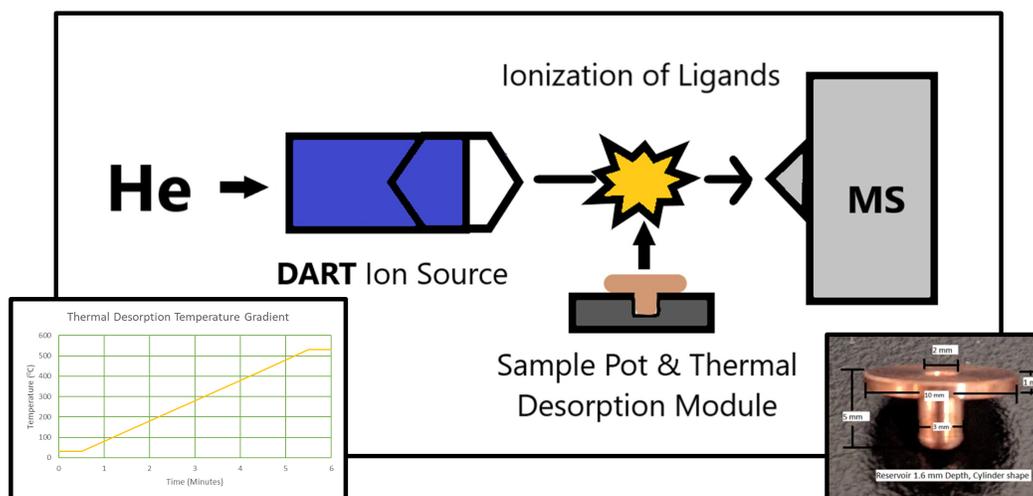


Figure 3.2. Schematics of DART-MS analysis. The sample was heated using a thermal desorption module where the ion source ionized the desorbed molecules. The mass spectrometer detects ionized ligand molecules and shows the signatures of the released species in the mass spectrum. Inset plot shows the linear temperature ramp applied over certain time.

The surface ligands of the QDs were analyzed using Thermal Desorption Direct Analysis in Real Time Mass Spectrometry (TD-DART-MS), as previously described by Frazier *et al* (Figure 3.2).¹⁷ In TD-DART-MS, a temperature ramp is applied with respect to time while measuring the mass spectrum of the ionized species. Using mass spectrometry, different ligand molecules can be distinguished from their mass spectrum with very high selectivity and sensitivity. The chemically bound species on the surface of the QDs can be readily distinguished from the physisorbed species. The weakly bound or the unbound species arrive at the detector at low temperatures and early time. Conversely, strongly bound or chemically bonded species arrive at higher temperature and at later time. Using a Thermo LTQ XL mass spectrometer coupled with a DART ion source and an IonRocket temperature gradient system, 5 μ L of the sample was analyzed at a time. The analysis of each sample was conducted using a temperature profile that increased from 30 to 530 $^{\circ}$ C at a rate of

100 °C/min, with a 30-s hold at 530 °C to ensure the complete desorption of ligands from the copper substrate. Additionally, each scan monitored m/z ranges from 50-1000, and the DART ion source He gas stream temperature was set to 400 °C.

3.2.2 Linear Spectroscopy and Photoluminescence

The QDs were dispersed in hexane to obtain an absorbance of 0.3 at 562 nm for the 2DES experiments. The absorption spectrum is measured using a Shimadzu-2600 UV-Vis-NIR spectrophotometer. The room temperature fluorescence was measured using a home-built fluorescence spectrometer employing a broadband visible LED and a compact double monochromator as an excitation source and a spectrograph and a CCD camera as the detector.¹⁸

3.2.3 Two-Dimensional Electronic Spectroscopy

2DES spectra were recorded using a pump-probe optical configuration with adaptive pulse shaping¹⁹ to compress the laser pulses and to generate the excitation pulse sequence (pulse 1- τ -pulse 2) required for the three-pulse stimulated photon-echo experiment. Excitation pulses were obtained from a noncollinear optical parametric amplifier (NOPA, Spectra-Physics Spirit-NOPA-3H), which was pumped by the third harmonic of a 1.04 μm amplified Yb laser (Spectra-Physics Spirit-4W, 400 fs pulses at a 100 kHz repetition rate, 4 W average power). The pump and probe beams in the spectrometer were split from the NOPA output by a broadband dielectric beamsplitter (Layertec, Mellingen), processed by an adaptive pulse shaper (FemtoJock and FemtoJock P, respectively, Biophotonic Solutions), and then compressed by multiple reflections on pairs of broadband chirped mirrors (Ultrafast Innovations, Munich). For the present experiments, the NOPA's signal beam output spectrum (Figure 3.5) was centered at 600 nm (~ 110 nm FWHM; 520–700

nm usable range). The excitation pulse energy was attenuated to 3.75 nJ per pulse, as measured at the sample's position. The pump beam's plane of linear polarization was rotated magic angle (54.7°) from that of the probe beam by a thin achromatic half-wave retarder plate. The two beams were focused by off-axis parabolic mirrors to 100 μm spots overlapped spatially just after the front window of the sample cuvette. The excitation pulses in both beams were characterized by MIIPS scans²⁰ conducted with a thin β -barium borate crystal, which was placed at the sample's position following a single cuvette window. The estimated pulse duration for both beams at the sample position was 6.9 fs. Residual phase plots (Figures A3.1), SHG-FROG spectrograms²¹ (Figure A3.2), and autocorrelation (Figure A3.3) are presented in the appendix.

2DES spectra were recorded by programming the pump beam's pulse shaper to scan the coherence time interval between the two pump pulses, τ , from 0 to 50 fs with 0.5 fs steps to obtain the excitation axis after Fourier transformation. The detection axis of the 2DES spectrum was measured directly by measuring the pump-induced change in probe transmission through the sample with a home-built 0.2 m spectrograph (300 gr/mm diffraction grating) and a fast CCD detector (Andor Newton 940) using a phase-sensitive detection protocol and amplitude modulation of the pump pulses.²² The population time T is scanned by a time-of-flight delay stages with a spacing of 2.5 fs from 0-30 fs, 5 fs spacing from 30-500 fs, 10 fs spacing from 500-800 fs, 50 fs spacing from 800-1000 fs and 1 ps spacing from 1-10 ps. Each 2D spectrum was an average of seven consecutive T scans. Owing to the use of the pump-probe optical geometry and amplitude modulation of the pump-pulse pair, the 2DES spectra reported here are intrinsically autophased. The spectra

obtained using this approach are the sum of those from the rephasing and non-rephasing nonlinear optical pathways.²²

3.3 Results

3.3.1 Particle Size and Surface Characterization

To study the vibronic character of the exciton relaxation in oleate-capped CdSe QDs, nanoparticles with a size of ~ 7 nm were used to perform the 2DES experiment. Transmission Electron Microscopy (TEM) has been carried out on these QDs to understand the size distribution (Figure 3.3a). TEM images show that the particles are highly monodisperse in shape and size (Figure 3.3b) and exhibit a zincblende crystal structure owing to their cubic symmetry. The mass spectra collected during the thermal desorption DART-MS showed that the desorbed ionic species detected were primarily oleate ions and its different ionic forms (Figure 3.3c). The temperature desorption profile of the sample at $m/z = 281.4$ indicates that the oleate ions were desorbed from the surface of the QD at 460 °C (Figure 3.3d). This confirms that the oleate ligands are the only surface ligands that are chemically bound to the QDs.

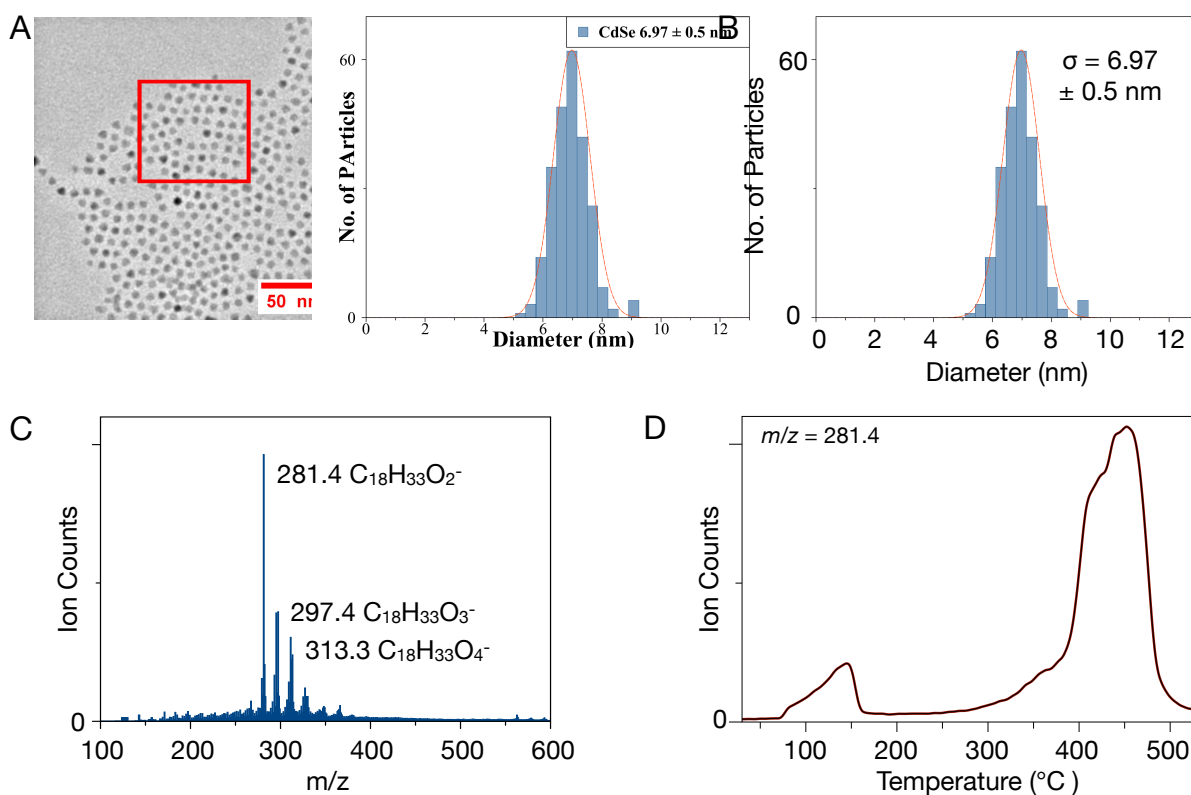


Figure 3.3. Characterization of oleate CdSe (a) Transmission electron microscopy images of oleate-capped CdSe quantum dots with 500,000x magnification and 5x zoom. (b) Size distribution of CdSe QDs, 245 total particles counted, 62 particles 6.98 nm. The mean of the size distribution is 6.97 nm with a standard deviation of 0.50 nm. Mass spectra collected from TD-DART-MS of oleate-capped CdSe QDs. The ligands are desorbed from the inorganic core at 430 °C. In addition to the major peak at $m/z = 281.4$ corresponding to the oleate anion, two peaks associated with subsequent additions of oxygen are observed at $m/z = 297.4$ and $m/z = 313.3$. Desorption plot obtained from DART-MS for $m/z = 281.4$.

3.3.2 Linear Spectroscopy

Upon incidence of photons, electrons are excited from the hole states in the valence band to the electronic states in the conduction band. In the 7-nm CdSe QDs, the lowest energy transition or the band edge exciton ($1S_{3/2} 1S_e$) is denoted as X1 (1.90 eV), the second exciton ($2S_{3/2} 1S_e$) is denoted as X2 (1.99 eV), the third exciton ($1P_{3/2} 1P_e$) as X3 (2.12 eV), and the fourth exciton ($3S_{1/2} 1S_e$) as X4 (2.31 eV). Figure 3.4a shows the various excitons created within the CdSe QDs, illustrating their positions in both the electron-hole

energy level and the exciton energy domain. These distinct excitons are represented by different colors (X1-red, X2-green, X3-blue, and X4-magenta) in the absorption spectrum (Figure 3.5). The broadband laser spectrum spans the first three excitons very well in this study. Coverage of the broadband spectrum allows us to study the population relaxation and coherent wavepacket dynamics from all three exciton levels simultaneously.

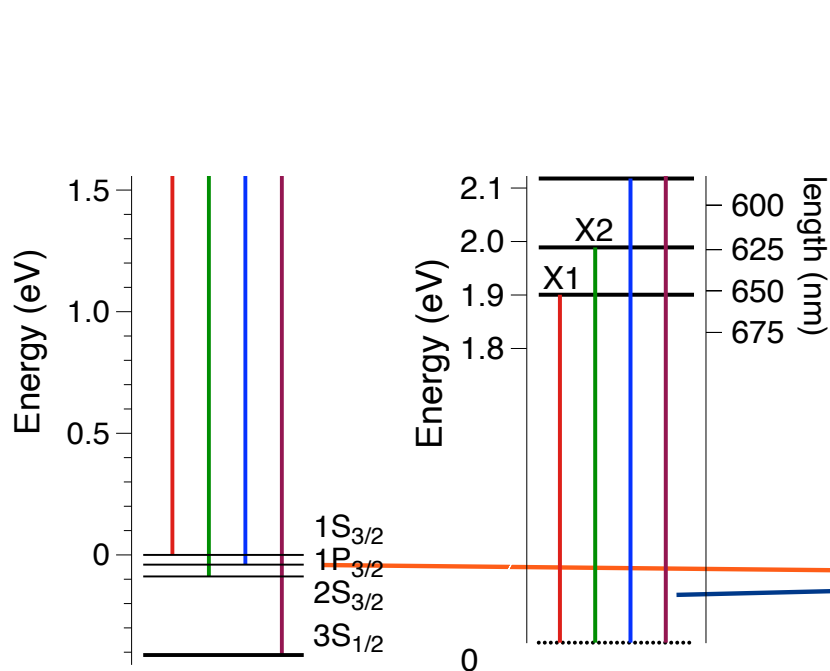


Figure 3.4. Energy level diagram of CdSe QDs. On the left, the electron-hole energy levels are marked with hole levels in the valence band ($1S_{3/2}$, $1P_{3/2}$, $2S_{3/2}$, $3S_{1/2}$) and electron levels ($1S_e$ and $1P_e$) in the conduction band. The band edge exciton ($1S_{3/2}$ $1S_e$) is denoted as X1, the second exciton ($2S_{3/2}$ $1S_e$) is denoted as X2, the third exciton ($1P_{3/2}$ $1P_e$) as X3, and the fourth exciton ($3S_{1/2}$ $1S_e$) as X4. The figure on the right shows the exciton energy levels of the first four excitons with energy in eV on the left and wavelength on the right.

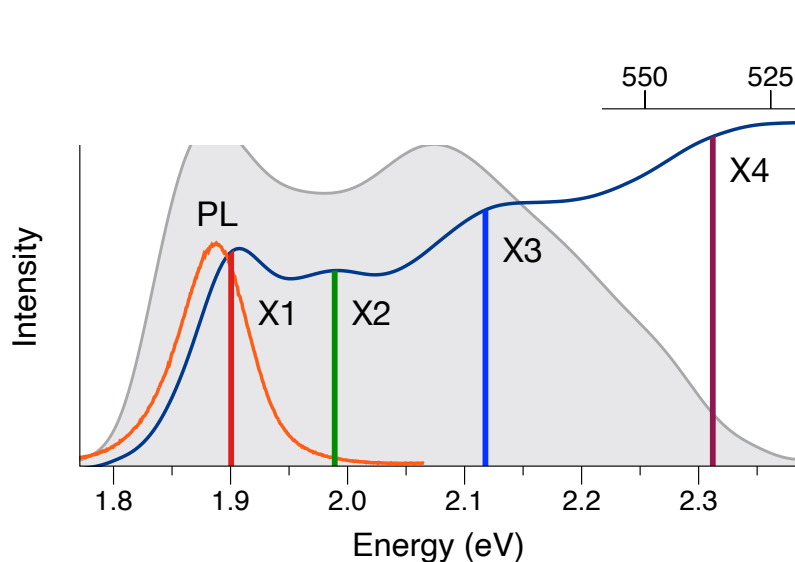


Figure 3.5. Steady-state spectroscopic characterization of oleate-capped QDs. Linear absorption spectrum (blue trace) marked with various exciton energy levels, and photoluminescence spectrum (orange trace) with overlapping laser spectrum (gray filled).

3.3.3 2DES Spectra

A series of 2D spectra with the absorption spectrum and overlapped laser spectra are shown in the Figure 3.6. In the short time delay, the 2D spectra exhibit partially resolved positive peaks along the diagonal resulting from the ground state bleaching (GSB) and stimulated emission (SE). The formation of diagonal peaks indicates preparation of population at different exciton energy levels after the photoexcitation from the pump pulses. An early time diagonal slice of 2D spectrum shows well resolved peaks that arise due to the fine structure of excitons in the QDs (solid blue line of side panel, Figure 3.5).

The origin of the fine structure of excitons in QDs is a combination of strong spin-orbit coupling, exchange interaction for singlet and triplet states and crystal field splitting arising from shape anisotropy.^{23,24} Early reports from Bawendi group investigated the fine structure in QDs using steady-state photoluminescence excitation and fluorescence line narrowing experiments.²⁴ These experiments were performed at very low temperatures

of 10 K and lacked time-resolved dynamics information. Previously several groups have used 2DES studies to understand the fine structure of CdSe and PbS QDs.^{23,25,26} However, these studies exclusively focused on probing the fine structure of the band edge exciton. Using broadband short pulses in this experiment allows us to monitor the fine structure of multiple excitons before the resultant spectral features undergo inhomogeneous broadening owing to interaction with the surroundings.

As the population time T evolves, the diagonal peaks broaden due to inhomogeneous broadening or loss of memory of the excitation owing to interactions with the surroundings. Apart from the broadening of spectral features, a strong cross peak appears at lower energies corresponding to X1, X2, and PL excited at higher energies. The formation of the cross peak in this region is due to the population relaxation from X3. Crosspeak formation can be observed at very short delays T , as short as 20 fs, suggesting that population relaxation occurs very rapidly.

The 2D spectra also shows negative blue signals corresponding to excited state absorption signals (ESA) arising from formation of trap states or biexcitons.^{23,27-29} The ESA signal that arise from the biexciton formation which can be viewed as transition from an excited state, X to a doubly excited state, XX in the QDs.²⁸ In a 2DES experiment, the pump pulses create a coherence between the ground state and exciton level X, the second pulse create a population in the excited state X the third probe pulse creates a coherence between X and biexcitonic state XX which emits a signal with frequency of energy gap between X and XX. The ESA features observed at detection energy, 1.85 eV with a wide range of excitation energies from 1.85-2.2 eV is likely to arise from biexcitonic interaction of the X1 with that of X1, X2 and X3. The ESA has also been observed during the formation of

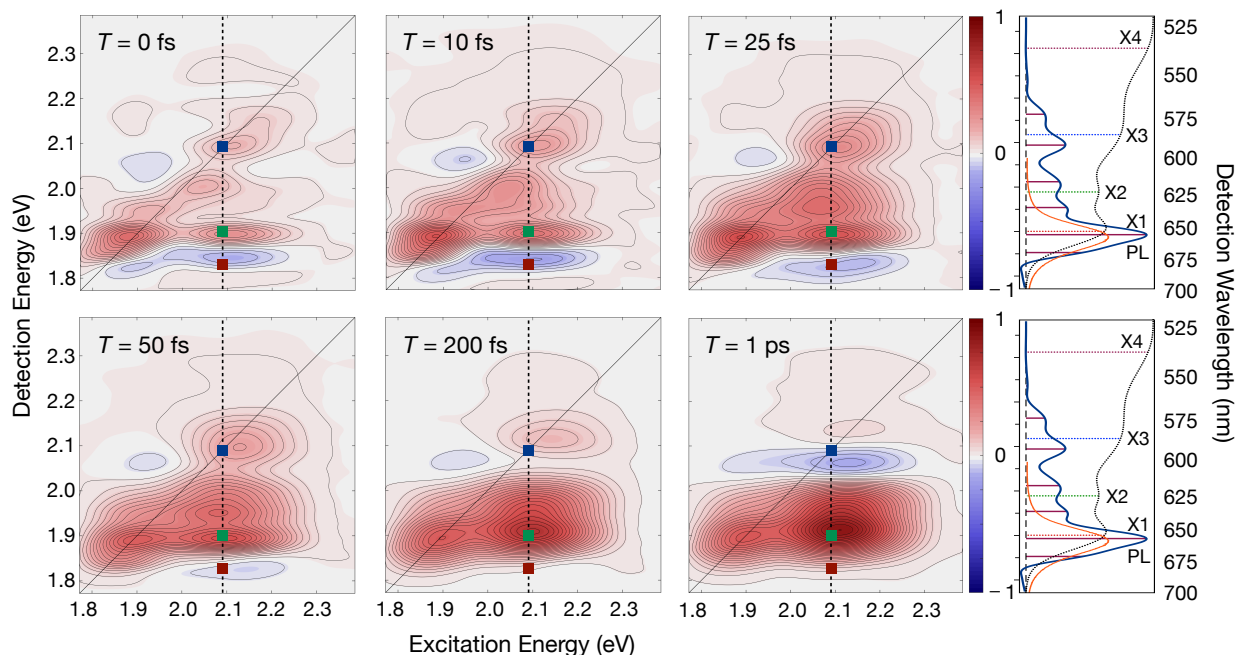


Figure 3.6. Time evolution of 2DES spectra of oleate capped CdSe quantum dots with respect to the population time, T . The spectra are presented with evenly spaced contours and are tinted with colors indicating positive (red, GSB/SE) and negative (blue, ESA/PA) signals. The side panels plot the 2DES signal amplitude sliced along the diagonal at $T = 0$ fs (blue) superimposed on the linear absorption oscillator strength (black dotted) and photoluminescence (PL) spectra (orange). Amplitude transients sampled at the marked coordinates (excitation at X3 and detection at X3, X1, and PL) are shown in Figure 3.7.

surface trap states when the surface of QDs is poorly passivated, with the unpassivated sites on the QDs' surface serving as carrier traps for electrons and holes. The 2D spectra at population times $T = 200$ fs and $T = 1$ ps show a high intensity crosspeak at lower energies indicating that the population from X3 has completely relaxed to lower energy states, X1 and PL. The relaxation of X3 is also apparent from the low amplitude of GSB/SE signals on the diagonal of the 2D spectrum at (X3, X3).

3.3.4 Global Modeling and Coherence Analysis

To understand the dynamics of X3 relaxation, the amplitude of the evolution of the nonoscillatory kinetic response excited at the energy level of X3 is subjected to global analysis (Figure 3.7). Global analysis models the evolution of spectral response as a linear

combination of evolution-associated difference spectra (EADS) of different spectrokinetic species.³⁰ Each of the EADS in the global model can be viewed as the average spectral signature of the different components of the model (Figure 3.7c). For each excitation, the sequence of species in the kinetic model is the simplest one that fits the 2DES amplitude as a function of the delay T . To determine the simplest model to describe the kinetics, the residual (the difference between data and the fitted values) across the spectrum is monitored to make sure the intensity is around zero. To describe the kinetic response of X3, the global model required five different spectrokinetic species (see kinetic scheme in Figure 3.7a). The character of these kinetic species is a combination of ground-state bleaching (GSB), stimulated emission (SE), and negative-going excited-state absorption (ESA). The first component is the response from the X3 exciton upon excitation. The EADS of this component has a positive GSB and SE signals at the excitation energy corresponding to the X3 exciton on the detection energy axis. Additionally, there is a positive signal at the energies of X1 and X2, this can be attributed to the shared ground state nature of all the excitations. The first two compartments rapidly evolve with time constant of 12 fs and 40 fs indicative of a coherent relaxation dynamics. This coherent relaxation process also contributes to a small increase in the intensity of GSB/SE amplitude at X1 and X2. Another notable event during this time frame is the shift and decrease of the ESA character at 1.85 eV. The ESA signal observed here is due to the formation of biexcitons of X3 with that of X1 (1.85 eV) and X2 (1.93 eV). The decrease in the ESA can be attributed to the overlapping SE signal produced during the relaxation of X3 to X1 and X2. The third spectrokinetic component evolves with a time constant of 200 fs. A significant decrease in the positive EADS amplitude at X3 energy is observed and at the same time there is increase in the

amplitude of at X1 and X2. The evolution of the third component to the fourth component is due to the hot electron cooling from the $1P_e$ electronic state to the $1S_e$ electronic state in an electron-hole picture of the QDs.^{6,9} It should be noted that excitons X1 and X2 have the same electronic energy level, $1S_e$. Therefore, when the electron relaxes from $1P_e$ to $1S_e$, the SE amplitude simultaneously increases at detection energies of both X1 and X2. The evolution of fourth species to fifth species has a time constant of 1.4 ps. In terms of EADS evolution, there is an increase in the ESA at about 2.0 eV as well as a decrease in X2 intensity. These intensity changes most likely indicate hole trapping on the surface of the QDs. The final component is the relaxation of the band-edge exciton to the ground state. This process is slow and takes several hundred picoseconds to complete.

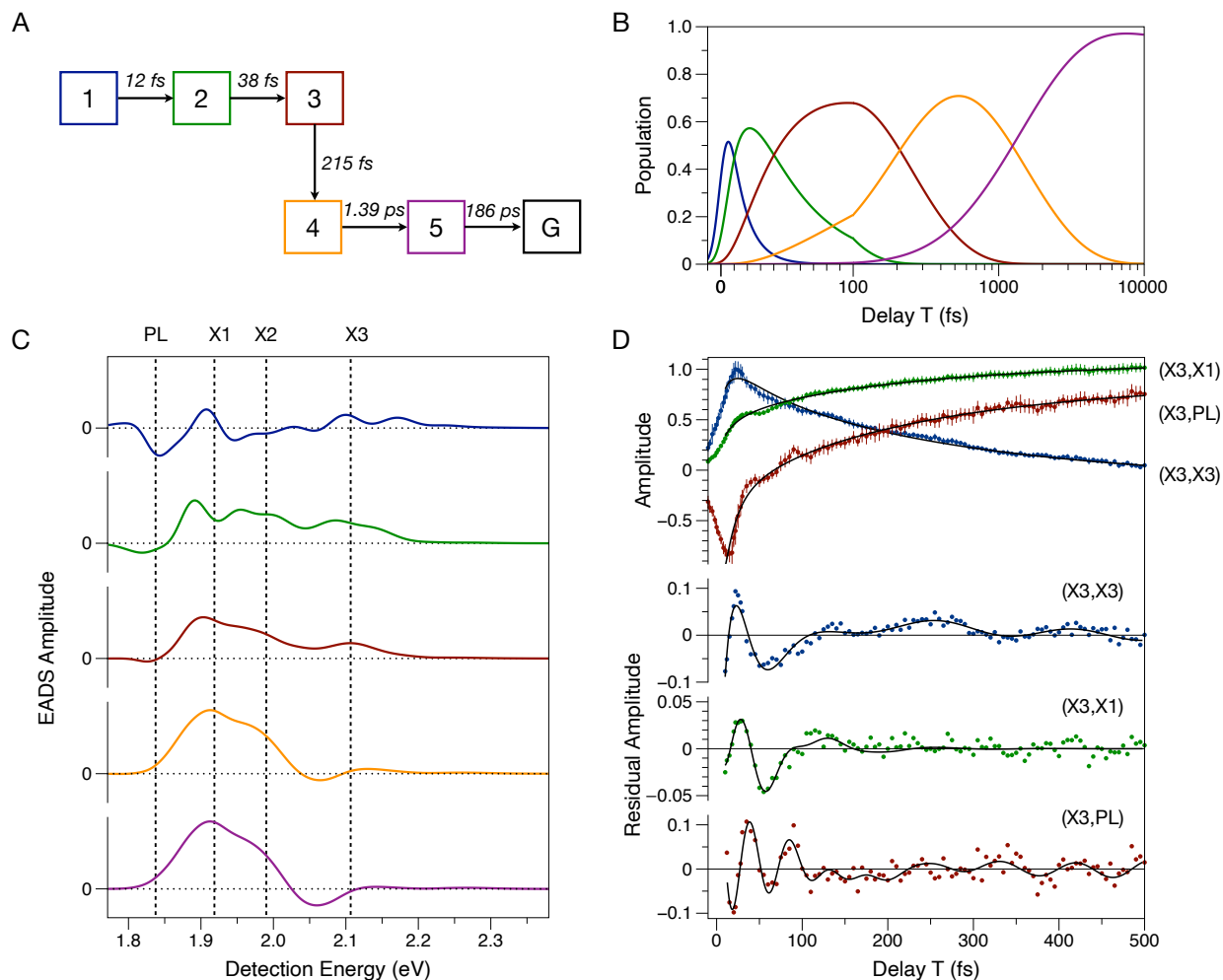


Figure 3.7. Global analysis of the population response of the X3 (2.066-2.194 eV) excitation region of 2DES spectrum of oleate capped CdSe quantum dots. (a) Kinetic scheme for the global model with time constants, 12 ± 1 fs, 40 ± 1 fs, 212 ± 3 fs, 1.41 ± 0.47 ps, and 186 ± 40 ps for each relaxation pathway. (b) Evolution of population with respect to time for each compartment. (c) Evolution associated difference spectra (EADS) for each compartment in the kinetic scheme. (d) Transients at various coordinates, (X3, X3) (blue trace), (X3, X1) (green trace) and (X3, PL) (maroon trace). The lower panels show the residual for each coordinate overlapped with the fit obtained from the LPSVD analysis.

The amplitude vs population time delay at different coordinates in the 2D spectra are plotted to show the population dynamics (Figure 3.7d). The blue trace is extracted at (X3, X3) which shows the population relaxation after the optical preparation of the X3 state. The green transient (X3, X1) and the maroon (X3, PL) show the transients at coordinates excited at X3 and detected at lower energy levels. The signal amplitude at these coordinates rises as the population from X3 relaxes to the X1 and PL energy levels.

The population relaxation in the signal response is accompanied by rapidly and slowly damped modulations. The rapidly damped modulations have damping times ~ 50 fs and frequencies derived from oleate-ligand vibrational motions. To characterize these rapidly damped modulations, an excitation-specific coherence map (Figure 3.8a) was generated by performing the FFT of residuals in the time range (10-200 fs). In this excitation specific coherence map, the amplitude of the FFT at each coordinate is plotted with frequency on the x-axis and detection energy on the y-axis. These maps encompass all the frequency information of the coherent dynamics at a given excitation energy. In the case of oleate-capped CdSe QDs, the coherence map reveals prominent modulations occurring across several lower energy levels, with the most significant intensities observed at X2, X1, and PL energy levels. This suggests that, upon excitation from the ground state, the coherent wavepacket persists during the relaxation process towards these lower energy levels.

The principal modulation components at the key coordinates, (X3, X3), (X3, X1) and (X3, PL) were analyzed using linear prediction, singular value decomposition (LPSVD) analysis (Figure 3.8b). The advantages of LPSVD over FTs include the additional information on the phase and the damping times of modulations. The data from 0-10 fs are

excluded from the analysis as to avoid any contributions from the pulse overlap effect in

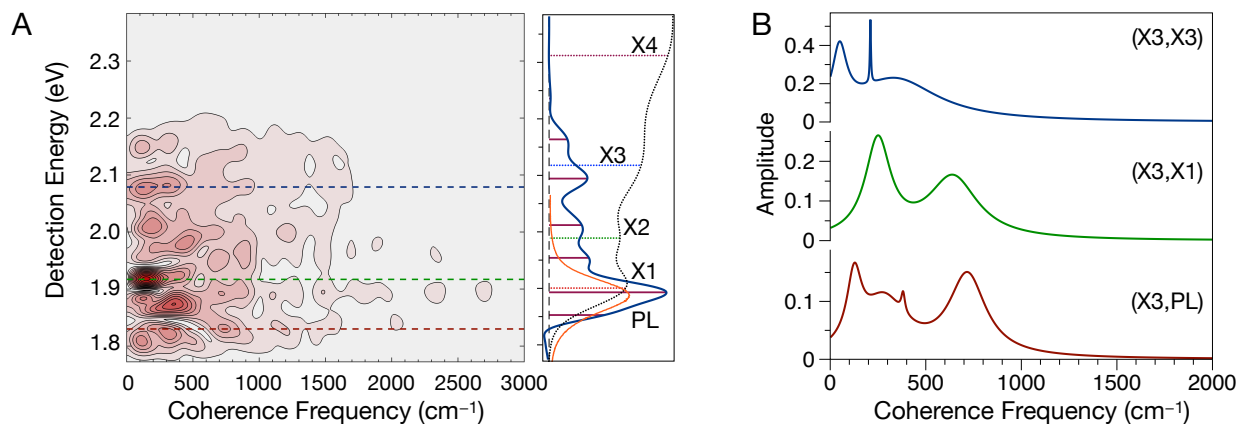


Figure 3.8. Coherence analysis accompanying the relaxation of X3. (a) Excitation-specific coherence map at X3 excitation (from 10-200 fs). The side panel includes the steady state absorption spectrum (b) LPSVD spectra for coordinates (X3, X3), (X3, X1) and (X3, PL) for time range 10- 500 fs.

the early time response. The LPSVD is carried out in the time range 10-500 fs to resolve both rapidly damped and slowly damped modulations simultaneously. The components of LPSVD analysis can be categorized to two, the low-frequencies, 0-300 cm^{-1} , and mid-frequencies in 300-700 cm^{-1} region. In the low frequency region, there are two types of modulation, rapidly damped and slowly damped modulations (Table 3.1). The example of slowly damped modulation is 210 cm^{-1} mode which aligns with the stimulated Raman signal due to the longitudinal optical (LO) phonon in a typical CdSe QD. Stimulated Raman coherence wavepackets dampen out in the vibrational dephasing times which are in the picosecond time domain. As a guide to understand the nature of these modulations, an electronic structure optimization and vibrational analysis of bidentate Cadmium oleate $[\text{Cd}(\text{C}_{18}\text{H}_{33}\text{O}_2)]^+$ is carried out using Gaussian software.³¹ The ground state optimization and the normal mode analysis were carried out using B3LYP functional 6-311g(d,p)/LANL2DZ level of theory.

Table 3.1. Parameters (frequency, amplitude, phase, and damping time) for LPSVD analysis of X3 excitation at the indicated coordinates in 2D spectra. These coordinates are indicated in the 2D spectra (Figure 3.6).

Coordinate	Frequency	Amplitude	Phase (radians)	Damping time
(X3, X3)	49 cm ⁻¹	0.72	2.76	117 fs
	210 cm ⁻¹	0.05	2.29	1616 fs
	339 cm ⁻¹	3.02	2.04	20 fs
(X3, X1)	250 cm ⁻¹	0.98	0.22	65 fs
	642 cm ⁻¹	1.23	4.12	34 fs
(X3, PL)	126 cm ⁻¹	0.26	0.89	116 fs
	280 cm ⁻¹	0.70	0.44	37 fs
	381 cm ⁻¹	0.02	1.27	455 fs
	718 cm ⁻¹	0.82	0.84	46 fs

To locate the amplitude of the vibrational motions in the given excitation and detection of the 2DES, a 3DES is produced. The entire signal response from a 2DES experiment is subjected to background exponential subtraction to isolate the residual. These residuals are the amplitudes of oscillations owing to different coherent wavepacket dynamics. The residual at each coordinate is subjected to FFT and to make a 3DES spectrum, the amplitude of a particular frequency at each coordinate is plotted with respect to the excitation and detection energies. The 3DES spectrum for 280 cm⁻¹, 380 cm⁻¹, 650 cm⁻¹ and 720 cm⁻¹ are shown in the Figure 3.9. The major intensity of the 3DES spectrum is seen along the relaxation pathway of the relaxation of X3 excitation. Another interesting feature is that the peaks are approximately spaced by the mode frequency along the detection

energy axis, which indicates that the peaks arise due to vibrational coherences.³² These observations indicate that the vibrational motions accompany the nonadiabatic relaxation of X3 exciton.

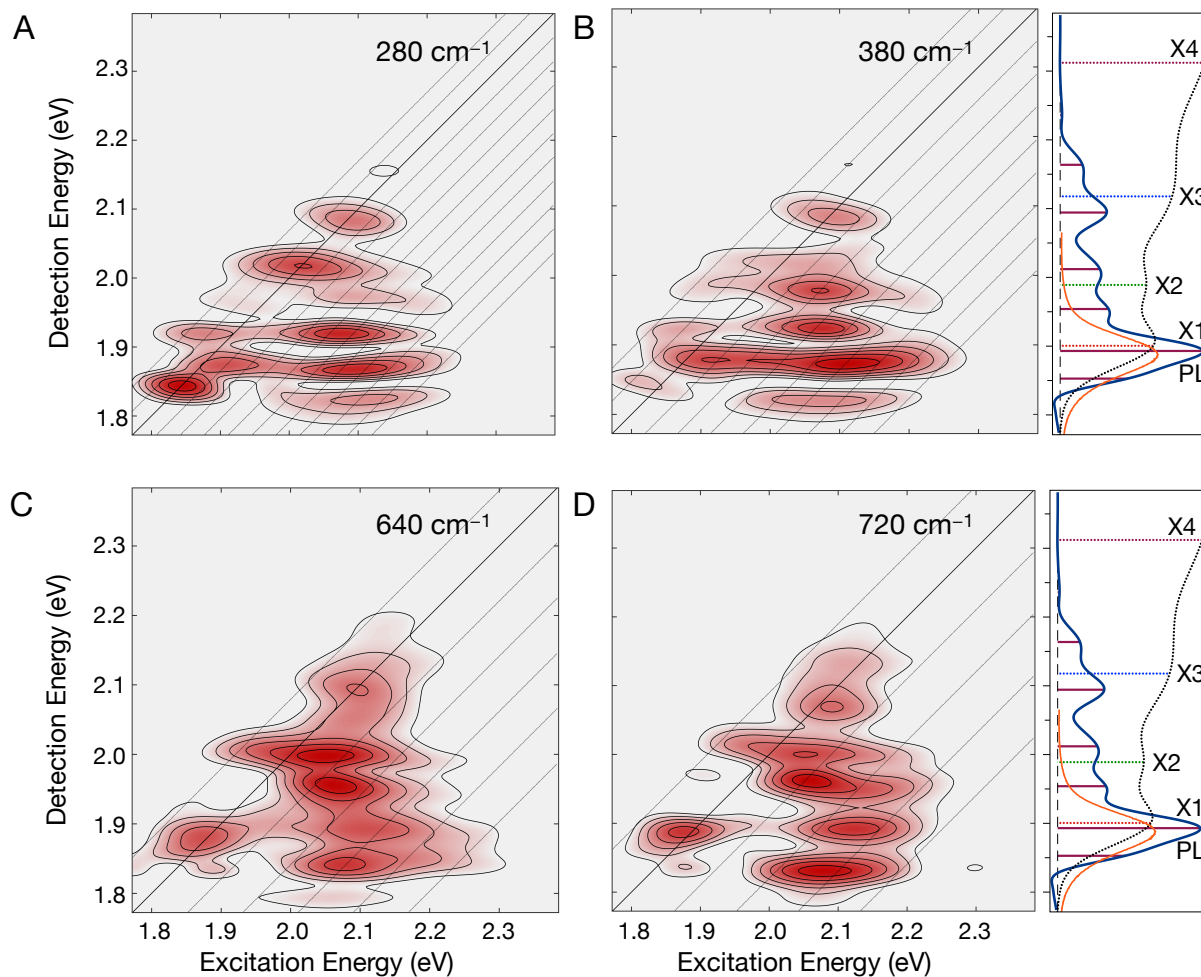


Figure 3.9. 3DES spectra/mode specific oscillation of modulations for rapidly damped modulations of frequencies, (a) 280 cm^{-1} , (b) 380 cm^{-1} , (c) 640 cm^{-1} , and (d) 720 cm^{-1} .

Global analysis was also performed on the X2 excitation (1.952-2.016 eV) to understand the relaxation mechanism (Figure 3.10). The X2 exciton has an excited hole in the valence band unlike the X3 with an excited electron in the conduction band. The relaxation of the X2 exciton can be visualized as relaxation of the excited hole to the band edge. An

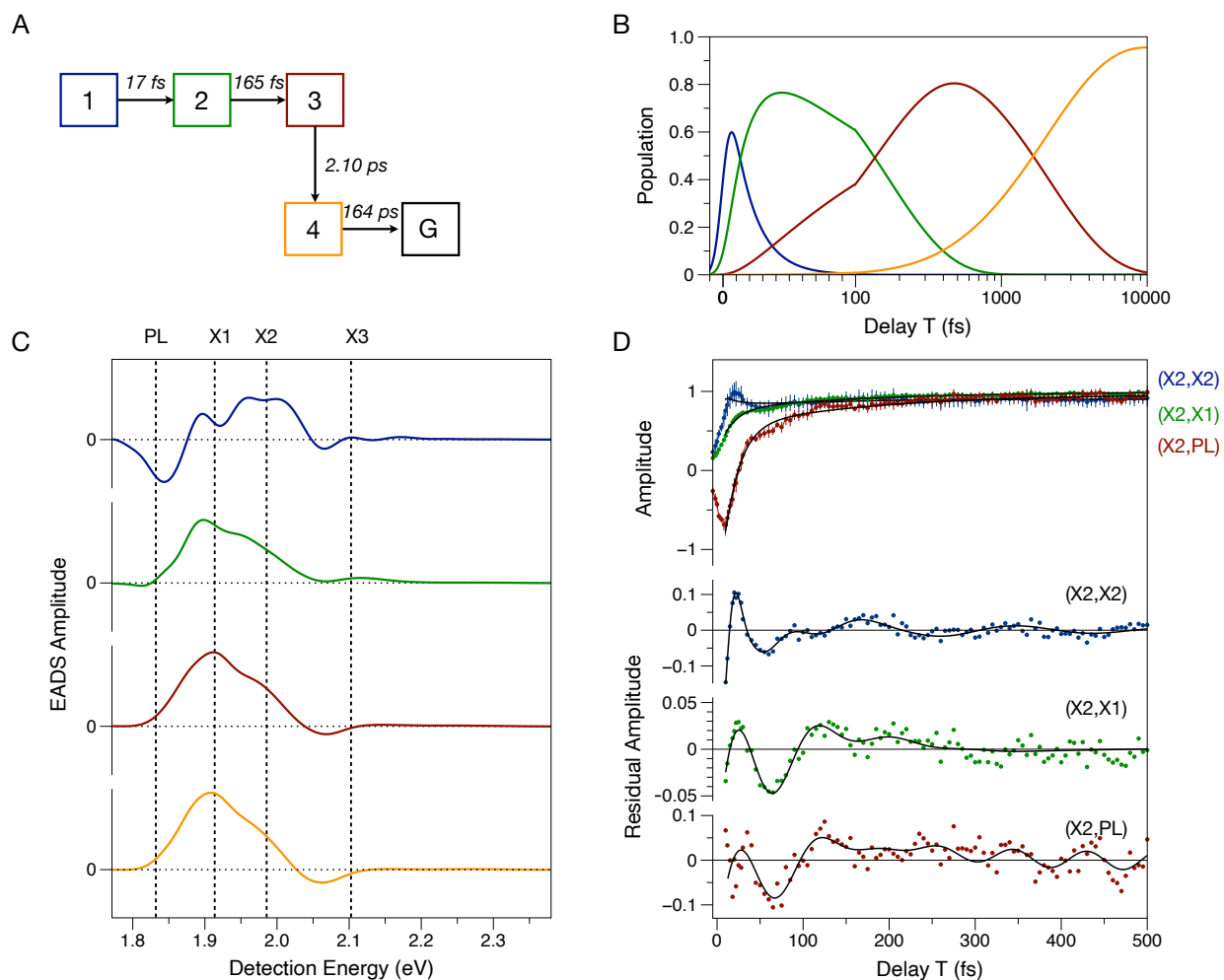


Figure 3.10. Global analysis of the population response of the X2 (1.952-2.016 eV) excitation region of 2DES spectrum of oleate capped CdSe quantum dots. (a) Kinetic scheme for the global model with time constants, 17 ± 1 fs, 165 ± 3 fs, 2.10 ± 0.4 ps, and 164 ± 40 ps for each relaxation pathway. (b) Evolution of population with respect to time for each compartment. (c) Evolution associated difference spectra (EADS) for each compartment in the kinetic scheme. (d) Transients at various coordinates, (X3, X3) (blue trace), (X3, X1) (green trace) and (X3, PL) (maroon trace). Lower panels show the residual for each coordinate overlapped with the fit obtained from the LPSVD analysis.

important point to keep in mind is that the transitions in QDs are very broad and the FWHM of the transition increases as with increase in energy of transition.²⁷ Due to the broad nature of these transitions, there could be some contribution from the X3 exciton at the X2 energy level as well. The global model requires four different spectrokinetic species to model the relaxation dynamics. The first component has GSB and SE signals at the excitation frequencies of X1 and X2 which are indicative of shared ground state. ESA signals

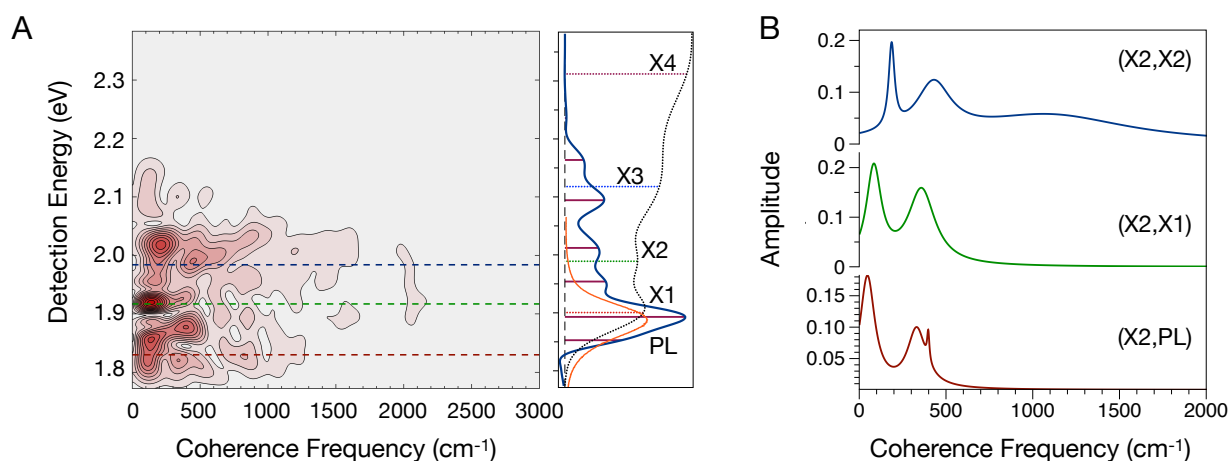


Figure 3.11. Coherence analysis accompanying the relaxation of X2. (a) Excitation specific coherence map at X3 excitation (from 10-200 fs). Side panel includes the steady state absorption spectrum (b) LPSVD spectra for coordinates (X2, X2), (X2, X1) and (X2, PL) for time range 10- 500 fs.

are observed at 1.85 eV and 2.05 eV which arises due to the biexciton formation of X2 with X1 and X3 respectively. This component undergoes decay with a time constant of 17 fs. During evolution, the ESA at energy levels 1.85 eV and 2.05 eV have disappeared. This is due to the overlap of SE arising due to the population relaxation to X1 energy level. The second component has a major GSB/SE intensity at the X1 and X2 excitation energies and decays with a time constant of 165 fs. As it evolves the X1 peak is shifted to higher energy.

The third component evolves with a time constant of 2.1 ps, the amplitude of the ESA at 2.05 eV increases owing to the surface traps (hole trap) on the QD. The final component relaxes in several hundreds of ps just like the final state in X3 excitation.

The excitation specific coherence for X2 excitation exhibits presence of coherences in the lower energy regions (Figure 3.11). Enhanced intensities are observed in the low frequencies and 400 cm^{-1} regions. The LPSVD analysis of the residuals at (X2, X2) and (X2, X1) shows that the modulation observed in the 400 cm^{-1} region is rapidly damped with damping times of ~ 50 fs. However, the LPSVD analysis of residual at (X2, PL) indicates that the 400 cm^{-1} vibrational mode is slowly damped and persist in the lowest energy region with a damping time ~ 650 fs. A comparison of the mode analysis between the X3 and X2 excitations are presented in the discussion section.

Table 3.2. Parameters for LPSVD analysis for X2 excitation at the indicated coordinates in 2D spectra. These coordinates are indicated in the excitation specific coherence map (Figure 3.11).

Coordinate	Frequency	Amplitude	Phase(radians)	Damping time
(X2, X2)	187 cm^{-1}	1.65	0.24	259 fs
	428 cm^{-1}	6.10	1.26	43 fs
	1094 cm^{-1}	15.59	1.07	9 fs
(X2, X1)	84 cm^{-1}	5.05	2.97	100 fs
	359 cm^{-1}	7.21	1.76	56 fs
(X2, PL)	47 cm^{-1}	0.26	0.89	101 fs
	331 cm^{-1}	0.70	0.44	82 fs
	398 cm^{-1}	0.02	1.27	670 fs

3.4 Discussion

The multidimensional spectroscopic study of coherent wavepacket dynamics upon optical preparation of excitons in oleate-capped CdSe quantum dots reveal that the vibrational motions that facilitate the nonadiabatic relaxation mechanism. The global model for the excitations shows rapid population relaxation (time constants <15 fs and <40 fs) indicative of coherent dynamics. This coherent wavepacket motions give rise to the rapidly damped modulations that accompany the exciton relaxation from higher energy levels. The short-time excitation specific coherence maps for X3 and X2 excitations exhibit low and mid-frequency vibrations in the lower energy levels. These modulations exhibit peak patterns that are similar to the vibrational coherences with major intensities below the diagonal and peaks spaced with respect to the frequency of vibrations.^{32,33}

The rapidly damped modulations like 130 cm^{-1} , 187 cm^{-1} and 280 cm^{-1} in the low frequency region arises due to the mixing of QD core modes with the vibrational modes of the ligands. This mixing of core vibrations with ligand vibrations gives rise to frequencies that are higher and lower than the lattice vibrations (eg. LO phonon). The modulations in the mid-frequency are assigned to the scissoring, rocking and wagging modes of the carboxylate group attached to the surface of the QD.³⁴ The mode analysis obtained from electronic structure calculations of Cd-oleate are shown in the Figure 3.12. The purple vectors depict the displacement of atoms from their equilibrium structures during the vibrational motions. The vibrational mode, $\sim 400\text{ cm}^{-1}$ involves rocking vibrations of the carboxylate attached to the Cd^{2+} along with rocking motions of CH_2 groups close to the carboxylates. This mode is rapidly damped in the excited state but persist for a long time in the lower energy PL state. This implies that the wavepacket rapidly slides down the

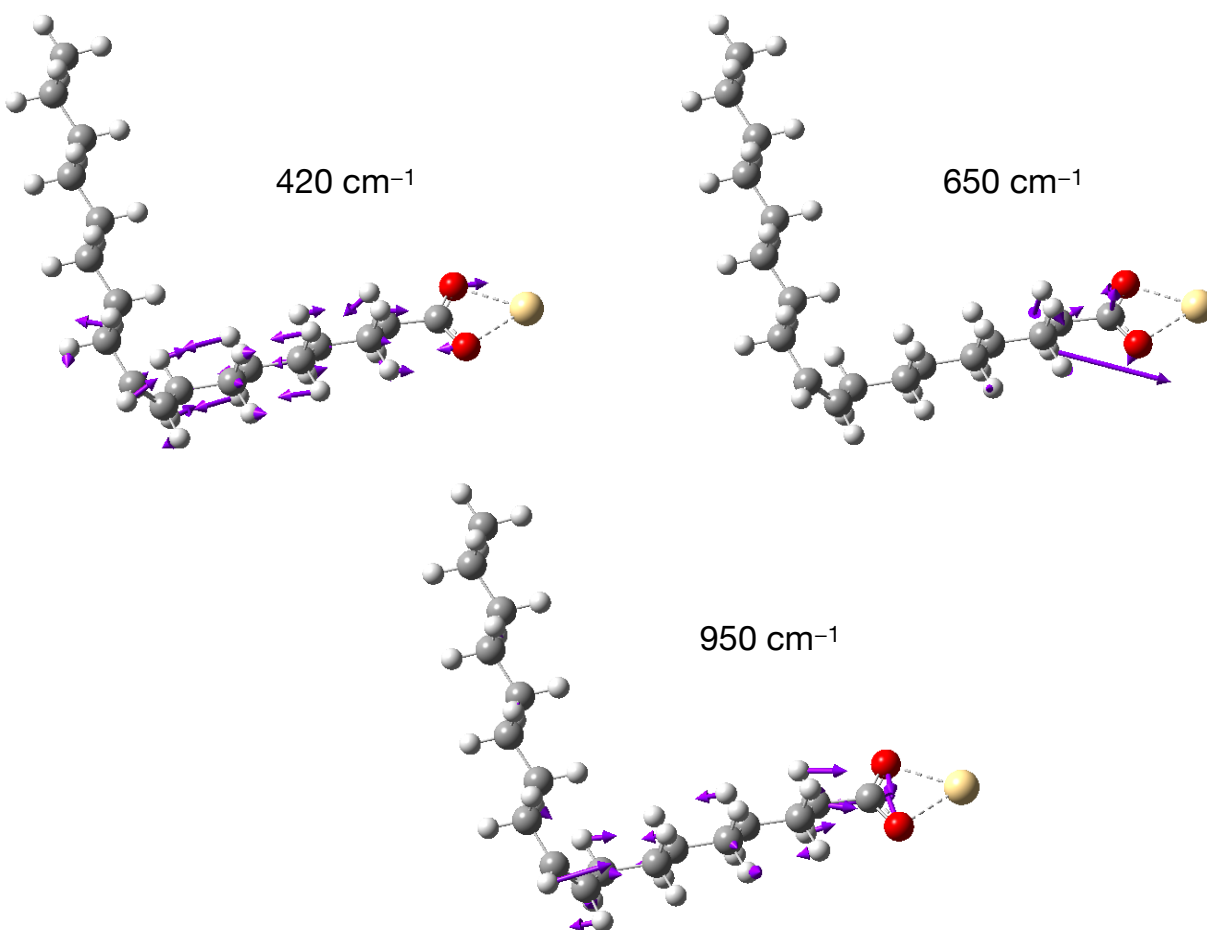


Figure 3.12. Vector representation of the 420 cm^{-1} , 650 cm^{-1} and 950 cm^{-1} obtained from the Raman spectra calculation of Cd oleate complex. Purple arrows indicate the direction of displacement of each atom from its equilibrium position.

cascade of conical intersections to reach the lower energy PL level and persists for a long time (670 fs). The 650 cm^{-1} mode involves out-of-plane stretching motions of the carboxylate bound to the Cd^{2+} ion and rocking motions of the adjacent atoms. Another mode observed in the calculation that is closer to the rapidly damped 1090 cm^{-1} mode seen at X2 is 950 cm^{-1} mode. This involves in-plane symmetric stretch of the carboxylate groups along with stretching motions of the carbon chain. Given the relatively high frequencies of these motions, it can be assessed that these vibrational motions are highly localized on the surface and to one ligand molecule. If there were multiple ligands aiding the relaxation

process simultaneously, the effective mass of the atoms involved in the vibrational motions would be very high. This would in turn result in very low frequency of the vibrations. The main difference in the rapidly damped modulations of the X3 and X2 excitation turns out to be the ligand-derived frequency. The relaxation of the X3 exciton essentially probes the relaxation of the electron from $1P_e$ level to $1S_e$. At the same time, X3 has an excited hole that relaxes to the band edge. The origin of the mid-frequency vibrational mode, 650 cm^{-1} observed in the X3 relaxation is due to the mixing of *electronic* wavefunction with the localized in-plane stretching of carboxylate moiety bound to the surface of the QD. Whereas the X2 excitation primarily probes the hole relaxation, and the 400 cm^{-1} is the vibrational mode that interacts with the *hole* wavefunction of the core QD. The fact that the 400 cm^{-1} mode is present in the X3 as well as X2 is the direct indication that this mode is mixed with the hole wavefunction. Another important aspect of the hole energy level is that they are very closely spaced. Therefore, it is easy to visualize the presence of 400 cm^{-1} mode in both X3 and X2 relaxation. This demonstrates the use of excitation specific coherence analysis to distinguish the vibrational motions that are mixed with the electronic wavefunction and the hole wavefunction. Access to excitation specific coherence analysis turns out to be a unique advantage of the 2DES performed with a broadband spectrum and short pulses.

The molecular exciton picture for the nonadiabatic relaxation includes a cascade of potential energy surfaces corresponding to different excitons. The optically prepared wavepacket slides via multiple potential energy surfaces and cross conical intersections (CIs) during exciton relaxation.^{15,35} Upon passage of the wavepacket via CIs, electronic energy is converted into vibrational motions along certain coordinates. The coherent wavepacket motions give rise to rapidly damped modulations with frequencies of surface-

ligand vibrational motions along the pathway of exciton relaxation. Surface ligand vibrations serve as branching modes and lifts the degeneracy of the potential energy surface crossings or conical intersections.¹⁴ The vibrational modes that undergo displacement during the nonadiabatic relaxation of the exciton in oleate-capped CdSe QDs are assigned to the low frequency modes with mixed core-ligand character and mid-frequency modes of the carboxylates bound to the surface. The ability to determine the effective electronic-vibrational coupling using ligand coherences will lead to new discoveries, especially in determining structural mechanisms for efficient excitation energy transfer or charge transfer to acceptors on the QD surface.

REFERENCES

- (1) García de Arquer, F. P.; Talapin, D. V.; Klimov, V. I.; Arakawa, Y.; Bayer, M.; Sargent, E. H. Semiconductor Quantum Dots: Technological Progress and Future Challenges. *Science* **2021**, *373* (6555). <https://doi.org/10.1126/science.aaz8541>.
- (2) Efros, A. L.; Brus, L. E. Nanocrystal Quantum Dots: From Discovery to Modern Development. *ACS Nano* **2021**, *15* (4), 6192–6210.
- (3) Bera, D.; Qian, L.; Tseng, T.-K.; Holloway, P. H. Quantum Dots and Their Multimodal Applications: A Review. *Materials* **2010**, *3* (4), 2260.
- (4) Alivisatos, P. The Use of Nanocrystals in Biological Detection. *Nat. Biotechnol.* **2004**, *22* (1), 47–52.
- (5) Kambhampati, P. Unraveling the Structure and Dynamics of Excitons in Semiconductor Quantum Dots. *Acc. Chem. Res.* **2011**, *44* (1), 1–13.
- (6) Klimov, V. I.; McBranch, D. W. Femtosecond P-to-S Electron Relaxation in Strongly Confined Semiconductor Nanocrystals. *Phys. Rev. Lett.* **1998**, *80* (18), 4028–4031.
- (7) Guyot-Sionnest, P.; Wehrenberg, B.; Yu, D. Intraband Relaxation in CdSe Nanocrystals and the Strong Influence of the Surface Ligands. *J. Chem. Phys.* **2005**, *123* (7), 074709.
- (8) Pandey, A.; Guyot-Sionnest, P. Slow Electron Cooling in Colloidal Quantum Dots. *Science* **2008**, *322* (5903), 929–932.
- (9) Kambhampati, P. Hot Exciton Relaxation Dynamics in Semiconductor Quantum Dots: Radiationless Transitions on the Nanoscale. *J. Phys. Chem. C* **2011**, *115* (45), 22089–22109.
- (10) Cooney, R. R.; Sewall, S. L.; Anderson, K. E. H.; Dias, E. A.; Kambhampati, P. Breaking the Phonon Bottleneck for Holes in Semiconductor Quantum Dots. *Phys. Rev. Lett.* **2007**, *98* (17), 177403.
- (11) Frederick, M. T.; Weiss, E. A. Relaxation of Exciton Confinement in CdSe Quantum Dots by Modification with a Conjugated Dithiocarbamate Ligand. *ACS Nano* **2010**, *4* (6), 3195–3200.
- (12) Frederick, M. T.; Amin, V. A.; Cass, L. C.; Weiss, E. A. A Molecule to Detect and Perturb the Confinement of Charge Carriers in Quantum Dots. *Nano Lett.* **2011**, *11* (12), 5455–5460.

- (13) Lian, S.; Christensen, J. A.; Kodaimati, M. S.; Rogers, C. R.; Wasielewski, M. R.; Weiss, E. A. Oxidation of a Molecule by the Biexcitonic State of a CdS Quantum Dot. *J. Phys. Chem. C* **2019**, *123* (10), 5923–5930.
- (14) Tilluck, R. W.; Mohan T M, N.; Hetherington, C. V.; Leslie, C. H.; Sil, S.; Frazier, J.; Zhang, M.; Levine, B. G.; Van Patten, P. G.; Beck, W. F. Vibronic Excitons and Conical Intersections in Semiconductor Quantum Dots. *J. Phys. Chem. Lett.* **2021**, *12* (39), 9677–9683.
- (15) Levine, B. G.; Martínez, T. J. Isomerization through Conical Intersections. *Annu. Rev. Phys. Chem.* **2007**, *58*, 613–634.
- (16) Jasieniak, J.; Bullen, C.; van Embden, J.; Mulvaney, P. Phosphine-Free Synthesis of CdSe Nanocrystals. *J. Phys. Chem. B* **2005**, *109* (44), 20665–20668.
- (17) Frazier, J.; Cavey, K.; Coil, S.; Hamo, H.; Zhang, M.; Van Patten, P. G. Rapid and Sensitive Identification and Discrimination of Bound/Unbound Ligands on Colloidal Nanocrystals via Direct Analysis in Real-Time Mass Spectrometry. *Langmuir* **2021**, *37* (50), 14703–14712.
- (18) Gurchiek, J. K.; Bao, H.; Domínguez-Martín, M. A.; McGovern, S. E.; Marquardt, C. E.; Roscioli, J. D.; Ghosh, S.; Kerfeld, C. A.; Beck, W. F. Fluorescence and Excited-State Conformational Dynamics of the Orange Carotenoid Protein. *J. Phys. Chem. B* **2018**, *122* (6), 1792–1800.
- (19) Shim, S.-H.; Zanni, M. T. How to Turn Your Pump-Probe Instrument into a Multidimensional Spectrometer: 2D IR and Vis Spectroscopies via Pulse Shaping. *Phys. Chem. Chem. Phys.* **2009**, *11* (5), 748–761.
- (20) Lozovoy, V. V.; Pastirk, I.; Dantus, M. Multiphoton Intrapulse Interference. IV. Ultrashort Laser Pulse Spectral Phase Characterization and Compensation. *Opt. Lett.* **2004**, *29* (7), 775–777.
- (21) DeLong, K. W.; Trebino, R.; Hunter, J.; White, W. E. Frequency-Resolved Optical Gating with the Use of Second-Harmonic Generation. *J. Opt. Soc. Am. B, JOSAB*. <https://doi.org/10.1364/JOSAB.11.002206>.
- (22) Augulis, R.; Zigmantas, D. Two-Dimensional Electronic Spectroscopy with Double Modulation Lock-in Detection: Enhancement of Sensitivity and Noise Resistance. *Opt. Express* **2011**, *19* (14), 13126–13133.
- (23) Wong, C. Y.; Scholes, G. D. Biexcitonic Fine Structure of CdSe Nanocrystals Probed by Polarization-Dependent Two-Dimensional Photon Echo Spectroscopy. *J. Phys. Chem. A* **2011**, *115* (16), 3797–3806.

- (24) Norris, D. J.; Efros, A. L.; Rosen, M.; Bawendi, M. G. Size Dependence of Exciton Fine Structure in CdSe Quantum Dots. *Phys. Rev. B Condens. Matter* **1996**, *53* (24), 16347–16354.
- (25) Harel, E.; Rupich, S. M.; Schaller, R. D.; Talapin, D. V.; Engel, G. S. Measurement of Electronic Splitting in PbS Quantum Dots by Two-Dimensional Nonlinear Spectroscopy. *Phys. Rev. B Condens. Matter* **2012**, *86* (7), 075412.
- (26) Collini, E.; Gattuso, H.; Levine, R. D.; Remacle, F. Ultrafast Fs Coherent Excitonic Dynamics in CdSe Quantum Dots Assemblies Addressed and Probed by 2D Electronic Spectroscopy. *J. Chem. Phys.* **2021**, *154* (1), 014301.
- (27) Caram, J. R.; Zheng, H.; Dahlberg, P. D.; Rolczynski, B. S.; Griffin, G. B.; Dolzhenkov, D. S.; Talapin, D. V.; Engel, G. S. Exploring Size and State Dynamics in CdSe Quantum Dots Using Two-Dimensional Electronic Spectroscopy. *J. Chem. Phys.* **2014**, *140* (8), 084701.
- (28) Seiler, H.; Palato, S.; Sonnichsen, C.; Baker, H.; Kambhampati, P. Seeing Multiexcitons through Sample Inhomogeneity: Band-Edge Biexciton Structure in CdSe Nanocrystals Revealed by Two-Dimensional Electronic Spectroscopy. *Nano Lett.* **2018**, *18* (5), 2999–3006.
- (29) Palato, S.; Seiler, H.; Baker, H.; Sonnichsen, C.; Brosseau, P.; Kambhampati, P. Investigating the Electronic Structure of Confined Multiexcitons with Nonlinear Spectroscopies. *J. Chem. Phys.* **2020**, *152* (10), 104710.
- (30) van Stokkum, I. H. M.; Larsen, D. S.; van Grondelle, R. Global and Target Analysis of Time-Resolved Spectra. *Biochim. Biophys. Acta* **2004**, *1657* (2–3), 82–104.
- (31) Frisch, M. J.; Trucks, G. W.; Schlegel, H. B.; Scuseria, G. E.; Robb, M. A.; Cheeseman, J. R.; Scalmani, G.; Barone, V.; Petersson, G. A.; Nakatsuji, H.; Li, X.; Caricato, M.; Marenich, A. V.; Bloino, J.; Janesko, B. G.; Gomperts, R.; Mennucci, B.; Hratchian, H. P.; Ortiz, J. V.; Izmaylov, A. F.; Sonnenberg, J. L.; Williams; Ding, F.; Lipparini, F.; Egidi, F.; Goings, J.; Peng, B.; Petrone, A.; Henderson, T.; Ranasinghe, D.; Zakrzewski, V. G.; Gao, J.; Rega, N.; Zheng, G.; Liang, W.; Hada, M.; Ehara, M.; Toyota, K.; Fukuda, R.; Hasegawa, J.; Ishida, M.; Nakajima, T.; Honda, Y.; Kitao, O.; Nakai, H.; Vreven, T.; Throssell, K.; Montgomery, J. A., Jr.; Peralta, J. E.; Ogliaro, F.; Bearpark, M. J.; Heyd, J. J.; Brothers, E. N.; Kudin, K. N.; Staroverov, V. N.; Keith, T. A.; Kobayashi, R.; Normand, J.; Raghavachari, K.; Rendell, A. P.; Burant, J. C.; Iyengar, S. S.; Tomasi, J.; Cossi, M.; Millam, J. M.; Klene, M.; Adamo, C.; Cammi, R.; Ochterski, J. W.; Martin, R. L.; Morokuma, K.; Farkas, O.; Foresman, J. B.; Fox, D. J. *Gaussian 16 Rev. C.01*; Wallingford, CT, 2016.
- (32) Butkus, V.; Zigmantas, D.; Valkunas, L.; Abramavicius, D. Vibrational vs. Electronic Coherences in 2D Spectrum of Molecular Systems. *Chem. Phys. Lett.* **2012**, *545*, 40–43.

- (33) H. L.; Abramavicius, D.; Zigmantas, D. Discrimination of Diverse Coherences Allows Identification of Electronic Transitions of a Molecular Nanoring. *J. Phys. Chem. Lett.* **2017**, *8* (10), 2344–2349.
- (34) Wong, P. T. T.; Mantsch, H. H. Temperature-Induced Phase Transition and Structural Changes in Micellar Solutions of Sodium Oleate Observed by Raman Scattering. *J. Phys. Chem.* **1983**, *87* (13), 2436–2443.
- (35) Domcke, W.; Yarkony, D. R.; Köppel, H. *Conical Intersections*.
<https://www.worldscientific.com/worldscibooks/10.1142/7803> (accessed 2023-10-15)

APPENDIX

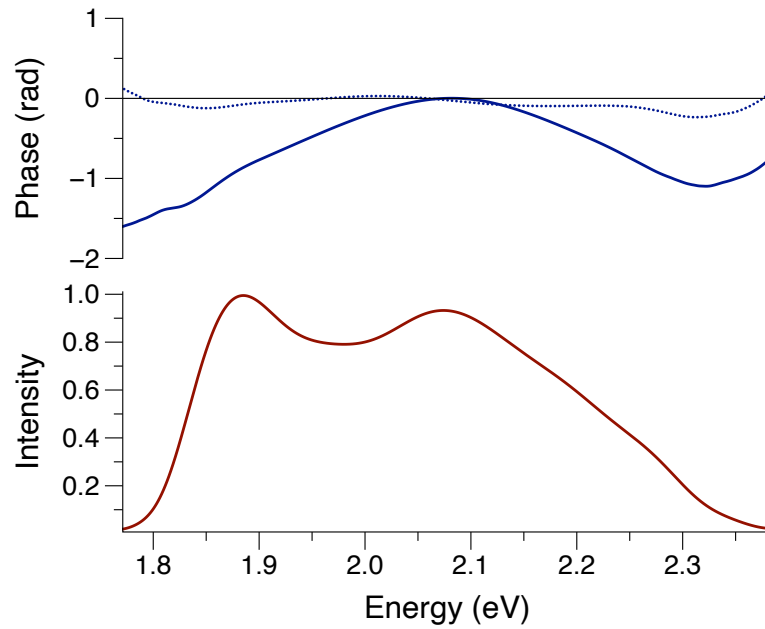


Figure A3.1. Residual phase and intensity spectra of the femtosecond laser pulses used in the broadband multidimensional electronic spectroscopy experiments. Top panel shows residual phase spectra after compression of the laser pulses used in the 2DES experiment for the pump beam (solid), and for the probe beam (dashed), as determined by MIIPS scans.²⁰ Bottom panel is the intensity spectrum of the laser pulses.

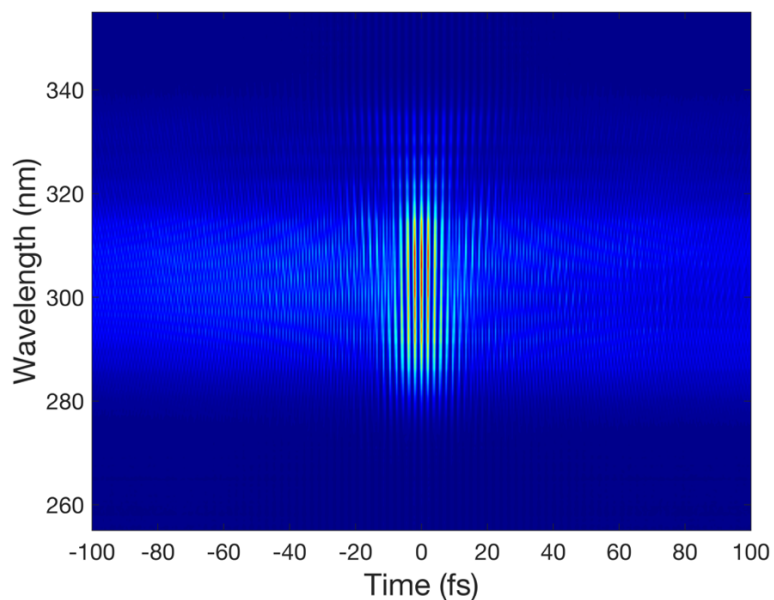


Figure A3.2. SHG-FROG²¹ spectrogram for the pump pulses, as measured with scanned pulse pairs prepared by the pump beam's pulse shaper in the 2DES spectrometer.

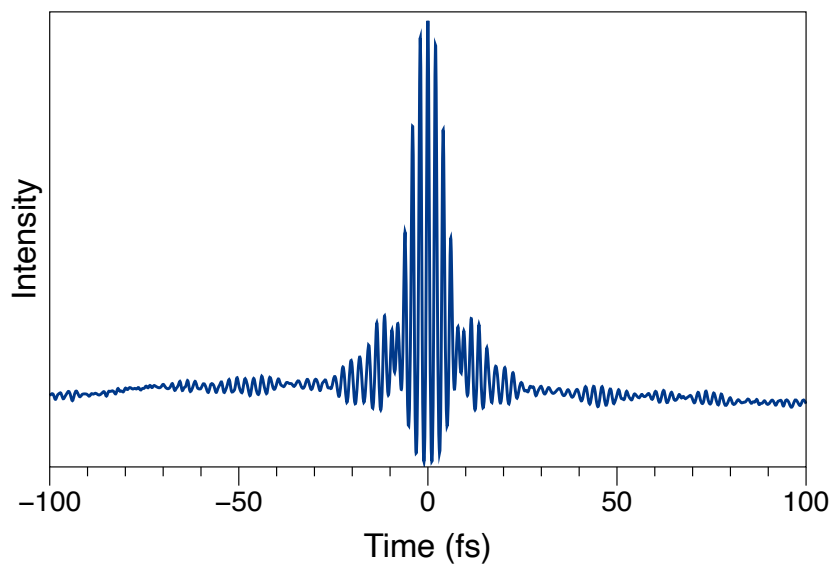


Figure A3.3. Interferometric autocorrelation of the pump pulses, determined as the integral of the SHG-FROG spectrogram (Figure A3.2).

Chapter 4: Vibronic Coherences Initiate Photoinduced Charge Transfer from CdSe Quantum Dots to Methyl Viologen

We studied the role of vibronic coherences in photoinduced charge transfer of CdSe quantum dots (QDs) in the presence of surface-bound methyl viologen dication (MV^{2+}) acceptors using multidimensional spectroscopy with broadband (500–700 nm) mid-visible excitation pulses of <7 fs duration. Analysis of coherent wavepacket motions in two-dimensional electronic spectra of oleate-capped CdSe QDs treated with MV^{2+} reveal enhanced activity in low and mid-frequency vibrations at frequencies corresponding to core lattice vibrations and out-of-plane deformations of the MV^{2+} pyridine rings. The rapid damping of these coherences is consistent with their assignment to excited-state coherent wavepacket motions following hot-carrier cooling. They can be distinguished from slowly damped stimulated Raman pathways involving the core longitudinal optical phonon modes. We assign the excited-state wavepacket motions to a charge-transfer state of mixed QD and MV^{2+} character, which is populated in <200 fs prior to transfer of a valence band electron to the MV^{2+} acceptor on the ps timescale. These observations are potentially significant steps towards understanding how to use coherences focused on the organic ligands and adsorbed electron- and excitation-energy acceptors on the surface of QDs to optimize their use in photocatalysis.

4.1 Introduction

Solar light harvesting offers a promising solution to overcome current energy challenges, particularly the extensive use of nonrenewable fossil fuels.¹ Semiconductor nanocrystalline materials are great potential candidates as light-harvesting materials due to their tunable size, optical and redox properties.^{2,3} In particular, colloidal quantum dots (QDs) capped with various surface ligands are used in several classes of solution-processed optoelectronic devices such as photovoltaic cells,⁴ emissive devices,^{5,6} and photodetectors.⁷ Furthermore, photocatalysis using QDs is another promising application that can utilize the solar energy to drive chemical reactions.^{8,9}

The process of solar light harvesting involves the absorption of photons and the subsequent generation of electron-hole (*e-h*) pairs. The excellent tunable optical properties of the QDs can be used to absorb photons in a wide range of energies to generate *e-h* pairs. Successful implementation of QDs in solar light harvesting relies on extracting charge carriers and stabilizing the charge-separated state. The charge separation in photoexcited QDs are achieved using electron or hole acceptors (Figure 4.1). These acceptor species can then be utilized for various applications, such as catalyzing redox reactions and facilitating charge transport. The chemistry of the QD surface and the nature of surface ligands can be tuned to achieve efficient extraction of photogenerated charge carriers and stabilization of charge separated state.¹⁰⁻¹²

One of the most interesting ligand candidates for such a charge transfer (CT) are viologens (V), a class of cationic organic molecules with conjugated bi-pyridyl functional groups with three stable forms: dication, radical cation, and neutral molecule. The dication viologen molecule, V^{2+} , can be sequentially reduced to stable radical cation and neutral

molecule. They have been widely used as an electron acceptor for charge separation from the photoexcited quantum dots.¹³⁻¹⁵ Methyl viologen dichloride or 1,1'-Dimethyl-4,4'-bipyridinium dichloride, is an electrochromic molecule. The dication species of the methyl viologen has a spectroscopic signature in the UV region, whereas the reduced form of the molecule, the methyl viologen radical, has a distinct spectroscopic signature in the visible region (Figure 4.2). Therefore, in the event of electron transfer from the QDs, radical cation is formed, and it can be detected using a visible probe. The Weiss group have studied the photoinduced CT using viologen derivatives and the mechanism of surface ligand adsorption in CdSe and CdS quantum dot systems using transient absorption experiments.¹⁵⁻¹⁸ The Lian group have demonstrated varying range of CT rates with respect to several functionalized viologen electron acceptor molecules.¹⁹ The Smith group has investigated the electron transfers in CdSe/CdS core-shell quantum systems using viologen acceptors and demonstrated that the charge transfer rates decrease with increase in the shell thickness.²⁰

Additionally, there have been several reports on the involvement of vibrational coherences in the CT processes from QDs to various electron acceptors.^{21,22} The Zhu group has carried out hot electron extraction from PbSe QDs using TiO₂ electron acceptors and observed vibrational coherences involving the surface atoms of the electron acceptor TiO₂.²¹ Vibrational coherences in this study arises when optical pulses shorter than the vibrational period activate electric fields near the surface. Recently, the Scholes group have investigated the mechanism of ultrafast electron transfer in polymer-fullerene blends using vibrational coherences.²²

In this chapter, we present the photoinduced CT from CdSe QD to the surface bound electron acceptor molecule, methyl viologen (MV). The CT from a donor to acceptor requires good energy level alignment of donor-acceptor states with donor state at similar or higher energy than that of the acceptor state and a good wavefunction overlap between the donor and acceptor wavefunction. In the QD-MV²⁺ presented here, the lowest electronic energy level of CdSe is the donor state while the lowest unoccupied molecular orbital (LUMO) is the electron acceptor. We propose that the orbital overlap of the donor and acceptor states lead to mixing of electronic states of QDs with vibrational states of the MV²⁺. This mixing lead to delocalization of the surface and formation of vibronic excitons. This delocalized intermediate formed between QD core and MV²⁺ initiates the photoinduced CT from QD core to surface ligand electron-acceptor. From the Chapter 3, we learnt how the vibronic coherences involving surface ligands mediated the exciton relaxation in oleate-capped CdSe QDs. Here, the electronic-vibrational coupling using ligand coherences will be extended to understand the structural and coherent mechanisms for efficient photoinduced charge transfer to acceptors on the QD surface.

In this chapter, we discuss the use of broadband two-dimensional electronic spectroscopy (2DES) to study the kinetics and detect the vibronic coherences that mediate photoinduced charge transfer from CdSe QDs to the MV²⁺. The 2DES enables us to detect the exciton specific electron transfer to MV²⁺ as the radical cation exhibits a photoinduced absorption in the visible region.^{15,19} The short-pulses allows us to detect the vibronic coherences before their dephasing times. The global analysis used to model the kinetics of electron transfer from QD core to the MV²⁺ shows that the electron transfer occurs from the

lowest electronic energy level (either X1 or X2) of the QD to the LUMO of MV^{2+} . The coherence analysis of the modulations using LPSVD models and excitation specific

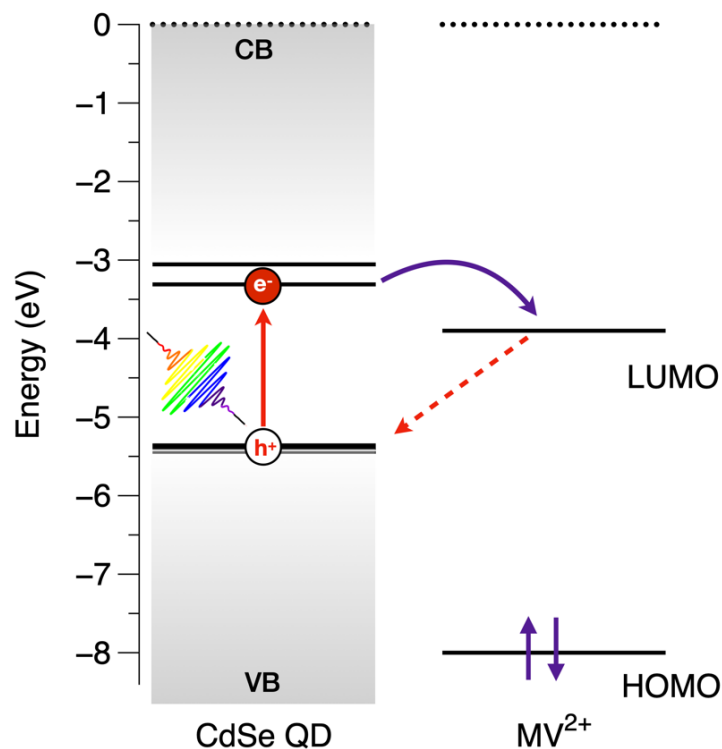


Figure 4.1. Energy level diagram for the photoinduced electron transfer from CdSe QD core to methyl viologen dication (MV^{2+}) inspired by Morris-Cohen et al.¹⁵ On the left, the electron ($1S_e$ and $1P_e$) and hole energy levels of the QDs are marked with solid lines. The conduction band (CB) and valence band (VB) of the QDs are marked with shaded regions. Exciton formation upon optical pulse interaction is indicated by the red arrow. On the right side, the lowest unoccupied molecular orbital (LUMO) and highest occupied molecular orbital (HOMO) levels of MV^{2+} are shown. Upon photoexcitation, an electron-hole pair is formed in the QDs. This electron is transferred from the $1S_e$ state of the QD to the LUMO of the MV^{2+} . The dotted arrow represents the electron recombination from the $MV^{••}$ to the hole in the VB.

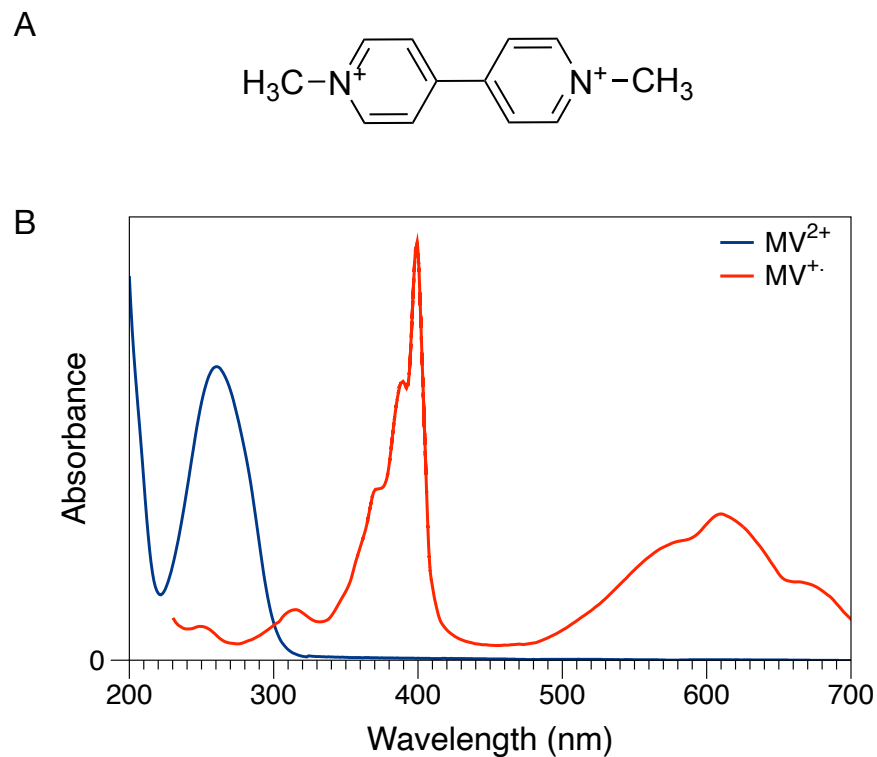


Figure 4.2. Spectroscopic characterization of methyl viologen. (a) Structure of 1,1'-dimethyl-4,4'-bipyridinium dication. (b) Absorption spectra at 298 K and of methyl viologen dication (blue trace) and radical cation in ethanol (red trace, redrawn from Watanabe et al.²³).

coherence map shows an enhanced activity in the low and mid-frequency vibrational modes. These vibrations correspond to the mixed core lattice vibrations of CdSe QD and out-of-plane deformations of the pyridine rings of MV^{2+} and arise from a mixed intermediate charge-transfer state involving the core of the QD and MV^{2+} .

4.2 Experimental Methods

4.2.1 CdSe Quantum Dot Synthesis and Characterization

The 2DES studies on CdSe quantum dots presented in this chapter were synthesized by the Van Patten laboratory at MTSU. The detailed procedure for QD synthesis is presented in Chapter 3 of this thesis. In short, CdSe QDs were synthesized following a modified

phosphine-free synthesis previously reported by Jasieniak et al.²⁴ A Se precursor stock solution was prepared in octadecene (ODE) for 30 min and then heated under nitrogen at 200°C for 2 h. A separate stock solution of Cd-oleate was prepared by dissolving CdO in oleic acid and heated under nitrogen at 100 °C for 1 h. The Cd-oleate solution was then heated to 285 °C, and the Se precursor was rapidly injected. The growth temperature was maintained at 265 °C for 30 min. After the first growth step, UV/Vis measurements were taken using a modernized Cary 14 spectrophotometer, and a second injection of the Se precursor was performed and the QD solution was allowed to grow at 265 °C for another 30 mins. The resulting QD solution was purified by two cycles of precipitation by spinning in a microcentrifuge at 17000 × g and resuspension using a chloroform/acetone/nitrile solvent/antisolvent combination. The surface ligands of the QDs were analyzed using TD-DART-MS as previously described by Frazier *et al.*²⁵

4.2.2 Linear Spectroscopy and Photoluminescence

The QDs were dispersed in chloroform to obtain an absorbance of 0.3 at 565 nm for the 2DES experiments. The chloroform solution is well miscible with the MV²⁺ in methanol and prevents the aggregation of QD-MV²⁺ complex. The absorption spectra were measured using a Shimadzu-2600 UV-Vis-NIR spectrophotometer. The room temperature photoluminescence (PL) was measured using Hitachi F-4500 Fluorescence Spectrophotometer. A 4 mM stock solution of methyl viologen dichloride hydrate (purchased from Sigma-Aldrich) was prepared in methanol. A control experiment was performed using oleate-capped CdSe QDs. To prepare the QD-MV²⁺ complex, 5.6 μL of the MV²⁺ stock solution was added to 150 μL of the QD sample to obtain a 1:50 ratio of the QD:MV²⁺.

4.2.3 Two-Dimensional Electronic Spectroscopy

2DES spectra were recorded using a pump–probe optical configuration with adaptive pulse shaping²⁶ to compress the laser pulses and to generate the excitation pulse sequence (pulse 1– τ –pulse 2) required for the three-pulse stimulated photon-echo experiment. Excitation pulses were obtained from a noncollinear optical parametric amplifier (NOPA, Spectra-Physics Spirit-NOPA-3H), which was pumped by the third harmonic of a 1.04 μm amplified Yb laser (Spectra-Physics Spirit-4W, 400 fs pulses at a 100 kHz repetition rate, 4 W average power). The pump and probe beams in the spectrometer were split from the NOPA output by a broadband dielectric beamsplitter (Layertec, Mellingen), processed by an adaptive pulse shaper (FemtoJock and FemtoJock P, respectively, Biophotonic Solutions), and then compressed by multiple reflections on pairs of broadband chirped mirrors (Ultrafast Innovations, Munich). For the present experiments, the NOPA's signal beam output spectrum (Figure 4.3b) was centered at 600 nm (~ 110 nm FWHM; 520–700 nm usable range). The excitation pulse energy was attenuated to 3.75 nJ per pulse, as measured at the sample's position. The pump beam's plane of linear polarization was rotated magic angle (54.7°) from that of the probe beam by a thin achromatic half-wave retarder plate. The two beams were focused by off-axis parabolic mirrors to 100 μm spots overlapped spatially just after the front window of the sample cuvette. The excitation pulses in both beams were characterized by MIIPS scans²⁷ conducted with a thin β -barium borate crystal, which was placed at the sample's position following a single cuvette window. The estimated pulse duration for both beams at the sample position was 7 fs. Residual phase plots (Figures A4.1), SHG-FROG spectrograms²⁸ (Figure A4.2), and autocorrelation (Figure A4.3) are presented in the appendix.

2DES spectra were recorded by programming the pump beam's pulse shaper to scan the coherence time interval between the two pump pulses, τ , from 0 to 50 fs with 0.5 fs steps to obtain the excitation axis after Fourier transformation. The detection axis of the 2DES spectrum was measured directly by measuring the pump-induced change in probe transmission through the sample with a home-built 0.2 m spectrograph (300 gr/mm diffraction grating) and a fast CCD detector (Andor Newton 940) using a phase-sensitive detection protocol and amplitude modulation of the pump pulses.²⁹ The population time T is scanned by a time-of-flight delay stages with a spacing of 2.5 fs from 0-20 fs, 5 fs spacing from 30-400 fs, 10 fs spacing from 400-800 fs, 100 fs spacing from 800-1000 fs, 1 ps spacing from 1-10 ps, and 10 ps from 10-150 ps. Each 2D spectrum was an average of four consecutive T scans. The signals detected in the 2DES in the pump-probe configuration were a sum of rephasing and non-rephasing responses from the sample.

4.3 Results

4.3.1 Linear Absorption and Photoluminescence

To study the vibronic mechanism of the photoinduced charge transfer in the QD-MV²⁺ complex, oleate-capped CdSe QDs with a size of ~6.5 nm were used to perform the 2DES experiment. Upon incidence of photons, electrons are excited from the hole states in the valence band to the electronic states in the conduction band. In the 6.5-nm CdSe QDs, the lowest energy transition or the band edge exciton ($1S_{3/2}1S_e$) is denoted as X1 at 1.94 eV, the second exciton ($2S_{3/2}1S_e$) is denoted as X2 at 2.04 eV, and the third exciton ($1P_{3/2}1P_e$) as X3 at 2.2 eV. Figure 4.3a shows the various excitons created upon photoexcitation within the CdSe QDs, illustrating their positions in both the electron-hole energy level and the exciton

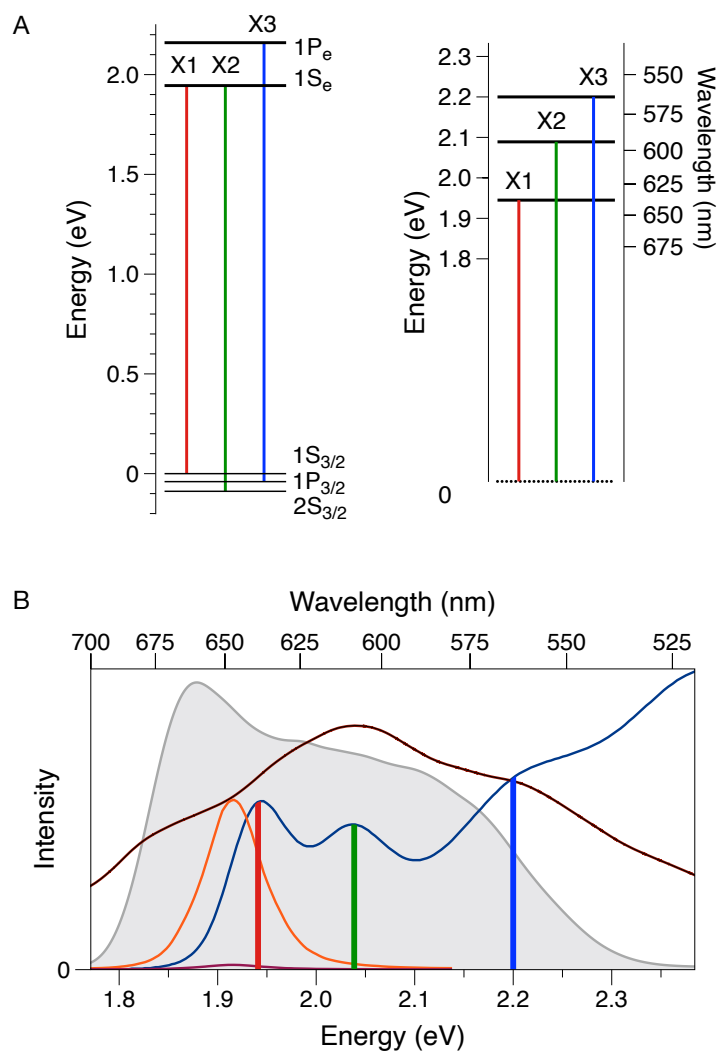


Figure 4.3. Energy level diagram of CdSe QDs and steady-state spectroscopic characterization of QD- MV^{2+} . (a) On the top left, the electron-hole energy levels are marked with hole levels in the valence band and electron levels in the conduction band. The vertical lines depict different excitons: X1 (red), X2 (green), and X3 (blue). The figure on the right shows the exciton energy levels with energy in eV on the left and wavelength on the right. (b) Linear absorption spectrum (blue trace) marked exciton energy levels, and photoluminescence (PL) spectrum (orange trace) with overlapping laser spectrum (gray filled). The brown trace is the photoinduced absorption spectrum of $MV^{\bullet+}$ radical cation adapted from Zhao et al.¹⁹ The purple trace is the PL of the QD- MV^{2+} complex.

energy domain. These distinct excitons are represented by different colors (X1-red, X2-green, and X3-blue) in the absorption spectrum (Figure 4.3b). The peak positions were determined using the minima of second derivative of the absorption spectrum. The PL peak

maximum was observed at 1.917 eV. The CdSe QDs presented in this study are smaller than the QDs in the Chapter 3. Therefore, the absorption spectrum of these particles is blue shifted. The smaller particles were chosen for the experiment to decrease the overlap of QD signals with that of $MV^{+\bullet}$ and to detect the photoinduced absorption signal from the $MV^{+\bullet}$.

The absorption spectrum of the QD- MV^{2+} complex exhibits the same profile as that of the QDs in the visible region as MV^{2+} does not absorb in this region (Figure 4.2b). However, the PL from the QDs was quenched after formation of the QD- MV^{2+} complex (Figure 4.3b, purple trace). This is due to the transfer of electron from the QD core to the MV^{2+} ligand which limits the radiative recombination of the e-h in the QD. The broadband laser spectrum spanned the first three excitons very well in this study. The coverage of the broadband spectrum allows us to study the population relaxation and coherent wavepacket dynamics from all three exciton levels and the photoinduced charge transfer to MV^{2+} by simultaneously detecting the $MV^{+\bullet}$ radical cation.

4.3.2 Two-Dimensional Electronic Spectroscopy

A series of 2D spectra at different time delays, T are shown in the Figure 4.4. The left side of the figure shows the 2D spectrum acquired at the labeled time delays from the 2DES control experiments with oleate-capped QDs. The 2D spectra obtained from the QD- MV^{2+} complex is shown on the right. The side panel includes the absorption spectrum of the QDs with marked exciton energy levels, the laser spectrum, and the photoinduced absorption spectrum of the $MV^{+\bullet}$. In the short time delay, the 2D spectra exhibit partially resolved positive peaks along the diagonal resulting from the ground state bleaching (GSB) and stimulated emission (SE). The formation of diagonal peaks indicates the preparation of population at different exciton energy levels after the excitation from the pump pulses.

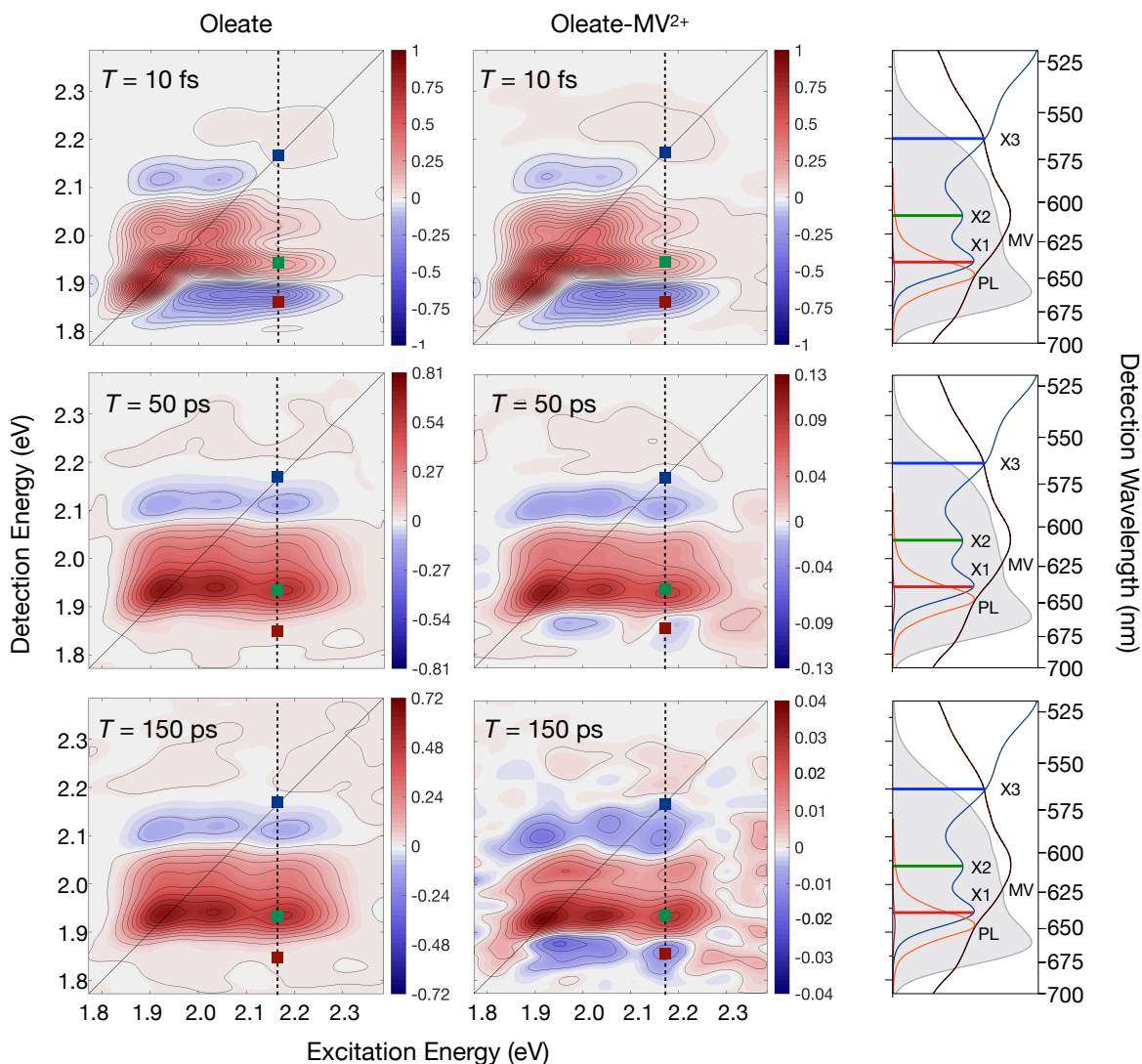


Figure 4.4. Time evolution of 2D spectra of oleate-capped QD and QD-MV²⁺ with respect to the population time, T . The 2D spectra on the left are those of the oleate-capped QDs used in the control experiment. The 2D spectra of the QD-MV²⁺ complex are shown on the right side. The intensities of the 2D spectra are auto scaled with respect to the maxima of the signal at a given time, T . The side panels plot the linear absorption oscillator strength (blue), photoinduced absorption spectrum of MV^{••} (brown), and photoluminescence (PL) spectra (orange). The amplitude transients sampled at the marked coordinates (excitation at X3 and detection at X3, X1, and PL) are shown in Figure 4.5.

There were no significant differences observed in the 2D spectra of the control oleate-capped QDs and the QD-MV²⁺ complex in the early times. The peak patterns are very similar to that described in Chapter 3. The emerging off-diagonal SE cross peaks during time evolution shows the relaxation of higher energy excitons to the lower energy states. Similar to the oleate, the 2D spectra exhibited an excited state absorption (ESA) at 1.88 eV arising from the formation of trap states or biexcitons. The intensity of the ESA is much higher than that of the larger QDs presented in the Chapter 3. This might indicate that the ligand coverage on the surface might be lower for this set of QDs giving rise to more trap states. However, in the later time, at $T = 50$ ps the GSB/SE signals corresponding to the formation of X2 and X1 decreases significantly. This indicates decay of population from these lower energy states due to the electron transfer from X2, X1 to the MV²⁺. At delay times, $T = 50$ ps and $T = 100$ ps, there appears an ESA signal detected at 1.85 eV throughout most of the excitation energies. This ESA corresponds to the photoinduced absorption of the MV^{+•} radical formed after the electron transfer from the core of the QDs.

4.3.3 Global Analysis and Coherence Analysis

To understand the kinetics of X3 relaxation and the electron transfer from QD to MV²⁺, the amplitude of the evolution of the nonoscillatory kinetic response excited at the energy level of X3 was subjected to global analysis (Figure 4.5). Global analysis models evolution of spectral response as a linear combination of evolution-associated difference spectra (EADS) from different spectrokinetic species.³⁰ Each of the EADS in the global model can be viewed as the average spectral signature of the different component of the model. For each excitation, the sequence of species in the kinetic model is the simplest one that fits the 2DES amplitude as a function of the delay T . To determine the simplest model to describe

the kinetics, the residual (the difference between data and the fitted values) across the spectrum is monitored to make sure that the intensity is around zero.

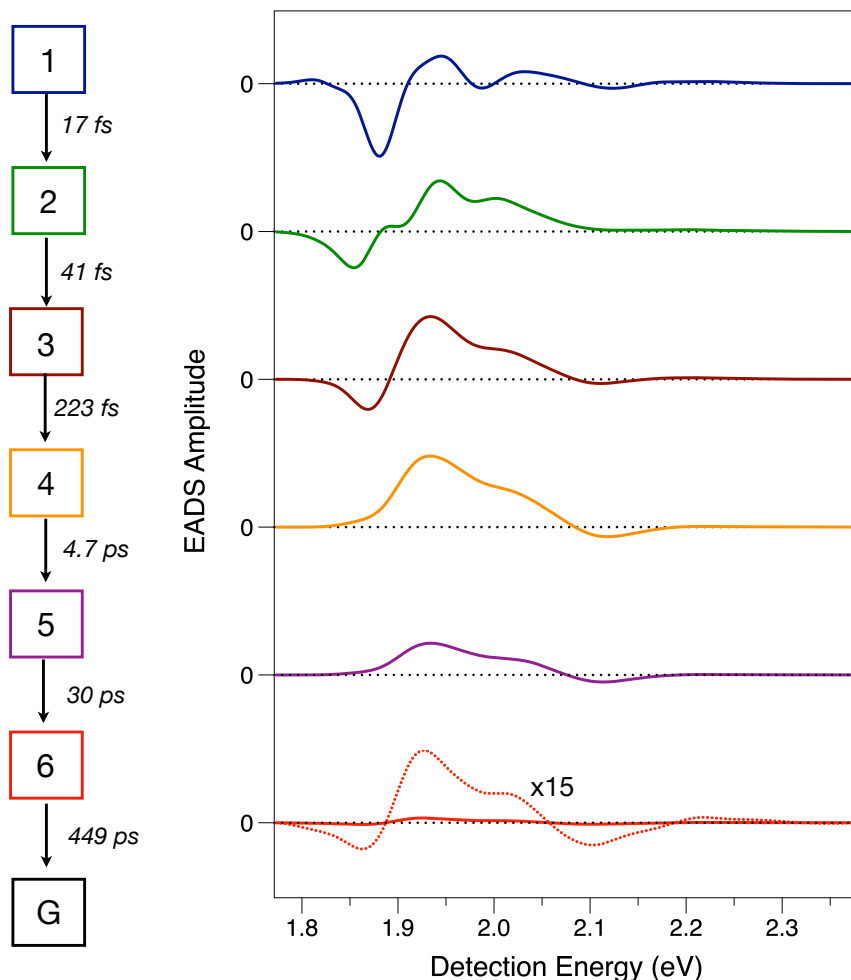


Figure 4.5. Global analysis of the population response of the X3 (2.102-2.214 eV) excitation region of 2DES spectrum of QD-MV²⁺ complex. On the left is the kinetic scheme for the global model with time constants for each relaxation pathway. Evolution associated difference spectra (EADS) for each compartment in the kinetic scheme are present on the right. The final component of the model is enhanced 15 times to project out the amplitudes.

To describe the kinetic response of X3, the global model required six different spectrokinetic species (see kinetic scheme in Figure 4.5). The character of these kinetic species is a combination of ground-state bleaching (GSB), stimulated emission (SE), and

negative-going excited-state absorption (ESA). The first component is the response from the X3 after excitation. The EADS of this component has a positive GSB and SE signals at the excitation energy corresponding to the X3 exciton on the detection-energy axis.

Additionally, there is a positive signal at the energies of X1 and X2, this can be attributed to the shared ground state nature of all the excitations. The first two compartments rapidly evolve with time constants of 17 fs and 41 fs indicative of a coherent relaxation dynamics. This coherent relaxation process also contributes to a small increase in the intensity of the GSB/SE amplitude at X1 and X2. Another notable event during this time frame is the shift and decrease in the ESA character at 1.88 eV. The ESA signal observed here is due to the formation of biexcitons of X3 with X1 (1.88 eV). The decrease in the ESA can be attributed to two processes: first the overlapping SE signal produced during the relaxation of X3 to X1 and X2 and second the decay of the ESA due to the decay of the biexciton state of X3 and X1. The third spectrokinetic component evolves with a time constant of 220 fs. A decrease in the positive EADS amplitude at X3 energy is observed and at the same time there is increase in the amplitude of at X1 and X2. The evolution of the third component to the fourth component is due to the hot electron cooling from the $1P_e$ electronic state to the $1S_e$ electronic state in an electron-hole picture of the QDs. It should be noted that excitons X1 and X2 have the same electronic energy level, that is, $1S_e$. Therefore, when the electron relaxes from $1P_e$ to $1S_e$, the SE amplitude increases simultaneously at detection energies of both X1 and X2. The kinetics of the evolution of first three spectrokinetic components of QD-MV²⁺ are very similar to that of the QDs. The evolution of fourth species to fifth species has a time constant of 4.7 ps. In terms of EADS evolution, there is a decrease in the SE at the energy levels of X2 and X1 owing to the electron transfer from these states. The evolution

of the fifth component to the sixth component is almost complete decay of the X1 and X2 SE signals with a time constant of 30 ps. This evolution indicates the electron transfer from these levels to the HOMO of MV²⁺. The sixth component has a very small signal intensity compared to all the other components. The significant part of the EADS is the ESA seen at 1.85 eV and 2.1 eV which is the photoinduced absorption signal from the methyl viologen radical cation. This signal is very weak compared with the signals from the QDs, and there is a large spectral overlap of the X2 and X1 excitons in this region which makes it even more difficult to detect the weak ESA from MV^{•+}. The weak response from the MV^{•+} can be understood in terms of the extinction coefficient $\epsilon = 13800 \text{ M}^{-1} \text{ cm}^{-1}$ at 2.03 eV²³ which is 100 times smaller than that of the CdSe QDs.³¹ The final component is the relaxation of the MV^{•+} to the ground state. This process is slow and takes several hundred picoseconds or even nanoseconds.¹⁵

The amplitude vs. population time delay at different coordinates in the 2D spectra were plotted to show the population dynamics (Figure 4.6b). The blue trace is extracted at (X3, X3) which shows the population relaxation after the optical preparation of the X3 state. The green transient (X3, X1) and the maroon (X3, PL) show the transients at coordinates excited at X3 and detected at lower energy levels, X1 and PL. The top panel of Figure 4.6b are the transients obtained from the control 2DES experiment on oleate-capped QDs whereas the bottom panel show the transients obtained from the 2DES experiments on the QD-MV²⁺ complex. Initially, the signal amplitude at the crosspeak coordinates rises as the population from X3 relaxes to these lower energy levels. In oleate-capped QDs, the signal amplitude at later times, that is, in picosecond time range, decays very slowly. In contrast to this, the signal intensity at the crosspeak of the QD-MV²⁺ complex increases in

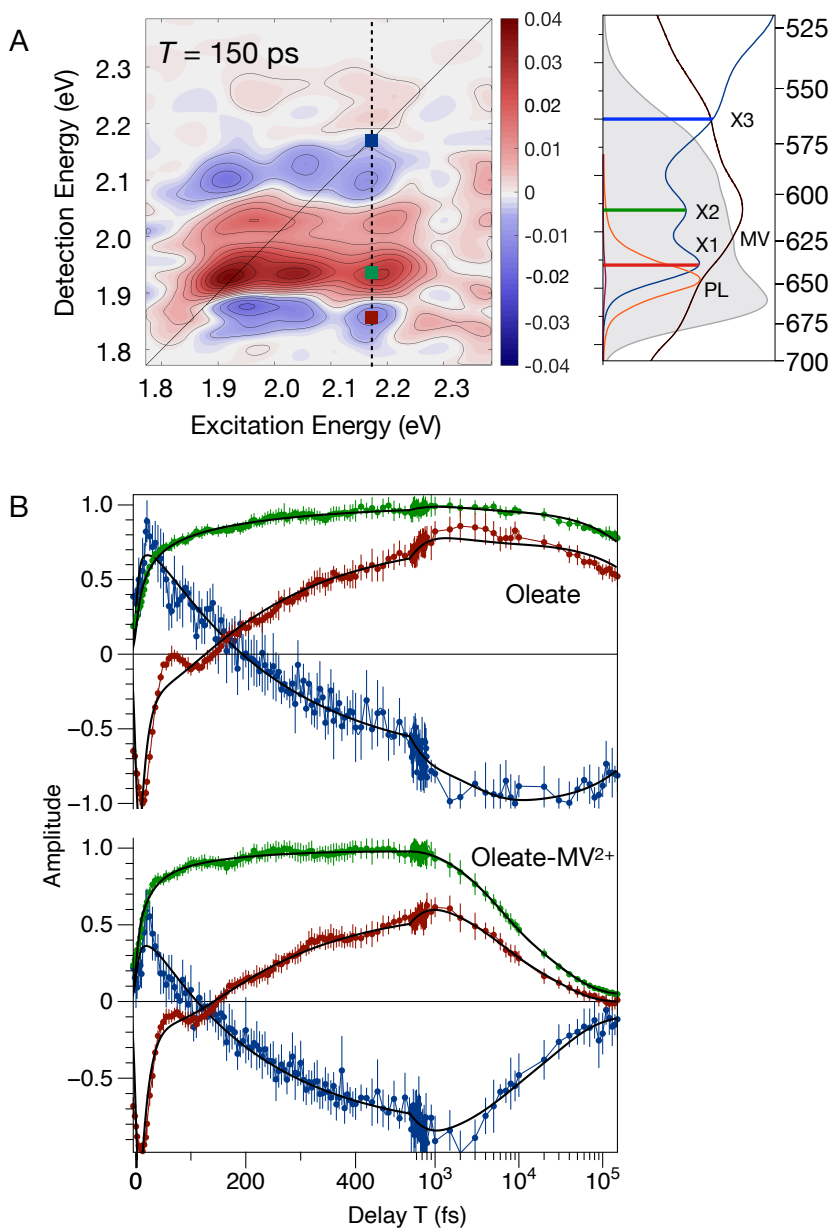


Figure 4.6. Amplitude transient comparison of QDs and QD-MV²⁺ at various coordinates. (a) 2D spectra of the QD-MV²⁺ complex with marked coordinates (X3, X3) (blue), (X3, X1) (green) and (X3, PL) (maroon). The side panels plot the linear absorption oscillator strength (blue), photoinduced absorption spectrum of MV^{••} (brown), and photoluminescence (PL) spectra (orange). (b) Amplitude transients at for the QDs (top panel) and QD-MV²⁺ (bottom panel) for the marked coordinates in the 2D spectra.

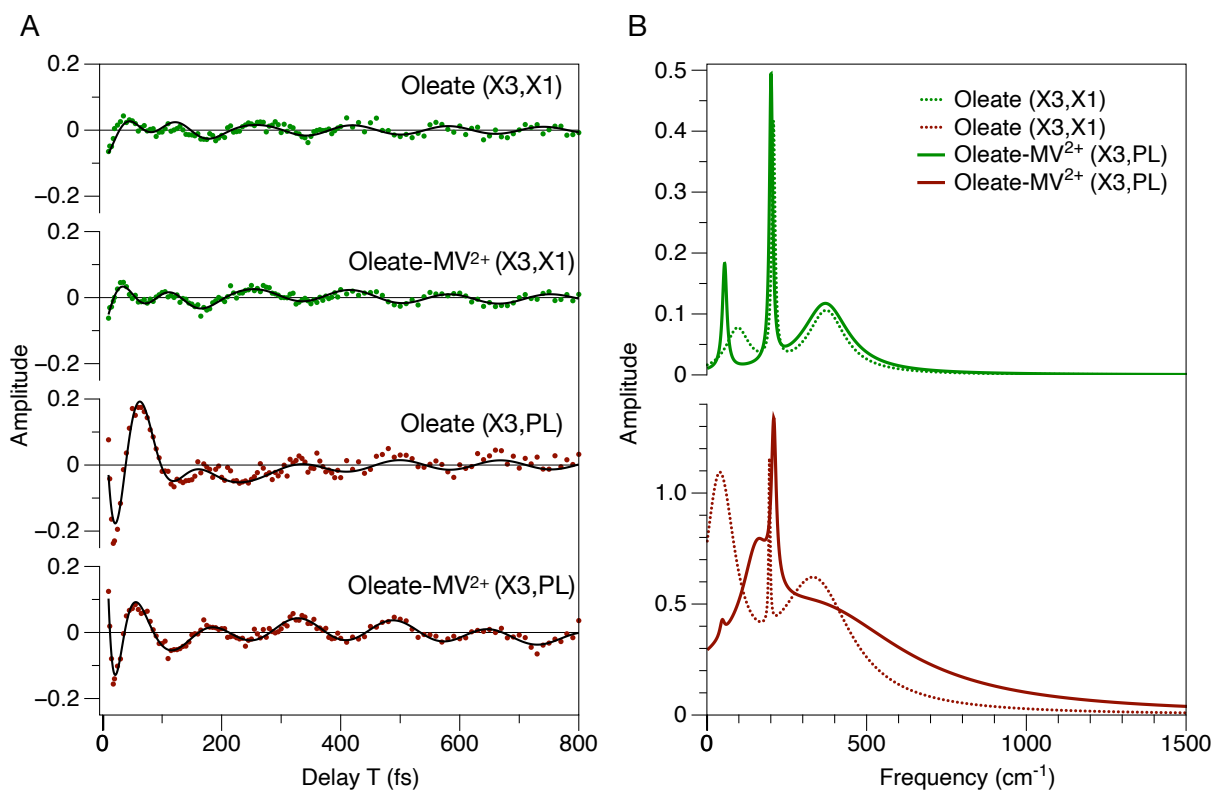


Figure 4.7. Frequency analysis of the residuals of the transients shown in Figure 4.6. (a) Residuals of the transients presented in the Figure 4.6. The green traces correspond to the coordinate (X3, X1) and the maroon trace correspond to the coordinate (X3, PL). The LPSVD fit function is plotted as the black trace overlapping on the residuals of the transients. (b) LPSVD models for the oscillations observed in the residuals. The dotted lines represent the amplitude spectra of the QDs, and the solid lines represent the amplitude spectra of the QD-MV²⁺ of the complex. The model parameters are provided in Tables 4.1 and 4.2.

the fs time range but decays in picosecond domain. The initial rise of the signal is due to the relaxation of X3 exciton to X2 and X1 whereas the decay in the ps domain is the signature of photoinduced charge transfer from X2 and X1 to the MV²⁺. Another notable difference in the transients are the modulation and their amplitudes. The transients of the QD-MV²⁺ show enhanced amplitudes of modulations at the crosspeak coordinates compared to the oleate-capped QDs.

Table 4.1. Parameters (frequency, amplitude, phase, and damping time) for LPSVD analysis of X3 excitation for QDs at the indicated coordinates in 2D spectra.

Coordinate	Frequency	Amplitude	Phase (radians)	Damping time
(X3, X1)	96 cm ⁻¹	0.015	0.44	120 fs
	208 cm ⁻¹	0.012	2.30	874 fs
	374 cm ⁻¹	0.037	3.12	74 fs
(X3, PL)	40 cm ⁻¹	0.296	0.79	88 fs
	196 cm ⁻¹	0.009	0.44	2.02 ps
	336 cm ⁻¹	0.405	1.60	38 fs

Table 4.2. Parameters (frequency, amplitude, phase, and damping time) for LPSVD analysis of X3 excitation for QD-MV²⁺ at the indicated coordinates in 2D spectra.

Coordinate	Frequency	Amplitude	Phase (radians)	Damping time
(X3, X1)	56 cm ⁻¹	0.007	2.69	636 fs
	201 cm ⁻¹	0.014	3.28	872 fs
	371 cm ⁻¹	0.051	2.40	60 fs
(X3, PL)	48 cm ⁻¹	0.003	2.83	630 fs
	157 cm ⁻¹	0.100	1.62	101 fs
	209 cm ⁻¹	0.032	0.56	592 fs
	331 cm ⁻¹	0.83	0.94	15 fs

The population relaxation in the signal response is accompanied by rapidly and slowly damped modulations. The rapidly damped modulations have damping times of ~50 fs

whereas the slowly damped modulations have damping times of several hundreds of femtoseconds. The rapid damping of the coherences is consistent with their assignment to excited-state coherent wavepacket motions following hot-carrier cooling. The slowly damped ones are mostly stimulated Raman coherences in the ground state. The residuals of the crosspeaks are extracted and subjected to LPSVD analysis. The LPSVD is carried out in the time range of 10-800 fs to resolve both rapidly damped and slowly damped modulations simultaneously.

For the coordinate (X3, X1), there are three major frequencies at 96 cm^{-1} , 208 cm^{-1} and 374 cm^{-1} in the LPSVD spectrum (Table 1). The nature of the LPSVD spectrum remains very similar in case of the QDs and the QD-MV²⁺ complex. The low-frequency peaks are relatively slowly damped. The 208 cm^{-1} peak is the stimulated Raman signal due to the lattice vibration, longitudinal optical (LO) phonon mode in a typical CdSe QD. Stimulated Raman coherence wavepackets dampen out in the vibrational dephasing times, which are in the picosecond time domain. The 374 cm^{-1} mode that is very similar in the QD and QD-MV²⁺ complex is likely an oleate mode, symmetric in-plane scissor of the carboxylate mixed with C-H/C-C stretching along the long alkyl chain. The most interesting part is the (X3, PL) coordinate where the vibrational mode patterns are quite different between the two samples. In the QD-MV²⁺ complex, there appears a rapidly damped low frequency mode at 157 cm^{-1} which is not present in the QD oleate. The frequency is lower than the lattice mode owing to the mixing of these modes. Another interesting mode is the 330 cm^{-1} mode which is very rapidly damped. The 336 cm^{-1} mode in the oleate is replaced by this rapidly damped mode. Since the damping time of this mode is short, there could be some uncertainty regarding the peak position. To understand the origin of this mode, a

Gaussian³² electronic structure calculation and vibrational analysis is carried out on the MV²⁺ molecule. The normal mode analysis was carried out using the B3LYP functional 6-311g(d,p) level of theory. The detailed mode assignments are described in the discussion section.

To compare these rapidly damped modulations across the excitation energy, an excitation-specific coherence map (Figure 4.8) was generated by performing the FFT of residuals in the time range (10-200 fs) at X3 excitation. In the excitation-specific coherence map, the amplitude of the FFT at each coordinate is plotted with frequency on the x-axis and detection energy on the y-axis. These maps encompass all the frequency information of

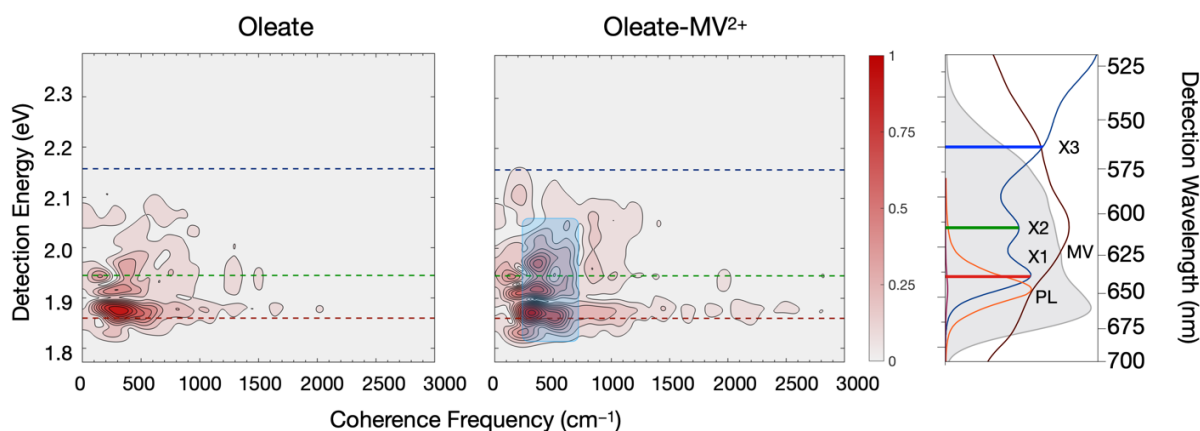


Figure 4.8. Comparison of excitation-specific coherence map at X3 excitation (from 10-200 fs) for QD and QD-MV²⁺ complex. The side panels plot the linear absorption oscillator strength (blue), photoinduced absorption spectrum of MV^{+•} (brown), and PL spectra (orange). The blue box illustrates the portion of the excitation-specific coherence map where significant amplitude differences between QD and QD-MV²⁺ are evident.

the coherent dynamics at a given excitation energy. In the case of oleate-capped CdSe QDs, the coherence map reveals prominent modulations occurring across several lower energy levels, with the most significant intensities observed at the X1 and PL energy levels. The major peak observed are $\sim 200 \text{ cm}^{-1}$ corresponding to the LO phonon mode. At the same

time, there is an overall enhancement of vibrational amplitudes in the excitation specific coherence map of QD-MV²⁺ complex.

4.4 Discussion

The results in this chapter indicate that the photoinduced charge transfer from CdSe QDs to the MV²⁺ ligand molecule involves a coherent vibronic intermediate (Figure 4.10). The kinetic analysis and global modelling indicate that the X3 exciton relaxes to the lower energy states, X2 and X1 similar to the relaxation kinetics observed in oleate-capped QDs in Chapter 3. The X2 and X1 state, owing to their shared electronic state, 1S_e donate the electron to the LUMO of the MV²⁺. The charge transfer process has a time constant of 30 ps in this case. The charge transfer rate in this study is slower compared to the charge transfer rates observed in the CdS quantum dots because of the low driving force or smaller energy gap between the donor and the acceptor states.^{14,15}

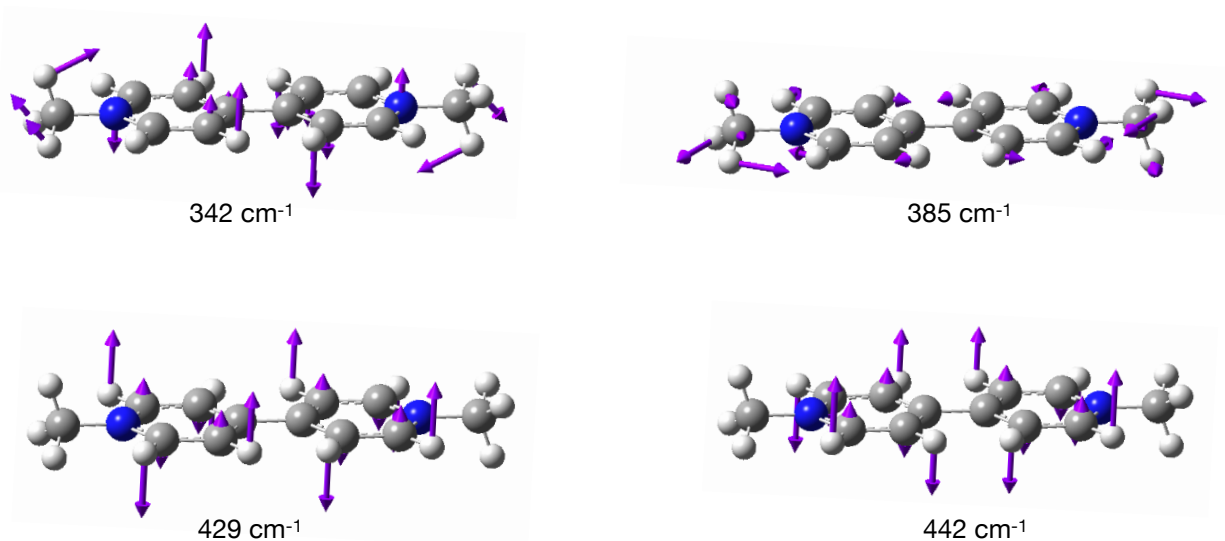


Figure 4.9. Vector representation of the vibrational modes obtained from the Raman spectra calculation of MV²⁺ for 340-450 cm⁻¹ region. Purple arrows indicate the direction of displacement of each atom from its equilibrium position during the vibrations.

The comparison of short-time excitation-specific coherence map of QD and QD-MV²⁺ complex reveals the enhancement in amplitudes is particularly seen in the mid frequency regions. Higher vibrational activity seen in the lowest energy region at ~1.88 eV region where the ESA of the MV²⁺ is being observed in the 2D spectra. The analysis of the mode-specific character of the coherences reveals the structural origin of the electronic-ligand vibrational coupling present in the intermediate (Figure 4.9). The main modes found in this intermediate is the ~160 cm⁻¹ which corresponds to a mixed mode with the lattice vibration (LO phonon) and ligand vibrations. This mode is a resultant of the quantum coherent mixing of the core electronic states with the vibrational states of the ligand. Apart from the low frequency modes, higher amplitudes are also observed in mid frequency regions at ~330 cm⁻¹. There are four modes that were isolated from the MV²⁺ normal mode analysis in the 340-450 cm⁻¹ region. A 342 cm⁻¹ involves the out-of-plane bending modes of the pyridyl rings and adjacent hydrogens on the methyl group. The 385 cm⁻¹ corresponds to the in-plane twisting of the MV²⁺ molecule. The 430 cm⁻¹ and 440 cm⁻¹ modes are very similar in nature and exclusively involves out-of-plane motions of the C atoms in the bipyridyl rings. The 330 cm⁻¹ mode detected in the LPSVD model could be either one of these modes or a mix of some of these modes and the core-QD lattice modes. Therefore, the mode observed ~330 cm⁻¹ is assigned to the in-plane and out-of-plane bending and deformation of the bipyridyl rings.^{33,34} An enhancement of the vibrational amplitudes along with detection of MV-specific vibrational motions, can be rationalized in terms of presence of mixed QD/MV²⁺ surface. It is highly unlikely to observe MV²⁺ vibrations in these energy regions without mixing of QD core with MV²⁺, owing to the absence of direct excitation and very small extinction coefficient of MV²⁺ compared to QDs. These

observations are consistent with the presence of an intermediate charge transfer state formed via coherent wavepacket motions. In summary, the exciton relaxation and photoinduced charge transfer can be understood in terms of a molecular exciton picture.

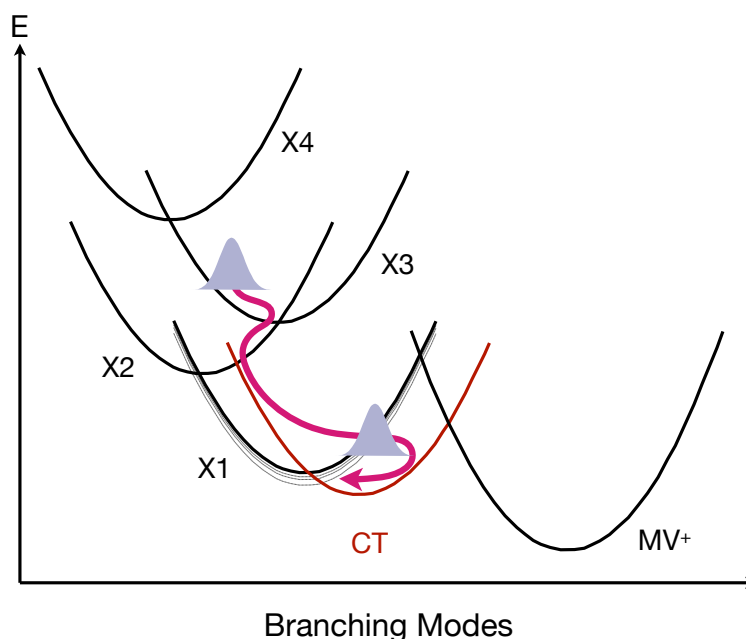


Figure 4.10. Schematic representation of the potential energy surface representing the relaxation of X3 optical excitation via a cascade of conical intersections via coherent wavepacket motions. The red potential energy curve depicts the bridging coherent charge transfer intermediate in the QD-MV²⁺ complex.

This picture involves a cascade of potential energy surfaces corresponding to different excitons. Upon photoexcitation, a coherent wavepacket is prepared at the X3 exciton. This wavepacket slides via multiple potential energy surfaces and cross conical intersections (CIs) during exciton relaxation.^{35,36} Upon passage of the wavepacket via CIs, electronic energy is converted into vibrational motions along certain coordinates. The coherent wavepacket motions gives rise to rapidly damped modulations with frequencies of surface-ligand vibrational motions along the pathway of relaxation of the excitons. Surface ligand

vibrations serve as branching modes and lifts the degeneracy of the potential energy surface crossings or conical intersections.³⁷

In other words, these vibrational modes are the ones that experience displacement during the nonadiabatic relaxation of the exciton. In the study presented here, the X3 exciton relaxation mechanism and coherences are quite similar in the initial stages for the case of QDs and the QD-MV²⁺ complex. However, the presence of different vibronic coherence and associated peak patterns in the lower energy region corresponding to energy levels of MV^{••} indicate that there is a charge transfer intermediate formed via coherent wavepacket motions. This intermediate involves coherent wavepacket motions that are resultant of mixed vibrations of the core and the surface electron acceptor molecule specifically out-of-plane motions of pyridyl rings. This coherent CT intermediate initiates the photoinduced CT from the core of the QDs to the LUMO of the surface electron acceptor, MV²⁺. The results presented in this chapter are consistent with the proposed hypothesis suggesting a presence of CT intermediate formed via vibronic coherence that initiates the photoinduced CT from QD-MV²⁺. These findings represent promising advances in understanding how to engineer quantum coherences associated with organic ligands and adsorbed electron- and excitation-energy acceptors on quantum dots' surfaces to optimize and enhance the efficiency of quantum dots in photocatalysis.

REFERENCES

- (1) Gray, H. B. Powering the Planet with Solar Fuel. *Nat. Chem.* **2009**, *1* (1), 7.
- (2) Grätzel, M. Photoelectrochemical Cells. *Nature* **2001**, *414* (6861), 338–344.
- (3) Chen, X.; Li, C.; Grätzel, M.; Kostecki, R.; Mao, S. S. Nanomaterials for Renewable Energy Production and Storage. *Chem. Soc. Rev.* **2012**, *41* (23), 7909–7937.
- (4) Chuang, C.-H. M.; Brown, P. R.; Bulović, V.; Bawendi, M. G. Improved Performance and Stability in Quantum Dot Solar Cells through Band Alignment Engineering. *Nat. Mater.* **2014**, *13* (8), 796–801.
- (5) Li, L.; Pandey, A.; Werder, D. J.; Khanal, B. P.; Pietryga, J. M.; Klimov, V. I. Efficient Synthesis of Highly Luminescent Copper Indium Sulfide-Based Core/Shell Nanocrystals with Surprisingly Long-Lived Emission. *J. Am. Chem. Soc.* **2011**, *133* (5), 1176–1179.
- (6) Steckel, J. S.; Coe-Sullivan, S.; Bulović, V.; Bawendi, M. G. 1.3 μm to 1.55 μm Tunable Electroluminescence from PbSe Quantum Dots Embedded within an Organic Device. *Adv. Mater.* **2003**, *15* (21), 1862–1866.
- (7) Konstantatos, G.; Howard, I.; Fischer, A.; Hoogland, S.; Clifford, J.; Klem, E.; Levina, L.; Sargent, E. H. Ultrasensitive Solution-Cast Quantum Dot Photodetectors. *Nature* **2006**, *442* (7099), 180–183.
- (8) Zhao, L.-M.; Meng, Q.-Y.; Fan, X.-B.; Ye, C.; Li, X.-B.; Chen, B.; Ramamurthy, V.; Tung, C.-H.; Wu, L.-Z. Photocatalysis with Quantum Dots and Visible Light: Selective and Efficient Oxidation of Alcohols to Carbonyl Compounds through a Radical Relay Process in Water. *Angew. Chem. Int. Ed Engl.* **2017**, *56* (11), 3020–3024.
- (9) Sun, P.; Xing, Z.; Li, Z.; Zhou, W. Recent Advances in Quantum Dots Photocatalysts. *Chem. Eng. J.* **2023**, *458*, 141399.
- (10) Lian, S.; Christensen, J. A.; Kodaimati, M. S.; Rogers, C. R.; Wasielewski, M. R.; Weiss, E. A. Oxidation of a Molecule by the Biexcitonic State of a CdS Quantum Dot. *J. Phys. Chem. C* **2019**, *123* (10), 5923–5930.
- (11) Huang, J.; Huang, Z.; Yang, Y.; Zhu, H.; Lian, T. Multiple Exciton Dissociation in CdSe Quantum Dots by Ultrafast Electron Transfer to Adsorbed Methylene Blue. *J. Am. Chem. Soc.* **2010**, *132* (13), 4858–4864.
- (12) Huang, J.; Stockwell, D.; Huang, Z.; Mohler, D. L.; Lian, T. Photoinduced Ultrafast Electron Transfer from CdSe Quantum Dots to Re-Bipyridyl Complexes. *J. Am. Chem. Soc.* **2008**, *130* (17), 5632–5633.

- (13) Okuhata, T.; Tamai, N. Face-Dependent Electron Transfer in CdSe Nanoplatelet–Methyl Viologen Complexes. *J. Phys. Chem. C* **2016**, *120* (30), 17052–17059.
- (14) Zhu, H.; Song, N.; Lv, H.; Hill, C. L.; Lian, T. Near Unity Quantum Yield of Light-Driven Redox Mediator Reduction and Efficient H₂ Generation Using Colloidal Nanorod Heterostructures. *J. Am. Chem. Soc.* **2012**, *134* (28), 11701–11708.
- (15) Morris-Cohen, A. J.; Frederick, M. T.; Cass, L. C.; Weiss, E. A. Simultaneous Determination of the Adsorption Constant and the Photoinduced Electron Transfer Rate for a CdS Quantum Dot-Viologen Complex. *J. Am. Chem. Soc.* **2011**, *133* (26), 10146–10154.
- (16) Tagliazucchi, M.; Tice, D. B.; Sweeney, C. M.; Morris-Cohen, A. J.; Weiss, E. A. Ligand-Controlled Rates of Photoinduced Electron Transfer in Hybrid CdSe Nanocrystal/Poly(Viologen) Films. *ACS Nano* **2011**, *5* (12), 9907–9917.
- (17) Peterson, M. D.; Jensen, S. C.; Weinberg, D. J.; Weiss, E. A. Mechanisms for Adsorption of Methyl Viologen on CdS Quantum Dots. *ACS Nano* **2014**, *8* (3), 2826–2837.
- (18) Morris-Cohen, A. J.; Vasilenko, V.; Amin, V. A.; Reuter, M. G.; Weiss, E. A. Model for Adsorption of Ligands to Colloidal Quantum Dots with Concentration-Dependent Surface Structure. *ACS Nano* **2012**, *6* (1), 557–565.
- (19) Zhao, F.; Li, Q.; Han, K.; Lian, T. Mechanism of Efficient Viologen Radical Generation by Ultrafast Electron Transfer from CdS Quantum Dots. *J. Phys. Chem. C* **2018**, *122* (30), 17136–17142.
- (20) Zeng, P.; Kirkwood, N.; Mulvaney, P.; Boldt, K.; Smith, T. A. Shell Effects on Hole-Coupled Electron Transfer Dynamics from CdSe/CdS Quantum Dots to Methyl Viologen. *Nanoscale* **2016**, *8* (19), 10380–10387.
- (21) Tisdale, W. A.; Williams, K. J.; Timp, B. A.; Norris, D. J.; Aydil, E. S.; Zhu, X.-Y. Hot-Electron Transfer from Semiconductor Nanocrystals. *Science* **2010**, *328* (5985), 1543–1547.
- (22) Song, Y.; Clifton, S. N.; Pensack, R. D.; Kee, T. W.; Scholes, G. D. Vibrational Coherence Probes the Mechanism of Ultrafast Electron Transfer in Polymer-Fullerene Blends. *Nat. Commun.* **2014**, *5*, 4933.
- (23) Watanabe, T.; Honda, K. Measurement of the Extinction Coefficient of the Methyl Viologen Cation Radical and the Efficiency of Its Formation by Semiconductor Photocatalysis. *J. Phys. Chem.* **1982**, *86* (14), 2617–2619.
- (24) Jasieniak, J.; Bullen, C.; van Embden, J.; Mulvaney, P. Phosphine-Free Synthesis of CdSe Nanocrystals. *J. Phys. Chem. B* **2005**, *109* (44), 20665–20668.

- (25) Frazier, J.; Cavey, K.; Coil, S.; Hamo, H.; Zhang, M.; Van Patten, P. G. Rapid and Sensitive Identification and Discrimination of Bound/Unbound Ligands on Colloidal Nanocrystals via Direct Analysis in Real-Time Mass Spectrometry. *Langmuir* **2021**, *37* (50), 14703–14712.
- (26) Shim, S.-H.; Zanni, M. T. How to Turn Your Pump-Probe Instrument into a Multidimensional Spectrometer: 2D IR and Vis Spectroscopies via Pulse Shaping. *Phys. Chem. Chem. Phys.* **2009**, *11* (5), 748–761.
- (27) Lozovoy, V. V.; Pastirk, I.; Dantus, M. Multiphoton Intrapulse Interference. IV. Ultrashort Laser Pulse Spectral Phase Characterization and Compensation. *Opt. Lett.* **2004**, *29* (7), 775–777.
- (28) DeLong, K. W.; Trebino, R.; Hunter, J.; White, W. E. Frequency-Resolved Optical Gating with the Use of Second-Harmonic Generation. *J. Opt. Soc. Am. B, JOSAB*. <https://doi.org/10.1364/JOSAB.11.002206>.
- (29) Augulis, R.; Zigmantas, D. Two-Dimensional Electronic Spectroscopy with Double Modulation Lock-in Detection: Enhancement of Sensitivity and Noise Resistance. *Opt. Express* **2011**, *19* (14), 13126–13133.
- (30) van Stokkum, I. H. M.; Larsen, D. S.; van Grondelle, R. Global and Target Analysis of Time-Resolved Spectra. *Biochim. Biophys. Acta* **2004**, *1657* (2–3), 82–104.
- (31) Yu, W. W.; Qu, L.; Guo, W.; Peng, X. Experimental Determination of the Extinction Coefficient of CdTe, CdSe, and CdS Nanocrystals. *Chem. Mater.* **2003**, *15* (14), 2854–2860.
- (32) Frisch, M. J.; Trucks, G. W.; Schlegel, H. B.; Scuseria, G. E.; Robb, M. A.; Cheeseman, J. R.; Scalmani, G.; Barone, V.; Petersson, G. A.; Nakatsuji, H.; Li, X.; Caricato, M.; Marenich, A. V.; Bloino, J.; Janesko, B. G.; Gomperts, R.; Mennucci, B.; Hratchian, H. P.; Ortiz, J. V.; Izmaylov, A. F.; Sonnenberg, J. L.; Williams; Ding, F.; Lipparini, F.; Egidi, F.; Goings, J.; Peng, B.; Petrone, A.; Henderson, T.; Ranasinghe, D.; Zakrzewski, V. G.; Gao, J.; Rega, N.; Zheng, G.; Liang, W.; Hada, M.; Ehara, M.; Toyota, K.; Fukuda, R.; Hasegawa, J.; Ishida, M.; Nakajima, T.; Honda, Y.; Kitao, O.; Nakai, H.; Vreven, T.; Throssell, K.; Montgomery, J. A., Jr.; Peralta, J. E.; Ogliaro, F.; Bearpark, M. J.; Heyd, J. J.; Brothers, E. N.; Kudin, K. N.; Staroverov, V. N.; Keith, T. A.; Kobayashi, R.; Normand, J.; Raghavachari, K.; Rendell, A. P.; Burant, J. C.; Iyengar, S. S.; Tomasi, J.; Cossi, M.; Millam, J. M.; Klene, M.; Adamo, C.; Cammi, R.; Ochterski, J. W.; Martin, R. L.; Morokuma, K.; Farkas, O.; Foresman, J. B.; Fox, D. J. *Gaussian 16 Rev. C.01*; Wallingford, CT, 2016.
- (33) Forster, M.; Girling, R. B.; Hester, R. E. Infrared, Raman and Resonance Raman Investigations of Methylviologen and Its Radical Cation. *J. Raman Spectrosc.* **1982**, *12* (1), 36–48.

- (34) Poizat, O.; Sourisseau, C.; Mathey, Y. Vibrational Study of the Methyl Viologen Dication MV²⁺ and Radical Cation MV^{•+} in Several Salts and as an Intercalate in Some Layered MPS3 Compounds. *J. Chem. Soc. Lond. Faraday Trans. 1* **1984**, *80* (12), 3257–3274.
- (35) Levine, B. G.; Martínez, T. J. Isomerization through Conical Intersections. *Annu. Rev. Phys. Chem.* **2007**, *58*, 613–634.
- (36) Domcke, W.; Yarkony, D. R.; Köppel, H. *Conical Intersections*. <https://www.worldscientific.com/worldscibooks/10.1142/7803> (accessed 2023-10-15).
- (37) Tilluck, R. W.; Mohan T M, N.; Hetherington, C. V.; Leslie, C. H.; Sil, S.; Frazier, J.; Zhang, M.; Levine, B. G.; Van Patten, P. G.; Beck, W. F. Vibronic Excitons and Conical Intersections in Semiconductor Quantum Dots. *J. Phys. Chem. Lett.* **2021**, *12* (39), 9677–9683.

APPENDIX

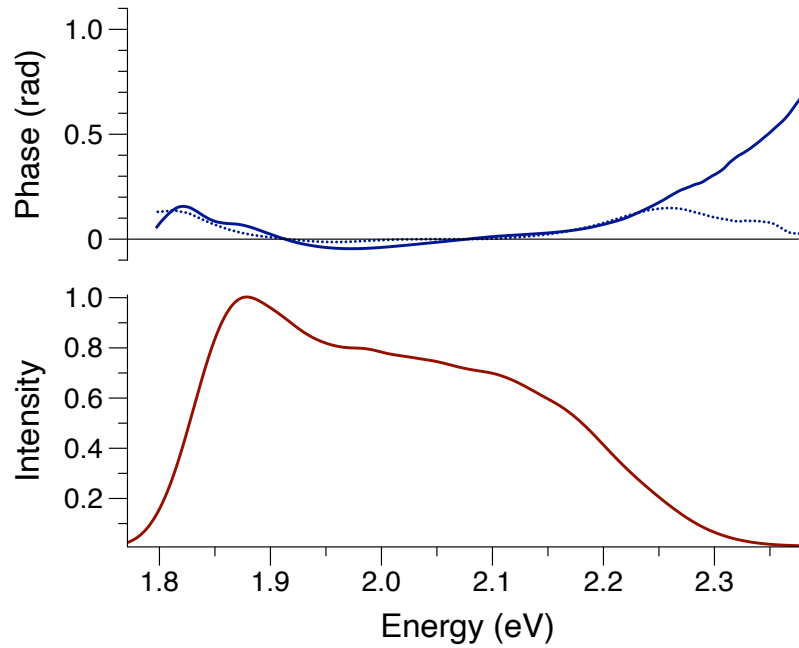


Figure A4.1. Residual phase and intensity spectra of the femtosecond laser pulses used in the broadband multidimensional electronic spectroscopy experiments. Top panel shows residual phase spectra after compression of the laser pulses used in the 2DES experiment for the pump beam (solid), and for the probe beam (dashed), as determined by MIIPS scans.²⁷ Bottom panel is the intensity spectrum of the laser pulses.

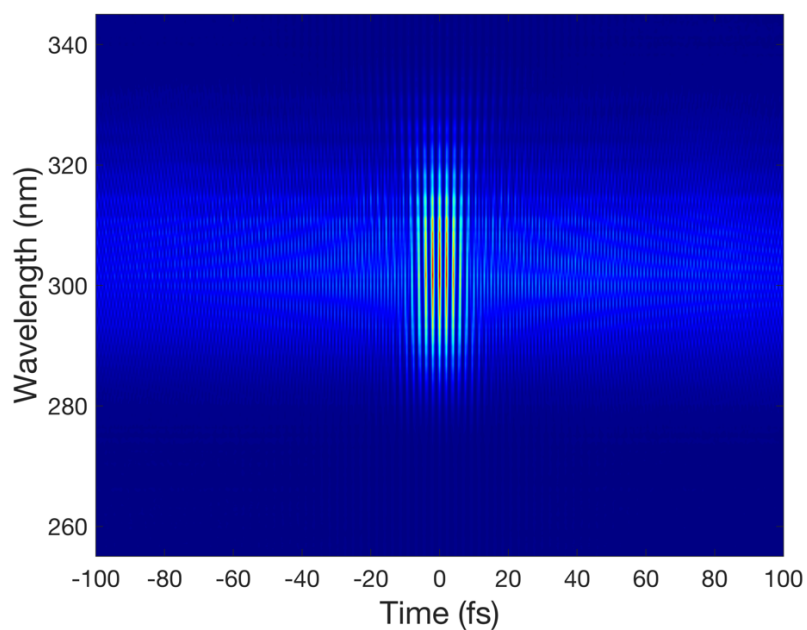


Figure A4.2. SHG-FROG²⁸ spectrogram for the pump pulses, as measured with scanned pulse pairs prepared by the pump beam's pulse shaper in the 2DES spectrometer.

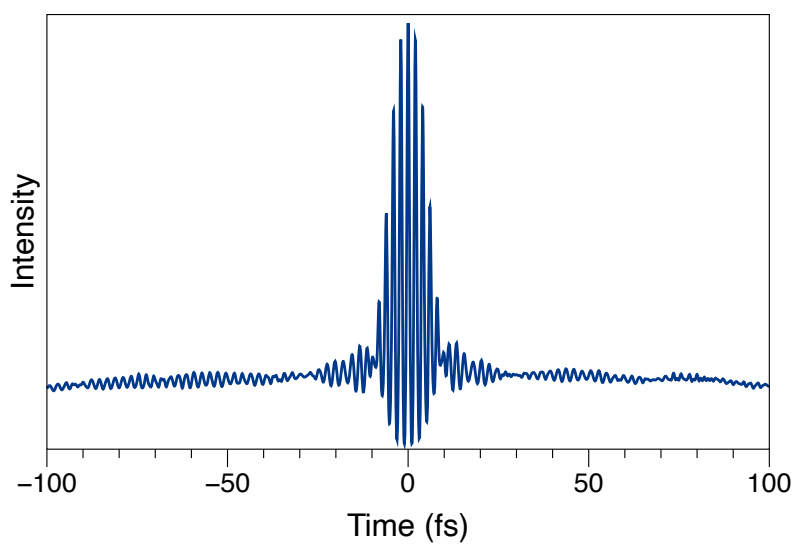


Figure A4.3. Interferometric autocorrelation of the pump pulses, determined as the integral of the SHG-FROG spectrogram (Figure A4.2).